

UC Berkeley

UC Berkeley Electronic Theses and Dissertations

Title

Evaporation-Driven Fast Crystallization of 3D Micro- and Nano-particle Assemblies via Micro Mechanical Systems

Permalink

<https://escholarship.org/uc/item/2f267691>

Author

Choi, Sun

Publication Date

2012

Peer reviewed|Thesis/dissertation

**Evaporation-Driven Fast Crystallization of 3D Micro- and Nano-particle
Assemblies via Micro Mechanical Systems**

by

Sun Choi

A dissertation submitted in partial satisfaction of the

requirements for the degree of

Doctor of Philosophy

in

Engineering-Mechanical Engineering

in the

Graduate Division

of the

University of California, Berkeley

Committee in charge:

Professor Albert P. Pisano, Co-Chair

Professor Tarek I. Zohdi, Co-Chair

Professor Liwei Lin

Professor Ming C. Wu

Spring 2012

Evaporation-Driven Fast Crystallization of 3D Micro- and Nano-particle
Assemblies via Micro Mechanical Systems

Copyright © 2012

by

Sun Choi

Abstract

Evaporation-Driven Fast Crystallization of 3D Micro- and Nano-particle
Assemblies via Micro Mechanical Systems

by

Sun Choi

Doctor of Philosophy in Engineering-Mechanical Engineering

University of California, Berkeley

Professor Albert P. Pisano, Co-Chair

Professor Tarek I. Zohdi, Co-Chair

Fast crystallization of solid-phase materials in liquid medium is a crucial prerequisite to achieve the aims of a number of applications for micro-and nano-manufacturing, bio-chemical sensing technology and fundamental colloidal science. Corresponding mechanical systems for those applications are required to accommodate and take advantage of the virtue of multi-phase (liquid, gas, and solid phases) flow phenomenon to accomplish “crystallization” part for complete functioning. In this dissertation, evaporation-driven fast crystallization of micro-and nano-particles is demonstrated via micro mechanical systems in order to inspire potential implementation of those systems to existing mechanical systems. Various fast crystallizing behaviors of micro, nanoparticles are demonstrated by multi-phase flow in the micro-mechanical systems. Evaporative flows such as open-channel flow, thin liquid-film flow, and fast, micro-scale evaporative liquid flow on hydrophobic surface are driving fast crystallization of the particles in micro-mechanical systems with sub-5 minute scale. Critical parameters for the analysis of colloidal motions in evaporative flows are identified by conventional thermo-coupled fluid mechanics and numerical values of those parameters were accurately calculated by particle-dynamic incorporated-computations to provide accounts for particle effects in evaporative self-assembly. Finally, electrical and

optical characterizations of crystallized 3D lattices are performed to demonstrate the feasibility of the developed systems for rapid, direct characterization of various target species. Experimental, analytical and computational parts of the dissertation complement each other with active cross-talks and reinforce the thesis argument that evaporation-driven multi-phase flow can be applied for the improvement of micro-and nano-manufacturing technologies, bio-chemical assay technologies and the development of platforms for fundamental colloidal sciences.

Now faith is being sure of what we hope for and certain of what we do not see. This is what ancients were commended for. By faith, we understand that the universe was formed at God's command, so that what is seen was not made out of what was visible.

Hebrews 11:1-3

To my Lord.

Table of Contents

Contents.....	ii
List of Figures.....	v
List of Tables.....	vii
Chapter 1 Introduction.....	1
1.1. Motivation for Fast Crystallization of Solid-Phase Species in Liquid.....	1
1.2. Reviews on Current Phase-Separation Systems.....	2
1.3. Introduction of Evaporative Self-Assembly of Micro-and Nano-Particles.....	6
Chapter 2 Constrained Microparticle Assembly by Open-Channel Flow.....	7
2.1. Introduction.....	7
2.2. Experimental Methods.....	7
2.2.1. Materials.....	7
2.2.2. Design and Fabrication of Open Microchannel.....	8
2.2.3. Patterning of Microparticles.....	8
2.2.4. Imaging.....	9
2.3. Principles of Self-Assembly of Microparticles.....	9
2.4. Theoretical calculation of Assembly Speed.....	11
2.5. Analysis on Experimental Results.....	13
2.5.1. Commensurable Effect.....	13
2.5.2. Theoretical Analysis.....	16
2.5.3. Release of Particle Assembly.....	21
Chapter 3 Templated Micro, Nanoparticle Assembly by Thin-Liquid Film Flow.....	24
3.1. Introduction.....	24
3.2. Experimental Methods.....	25
3.3. Principles of Confinement of 3D Micro, Nanoparticle Assemblies in Micro-Scale Templates.....	27
3.3.1. Preparation of Photopatterned Substrate.....	28
3.3.2. Description of Sequential Processes of Self-Assembly of Particles.....	28
3.4. Release of Particle Assemblies from Templates.....	32
3.5. Theoretical Analysis of Patterning Results.....	36

3.5.1. Scaling Analysis of Main Parameters in Hydrodynamics of Process	37
3.5.2. Studies of Scaling Effect, Effect of Volume and Concentration of Suspension on Patterning	40
3.5.3. Studies of Surface Charge Condition of Templates on Patterning	42
Chapter 4 Printed Micro, Nanoparticle Assembly by Micro Scale Evaporative Flow	45
4.1. Introduction.....	45
4.2. Experimental Methods	46
4.2.1. Materials.....	46
4.2.2. Fabrication of Printing Heads	47
4.2.3. Fabrication of Handling Wafer	48
4.2.4. Fabrication of Printing Head- Handling Wafer Complex	48
4.2.5. Micro-and Nano-particle Printing.....	49
4.3. Generation of Picoliter-scale Droplets of Particle Suspension	50
4.4. Rapid Evaporative Self-Assembly of Micro, nanoparticles on a Hydrophobic Surface .	53
4.5. Multiplexed Printing of Micro, Nanoparticle Clusters	60
Chapter 5 Studies on Particle Effects in Evaporative Self-Assembly by Numerical Simulation.	63
5.1. Introduction.....	63
5.2. Experimental Observation of Evaporative Self-Assembly of Particles	64
5.3. Particle-based Computational Modeling.....	65
5.4. Analysis on Particle Assemblies	70
Chapter 6 Electrical, Optical Characterization of Micro, Nanoparticle Assemblies	79
6.1. Introduction.....	79
6.2. Creation of 3D ZnO Nanoparticle Assemblies on Gold Electrodes	79
6.3. Electrical, Optical Characterization of ZnO Nanoparticle Assemblies	84
6.4. Study on Size-tunability of Particle Cluster Arrays by Fluorescence Microscopy.....	90
6.5. Study on Size-uniformity of Particle Cluster Arrays by SERS Measurement.....	92
Chapter 7 Conclusion and Future Work	95
7.1. Conclusion	95
7.2. Future Work.....	97
7.2.1. Micro-and Nano-manufacturing	97
7.2.2. Bio-chemical assays.....	97
7.2.3. Fundamental Colloidal Science	98
Bibliography	99
A.1. Relationship between Volume of Suspension and Nature of Particle Deposition.....	119

A.2. Images of 3 μm Silica Microspheres-based Structures after Lift-off	120
A.3. Calculation of Scaling Analysis	120
A.4. Calculations of Packing Volume Ratio	122
A.5. Correlation between Evaporation Time and (Length-scale) ²	123
Appendix B. Supporting Information for Chapter 4	124
B.1. Calculations for Scaling Analysis	124
B.2. Calculations of Enhancement Factor in SERS Measurement	124
B.3. Estimating Number of Particles, n, in 30 μm Diameter Patterns	126
Appendix C Supporting Information for Chapter 5	127
C.1. Iterative Solution Schemes	127
C.2. Computational Algorithms	131
C.3. Determination of Total Assembly Time	132
C.4. Determination of Distribution of Initial Particle Displacement	133

List of Figures

Figure 1.1 Lab-on-a-disc. (A) Photograph of a lab-on-a-disc (B) A photo image of the Samsung Blood Analyzer (25(W) × 35(D) × 25(H) cm).....	2
Figure 1.2 Salt Ponds, South San Francisco Bay[101]	5
Figure 2.1 Schematics of the crystallization of the microparticles in a micro open channel.	10
Figure 2.2 SEM images of the assembly of 3- μ m diameter silica microspheres within SU-8 micro-open channel.....	15
Figure 2.3 Sequences of 3- μ m silica assembly at the interface between channel and outlet (channel width: 20 μ m, height: 7 μ m, length: 4 mm). The concentration of particle suspension is 2.5 wt %.....	18
Figure 2.4 Graphs of the crystal growth length (L_c) versus time (left) and the crystal growth rate (v_c) and the ratio of estimated to measured v_c versus the weight fraction of particles (right).	20
Figure 2.5 Fabrication of microparticle self-supported line patterns based on microspheres..	21
Figure 2.6 SEM images of self-supported line patterns based on silica microspheres.....	23
Figure 3.1 Schematics of the self-assembly of the micro particles on a photo-patterned substrate.	29
Figure 3.2 The snapshots of the particle assemblies before the completion of the evaporation... ..	30
Figure 3.3 The magnified views of images from Figure 3.2 at the center of the droplet.	31
Figure 3.4 The images of the patterns of the microparticle assembly (after lift-off).....	33
Figure 3.5 The dependence of the patterning with the concentration of the suspension.. ..	34
Figure 3.6 (a) A cross sectional view of the pattern made from 2.5 wt % of the suspension (silica microspheres, diameter, 1 μ m, 2 μ L). (b) A cross sectional view of the pattern made from 5 wt % of the suspension (silica microspheres, diameter, 1 μ m, 2 μ L).	35
Figure 3.7 Notations for the scaling analysis. (a) Global coordinates with respect to the droplet. (b) Local coordinates with respect to a single pattern. (c) A schematic of the definition of global, local pressure and time.....	37
Figure 3.8 The graphs of the packing volume ratio versus the weight fraction of a suspension.. ..	41
Figure 3.9 The images of the confinement of the particle assembly on a photopatterned substrate without surface treatment (before lift-off)	44
Figure 4.1 Schematics of printing procedure.....	50
Figure 4.2 Optical snopshots of evaporating droplets after the pinch-off. (left) Right after the pinch-off. (right).	54
Figure 4.3 SEM views of gold nanoparticle (diameter ~ 100 nm) clusters printed from 200 μ m head pore size.....	55
Figure 4.4 SEM views of zinc oxide nanoparticle (diameter ~ 30 nm) clusters. (i-iii) 30 μ m diameter clusters printed from 40 μ m head pore size and 40 wt% concentration suspension.....	56
Figure 4.5 SEM views of silica microsphere (diameter 1 μ m) clusters... ..	59
Figure 4.6 SEM views of polystyrene microsphere (diameter 1 μ m) clusters.....	60
Figure 4.7 Multiplexed printing of micro, nanoparticle clusters.	61
Figure 4.8 Multiplexed printing of micro, nanoparticle clusters	62
Figure 5.1 Schematics of printing procedure.....	64

Figure 5.2 Optical snapshots of evaporating droplets after the pinch-off. Evaporation of 5×10^{-3} wt% gold nanoparticle suspension each part corresponds to the part in Figure 5.1.	65
Figure 5.3 Centering of particle assemblies in evaporative self-assembly.	66
Figure 5.4 SEM views of gold nanoparticle (diameter ~ 100 nm) clusters.	70
Figure 5.5 SEM views of silica microsphere (diameter $\sim 1 \mu\text{m}$) clusters.	70
Figure 5.6 SEM views of polystyrene microsphere clusters.	71
Figure 5.7 a. Normalized average inter-particle distance with respect to normalized assembly time. 2 particles, 4 particles and 6 particle-silica particle systems are used. b. Particle assembly time of 10 different sets of 2-particle systems and comparison with the evaporation time of the droplet.	75
Figure 5.8 Particle assembly time with respect to the number of particles	76
Figure 6.1 The patterning process.	80
Figure 6.2 a) Optical micrograph of ZnO nanoparticles in a coffee ring on a cellulose acetate template on silicon. b) SEM micrograph of nanoparticle patterns on a silicon substrate after lift-off. c) Optical micrograph of a released cellulose acetate film.	81
Figure 6.3 SEM micrographs of ZnO nanoparticles on a silicon substrate a) in a large array with 1:1 spacing and b) individually. c) Optical micrograph of ZnO nanoparticles on a COC substrate	83
Figure 6.4 SEM micrographs of ZnO nanoparticles on a silicon substrate, showing a) the variation in height of patterned features directly under the coffee ring and b) small and c) large patterned heights in the center of the patterned area away from the coffee ring	84
Figure 6.5 a) The current response of the sensor under a constant bias of 20V when flashing 365 nm light (0-16 mins) and 254 nm light (after 18 mins). b) A close-up view of the 365 nm light response from part a)	86
Figure 6.6 The experimental data and theory curve-fit for sensor current as a function of a) physical distance of the sensor from the light source, and b) intensity of light reaching the assembly.	89
Figure 6.7 Size tunable printing of dark blue (BB, excitation wavelength: $330 \mu\text{m}$) fluorescence dye tagged-polystyrene microspheres.	91
Figure 6.8 Surface Enhanced Raman Spectroscopy (SERS)-spectrum of trans-1,2-bis(4-pyridyl)-ethylene (BPE) molecules-absorbed on gold nanoparticle clusters.	93
Figure A.1 The nature of particle deposition with respect to different concentrations of the suspension. a-d, (a) 0.3125 wt % (b) 0.625 wt % (c) 1.25 wt %	119
Figure A.2 The images of $3 \mu\text{m}$ silica microspheres based structures (a) Overall view (b) Close view.	120
Figure A.3 The notations for the parameters of the droplet.	121

List of Tables

Table 1.1 Category of Existing Concentrator Systems.....	2
Table 1.2 Properties of Existing Concentrator Systems	4
Table 2.1 Data for measured, estimated crystal growth-length and crystal growth-rate	19
Table 2.2 Data for the measured, estimated crystal growth-rate versus weight fraction of particles in suspension.....	19
Table 5.1 Summary of estimated parameters used for computations	72
Table 5.2 Calculated initial particle displacement, final displacement and center of mass of particle systems for N=2,3,4,5,6. Unit: μm	73
Table 6.1 Summary of data shown in Figure 6.6.c-d.....	94
Table B.1 Enhancement factor calculation	126

Chapter 1. Introduction

1.1. Motivation for Fast Crystallization of Solid-Phase Species in Liquid

Fast crystallization of solid-phase species in liquid medium is a crucial prerequisite to achieve the aims of a number of applications in water purification[1-9], sample preparation for the detection of environmentally hazardous species[10-31], bio-chemical sensing[11, 31-47] and micro-and nano-manufacturing[48-60]. For example, for bio-chemical sensing purposes, various biological species such as mammalian-cells[28, 29], bacterial-cells[2-6, 8, 9, 25, 27-29, 31], viruses[5, 7], airborne microorganisms[10, 12, 13, 15, 23, 24], DNAs(RNA)[22, 33, 44, 46] or proteins[11, 34, 35, 37, 39-43, 45, 47] in liquid medium are required to be crystallized prior to further detection steps. Or, in cutting-edge micro-and nano-manufacturing technologies, significant efforts are made to manipulate, locate, and assemble micro, nanoparticles in targeted areas for numerous applications such as three-dimensional photonic crystals[61-63], circuitry of printed electronics on flexible substrates, conductometric[64, 65], and plasmonic-based biochemical sensors[66, 67]. In those applications, fast crystallization of printed micro-and nano-particle inks is a crucial bottleneck to meet fast, low-cost, low-material consumption requirements. Generally, this fast crystallization step of solid-species in liquid medium involves multi-phase (liquid, gas, and solid phases) flow phenomenon to separate phases: (1) Separation of solid-phase materials from the rest of the phase-materials and (2) Removal of the liquid medium. A number of existing phase-separation systems are grounded upon the physical principles of segregating solid materials from the multi-phase systems by various mechanical and electrical means along with the removal of the liquid-phase medium for the completion of crystallization. In the next chapter, existing phase-separation systems are categorized and briefly overviewed.

1.2. Reviews on Current Phase-Separation Systems

Numerous types of micro-scale, phase-separation systems have been used to accomplish the crystallization of various materials that are addressed in the previous chapter.

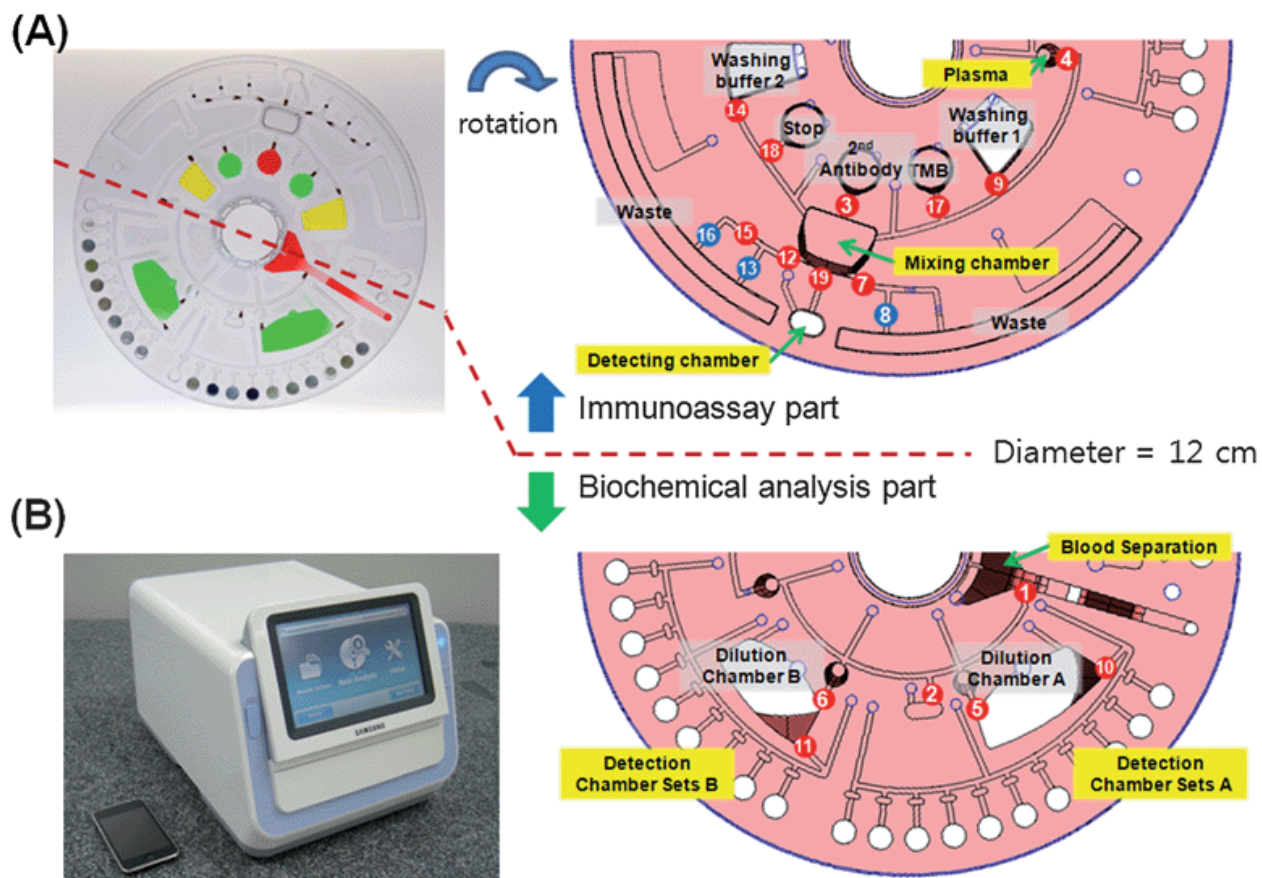


Figure 1.1 Lab-on-a-disc. (A) Photograph of a lab-on-a-disc (B) A photo image of the Samsung Blood Analyzer (25(W) × 35(D) × 25(H) cm)

Figure 1.1 features micro-scale centrifugal systems, a lab-on-a-disc technology. Detection wells on the clinical chemistry side are preloaded with lyophilized reagents. Other chambers for liquid type reagent are loaded with food dye solution for demonstration. In the right hand side, the disc design shows the detailed microfluidic layout. Top half of the disc for the immunoassay part is rotated for easier demonstration. The other half of the disc for the clinical chemistry analysis part is shown in the bottom. Various kinds of biological analytes such as DNA,

proteins, blood plasma and bacterial cells are concentrated, filtered and crystallized by micro-scale, rotational systems. For the convenience of the reader's understanding, the existing phase-separation systems are categorized into four types – centrifugation-based systems[32-45, 47, 68-71], chromatography-based systems[2-4, 11, 16, 17, 26, 30, 31, 72-85], electrophoresis-based systems[13, 15, 18, 28, 29, 86-92] and natural evaporation-based systems[93-101]. They were also critically reviewed with respect to five physical parameters - driving force of solid-phase material crystallization, resistance force of solid-material collection, principle of the separation of the liquid medium from solid-phase materials, principle of the removal of the liquid medium and power supply method of the system-as summarized in Table 1.1.

Table 1.1 Category of Existing Phase-Separation Systems

	Driving force of crystallization of solid-phase materials	Resistance force of solid-phase material collection	Principle of separation of the liquid medium from solid-phase materials	Principle of removal of liquid medium	External power supply method of the system
Centrifugation-based	Centrifugal force	Drag force by surrounding fluid	Gravitational sedimentation of particles	Extraction by hydrodynamic pressure	DC / AC electrical supply
Chromatography-based	Capillary force	Drag force by surrounding fluid	Evaporation of liquid	Evaporation of liquid	None
Electrophoresis-based	Electrostatic force between particle surface and the surrounding fluid	Drag force by surrounding fluid and electrophoretic retardation force	Sieving mechanism of gel materials	None	DC / AC electrical supply
Evaporation-based	Particle-attractive force	Drag force by fluid	Evaporation of liquid	Evaporation of liquid	None

As shown in Table 1.1, natural evaporation-based methods possess unique advantages such that there is no need to implement external power supplies to obtain crystallized substances. Several aspects of the crystallization step of those existing technologies, such as required minimum initial concentration of analytes, crystallization time, sample volume and used materials are critically reviewed in Table 1.2.

Table 1.2 Properties of the Crystallization of Existing Phase-Separation Systems

	Reported minimum detectable concentration of analyte	Crystallization time	Sample volume	Used materials
Centrifugation-based[36]	~ 0.1 pM	30 s ~ 60 min	2 ~ 550 μ L	Bacterial cells, Protein, DNA(RNA), Virus
Chromatography-based (HPLC)[102]	0.03 μ g/mL	5 ~ 25 min	1 ~ 10 mL	Organic chemicals, DNA(RNA), Protein,
Electrophoresis-based (Gel electrophoresis)[92, 103]	0.68 nM	2 ~ 16 hours	30 μ L ~ 1.5 mL	DNA(RNA), Protein
Natural evaporation-based[40, 93-97, 99-101]	All range of concentrations	From second scale to week-scale	From mm ² scales to 10,000 Acres-scale	Salts, Crystallized ions

As shown in Table 1.2, natural evaporation-based concentration methods utilize a wide range of concentrations, crystallization time and sample volume compared to other existing technologies.



Figure 1.2 Salt Ponds, South San Francisco Bay[101]

Figure 1.2 shows the large coverage of salt ponds which is the representative example of natural evaporation-based crystallization method. However, its applications have been still limited to obtaining sea salts or crystallized ions and its virtues that the wide range of analyte- concentration, sample volume can be used to achieve fast crystallization of analytes for the assay or the fabrication of micro-and nano-scale devices have not been actively explored. Also, generality of applicable materials – from micro-and nano-scale particles to biological species such as bacterial cells, protein, DNA(RNA), also has not been emphasized and numerous applications which can potentially stem from natural evaporation-based crystallization systems have not been envisioned yet. In the next chapter, evaporative self-assembly of micro- and nano-scale particles is introduced as a new

possible tool to develop novel ways of achieving fast crystallization of micro-and nano-particles via natural evaporation of liquid medium.

1.3. Introduction of Evaporative Self-Assembly of Micro-and Nano-Particles

A number of self-assembly techniques of micro-and nano-particles have been developed based on electrostatic force[104], electrochemical reactions[105, 106], surface functionalization and microfluidics[60, 98, 107, 108]. Especially, fluidic self-assembly is emerging as a promising pathway to guide and assemble micro structures due to its high yield and great simplicity[109]. It is reported that particles in millimeter-scale[110], and micro-scale[96] in fluid can be assembled and structured by lateral-capillary forces between the particles in suspension. This type of assembly refers to “Evaporative Self-Assembly”. In this dissertation, for chapters 2 - 4, three types of micro mechanical systems that enable fast crystallization of micro-and nano-particles are demonstrated based on evaporative self-assembly. Evaporative flows such as open-channel flow, thin liquid-film flow and fast, micro-scale evaporative liquid flow on hydrophobic surface are driving fast concentration and crystallization of the particles in micro mechanical systems within 5 minute. Micro-and nano-particles are chosen as adequate modeling materials to describe the crystallizing behavior of particle assembly because their geometries are controllable and uniform and their motions are easily interpretable by conventional hydrodynamics and particle dynamics. Critical parameters for the analysis of colloidal motions in evaporative flows are identified by conventional thermo-coupled fluid mechanics for each system. In chapter 5, numerical values of those parameters are accurately calculated by particle-dynamic incorporated-computations and interpreted with experimental results to provide accounts for particle effects in evaporative self-assembly. In chapter 6, electrical and optical characterization of crystallized 3D particle assemblies are performed to demonstrate the feasibility of the developed systems for rapid, direct characterizations of various target species.

Chapter 2. Constrained Microparticle Assembly by Open-Channel Flow

2.1. Introduction

A simple, ultrafast microfluidic approach to crystallize microparticles in a constrained micro-fluidic channel is introduced on the basis of the photolithography and capillary action of microparticle-dispersed suspensions[48]. There have been several attempts to control the crystallization of 2D microparticle assembly from the liquid suspension of microparticles[60, 97, 98, 107, 111-113]. In particular cases, the crystallization of the microparticles was achieved in confined geometries by either receding a contact line[60, 112] or electrostatic forces[111], and the particles were transported from the suspension to fill the trenches. These approaches require the fine control of the receding speed of the contact line and the contact angle of the meniscus of the fluid with respect to substrates. Also, the release of crystallized particle assemblies in the confined geometries, a crucial issue in the integration of on-chip particle assemblies with other micro-scale electronic devices, was not demonstrated. In this chapter, various sizes(diameter|1-5 μm) of silica microspheres and silica gel microspheres was successfully crystallized within open micro channel with a small cross-sectional area and a long length by using this approach. Also, microsphere-crystallized line patterns were fabricated by dissolving the photoresist that was used to guide the open-channel flow. In addition, the crystallization speed was estimated theoretically, and the discrepancy with experimental results was discussed.

2.2. Experimental Methods

2.2.1. Materials

A liquid suspension of silica microspheres (silicon dioxide-based microparticles; diameter, 3 and 5 μm , water, 95 wt%, silica, 5 wt%, Sigma-Aldrich) was diluted

into various concentrations of suspension (2.5, 1.25, 0.625, 0.3125 wt% silica) by adding a controlled volume of deionized water. Dried silica gel spheres with a diameter of 3 μm , a pore size of 6 nm, and a distribution of diameters (D10, 2.15 μm ; D50, 3.40 μm , and D90, 6.42 μm) (SiliaSphere, Silicycle) were mixed with a controlled volume of deionized water to form suspension of 1.25 wt% silica gel and 98.75 wt% water.

2.2.2. Design and Fabrication of Open Microchannel

Two reservoirs and the channel geometry were designed. For inlet/outlet reservoirs, 20 mm \times 20 mm \times 7 μm (width \times length \times height) rectangular patterns were defined to contain a 0.2 μL volume of suspension with 0.3125 – 2.5 wt% concentration of particles without overflow. For channels, various widths (10, 13, 16, 20, 40 and 60 μm) and lengths (2, 3, 4, 5, 6, 7 and 8 mm) were combined with fixed height (7 μm). The open microchannel was fabricated by UV photolithography. Lightly doped p-type silicon wafer (Silicon Quest International Inc.) was used as a substrate and SU-8 2007 (Microchem Corp.) and SPR 220-7 (Megaposit) were used as UV-sensitive photoresists. For the SU-8 channel, the resist was spin coated on a silicon substrate at 3000 rpm for 30 s (thickness|7 μm) and soft baked at 95 $^{\circ}\text{C}$ for 3 min. After UV-light exposure, the sample was baked at 95 $^{\circ}\text{C}$ for 3 min for post-exposure bake and developed for 1 min. For SPR 220-7 channels, the resist was spin coated onto a silicon substrate at 2200 rpm for 30 s (thickness|10 μm) and soft baked at 115 $^{\circ}\text{C}$ for 5 min. After UV-light exposure, the sample was developed for 4 min. After the lithography step, oxygen plasma treatment (50 W, 260 mTorr, 30 s) enhanced the hydrophilicity of the channel wall and substrate.

2.2.3. Patterning of Microparticles

All the patterning experiments on the open micro channel were conducted in an air environment at atmospheric pressure and room temperature conditions. A micro syringe (Microliter Syringes 5 μL , HAMILTON) was used to extract a small volume (0.2 μL) of the microparticle solution in the inlet reservoir. After the

particle assembly was completed, the sample was held at room temperature for 1 h to evaporate the solvent completely and the resist was dissolved by PRS 3000 (*J.T. Baker*) in case of the SPR 220-7 micro-open channel.

2.2.4. Imaging

The samples were imaged by optical microscope (Polylite 88, Reichert-Jung) and scanning electron microscopy (LEO 1550, *ZEISS*). A cross section of the channel was imaged after the sample was coated via the sputtering of a Au / Pd thin film.

2.3. Principles of Self-Assembly of Microparticles

Figure 2.1 illustrated the sequential processes of self-assembly in the open microchannel. The self-assembly of microparticles in the micro-open channel was divided into three steps: (1) initiation of particle nucleation (Figure 2.1.c); (2) crystal growth of particle nucleus (Figure 2.1.d); (3) completion of crystal growth followed by medium evaporation (Figure 2.1.e,f). The capillary immersion force generated a strong attractive force between the particles when the fluid thickness reaches the particle diameter (D) if $D \leq 5 \mu\text{m}$. If the capillary pressure from the suspension droplet is sufficient to be maintained throughout the channel, then the medium is driven by the surface tension of channel and flows along the channel. The thickness of the medium film sharply decreased at the interface between the channel and outlet because of the divergence of the medium flow. Then, the particles were attracted to each other and nucleated at the interface. After the onset of particle nucleation, a convective flux of particles from the channel inlet to the ordered particle nucleus propagated the particle assembly by crystal growth. The convective flux of particles was generated by two sources: evaporation of the medium and capillary action of the medium. The evaporation of the medium occurred rapidly at the particle nucleus where menisci of the medium were formed around the particles.

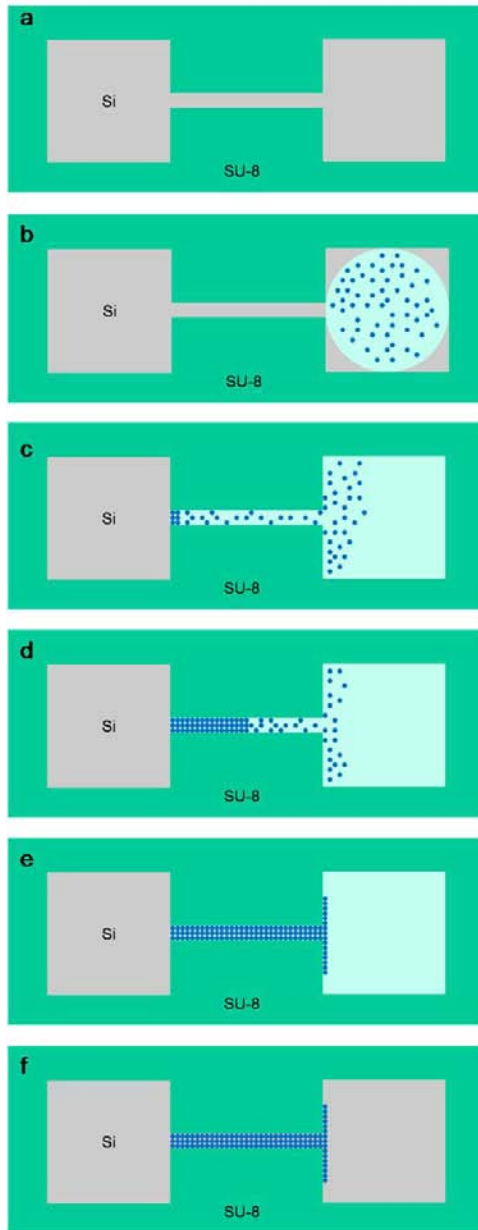


Figure 2.1 Schematics of the crystallization of the microparticles in a micro open channel. (a) SU-8 micro-open channel fabricated on the silicon substrate. (b) Microparticle -dispersed suspension placed on the inlet of the micro-open channel. (c) The suspension is driven by the surface tension, and the particles stop at the interface between the channel and outlet and crystallization starts. (d) Particle crystallization develops. (e) Crystallization is completed. (f) Medium is evaporated.

These menisci prevented the further thinning of the medium layer in the nucleus, and an intensive medium flux from the thicker part of the medium layer was generated to compensate for medium evaporation at the nucleus. The capillary

action of the medium was caused by the Young-Laplace capillary pressure on the micro-scale. The high surface tension of the substrate and sidewall of the channels, after O₂ plasma treatment, can induce a high medium flux from a droplet in the channel inlet in the micro-scale open channel. Therefore, the medium flux by both the evaporation of the medium at the nucleus and the capillary pressure of the medium carried the suspended particles toward the nucleus and resulted in fast particle assembly (The assembly time was 24 s in an open microchannel where the width was 20 μm, the height was 7 μm and the length was 4 mm). After the nucleus was propagated to the inlet of the channel, the medium in the nucleus evaporated completely and particle assembly was completed within defined microchannel geometries.

2.4. Theoretical Calculation of Assembly Speed

The crystal-growth rate of particle assembly can be theoretically estimated by combining the model of convective assembly of colloid particles[97] with the open-channel flow model[114]. On the basis of Dimitrov's model[97], the crystal-growth rate of convective particle assembly at steady-state, v_c , was expressed in terms of the macroscopic mean velocity of water, v_{wt} , mean evaporative flux of the medium from assembled particles, j_e , medium film thickness, h , leading edge of medium thickness, h_f , distance between the leading edge of the medium film and inlet reservoir, l , porosity of particle assembly, ε , and volume fraction of particles in suspension, ϕ .

$$v_c = \frac{\beta h_f v_{wt} \phi}{h(1-\varepsilon)} = \frac{\beta j_e l \phi}{h(1-\varepsilon)(1-\phi)} \quad (2.1)$$

The mean evaporative flux of the medium from assembled particles, j_e , was defined as $\frac{\int_0^\infty j_e(z) dz}{l}$, where z refers to the axis of propagation of particle assembly and β is the coefficient that depends on the particle-particle and particle-substrate interactions and varies from 0 to 1. If the interactions are stronger, then the value of β increases. For nonadsorbing particles such as silica particles or diluted suspensions, β approaches 1. As mentioned above, the medium flow in an open-

channel is mainly driven by two sources: capillary flow driven by surface tension and enhanced evaporation of water by the meniscus effect in particle assembly. Because it is difficult to measure j_e experimentally, another strategy was needed to quantify the contribution of capillary channel flow to the enhancement of the crystal-growth rate. v_c at the interface between the outlet and channel was theoretically estimated on the basis of the assumption that the capillary flow was the only source to drive water flow inside the channel. The volume flow rate of water in the open-channel, Q , by capillary pressure only was expressed as[114]

$$Q = \frac{1}{\eta} \frac{\Delta P}{R_{fr}} \quad (2.2)$$

$$R_{fr} = \frac{12L}{R_h^2 A} (1 - 1.3553a + 1.9467a^2 - 1.7012a^3 + 0.9564a^4 - 0.2537a^5) \quad (2.3)$$

where η is the viscosity of the liquid, ΔP is the difference of pressure between the two liquid fronts, L is the filled length of the channel, R_h is the hydraulic radius of the channel, A is the cross-sectional area of the channel, and a is the aspect ratio of the channel. The aspect ratio was defined as either height/width or width/height such that $0 \leq a \leq 1$. The capillary pressure that is equivalent to ΔP in the flow direction (z) of the open-microchannel can be described as[114]

$$P_{c,z} = \gamma \left(\frac{\cos \alpha_b}{d} + \frac{\cos \alpha_l + \cos \alpha_r}{w} \right) \quad (2.4)$$

where γ is the surface tension of a liquid and α_b , α_l and α_r are the contact angles of the liquid on the bottom, left, right walls, respectively. d and w are the depth and width of a micro-channel.

Therefore, v_{wt} and v_c by the capillary flow of water is

$$v_{wt_capillary} = \frac{1}{\eta A} \frac{P_{c,z}}{R_{fr}} \quad (2.5)$$

$$v_{c_capillary} = \frac{\beta h_f v_{wt_capillary} \phi}{h(1-\varepsilon)} \quad (2.6)$$

It is important to note that the estimated $v_{c_capillary}$, according to the formulations above, is valid mainly at the interface between the channel and outlet. The natural evaporation of water in a suspension-droplet in the inlet-reservoir increases the concentration of solutes in the suspension as crystal-growth proceeds. However, this effect was not included in the formulation. Also, the loss of a pressure gradient caused by crystallized columns was not considered in the formulations. $v_{c_capillary}$ is denoted as v_c in this chapter for simplicity. The discrepancy between the theoretically estimated v_c and the measured v_c is discussed in the chapter 2.5.

2.5. Analysis on Experimental Results

2.5.1. Commensurable Effect

Figure 2.2 showed that the silica microspheres are assembled tightly within the micro open channel in three-directions: horizontal (x axis) and vertical (y axis) directions in the plane of channel cross section and in the direction of the channel length (z axis) by using the presented technique. The crystal growth of particles after the initial nucleation was governed by forces in three directions: horizontal and vertical by the evaporation of the medium and in the direction of the channel by the capillary action of the medium. Also, the interface between the channel and outlet reservoir was sharply defined and no particle overflow was found, which is consistent with the claim that the nucleation of particles begins where the thickness of the water film is reduced to the particle diameter. The commensurable effect of silica microspheres in the open microchannel was examined in more detail by varying the width of the channel and the diameter of silica particles. At first, the number of particles across the channel width was increased by one as the width of the channel increased by the particle diameter. Because the assembly of particles was achieved to minimize the porosity, the number of complete particles across the width ($= N_1$) was equal to $f[\frac{W \text{ (Width)}}{D \text{ (Particle Diameter)}}]$ where function $f[x]$ returns the largest integer less than or equal to x . It was shown that the number of particles across the channel height decreased as the channel aspect ratio ($\frac{H \text{ (Channel Height)}}{w \text{ (Channel Width)}}$) decreased although we anticipated the number of particles ($= N_2$) across the

channel would be the same as $f\left[\frac{H(\text{Height})}{D(\text{Particle Diameter})}\right]$ regardless of the channel widths. It was speculated that the geometry of the interface between the suspension and air affected the nature of self-assembly. Inside the channel with a lower aspect-ratio, a thinner-medium film was formed because the contact angle of water with respect to the channel sidewall remained constant even if the channel width changed. Consequently, a thinner medium film carried and assembled fewer particles in vertical scale. Therefore, not only the height of the channel, but also the geometry of suspension interface with air determined the number of silica layers on the vertical scale. When the size of the microspheres was increased from 3 to 5 μm , the number of particles in on both horizontal and vertical scales was decreased.

Silica gel microspheres that are widely used materials in conventional chromatography were self-assembled by using the presented technique. The solid-state silica gel particles were diluted with the medium, and a droplet of the acquired suspension was applied to the channel. Although silica gel particles showed a wider distribution of diameters and have water-absorbing properties, the interface between the assembled structures and outlet reservoir was clearly defined and the particles were assembled tightly, as shown in Figure 2.1. It showed that particle assembly occurred in both the vertical and horizontal direction with respect to the channel width simultaneously, not sequentially. It is noteworthy that various microparticles can be self-assembled according to the channel geometry because the pathway and the height of the fluid-state medium determined the 3D geometry of the assembled structure. The 3D assembly of microparticles was easily structured within a micro-open channel whose geometry can be easily controlled by photolithographic processes. The self-assembly of microparticles in various geometries was also demonstrated in Figure 2.2.e.

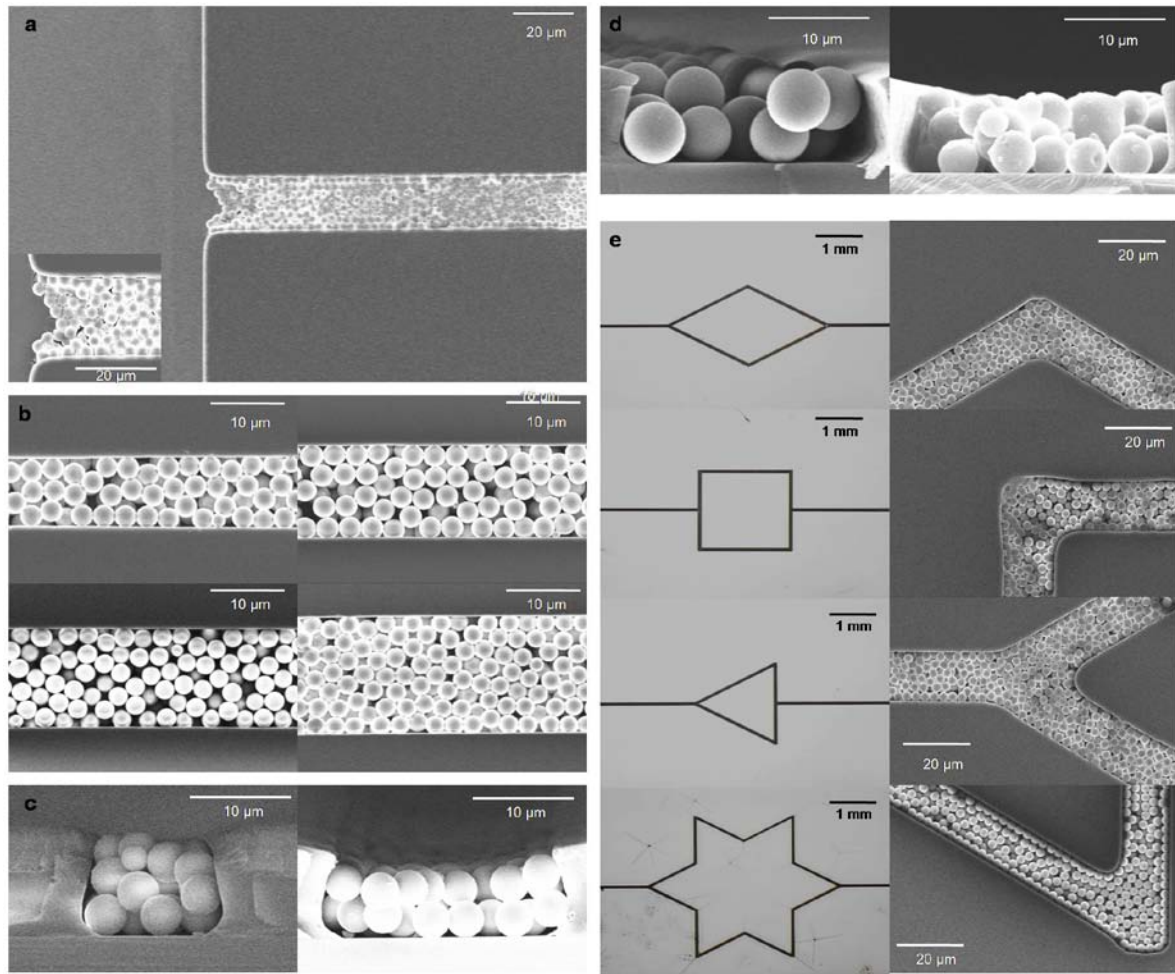


Figure 2.2 SEM images of the assembly of 3- μm diameter silica microspheres within SU-8 micro-open channel. (a) Interface between the channel and outlet reservoir. The channel width is 20 μm , the height is 7 μm and the length is 4 mm. The outlet reservoir is 2 mm \times 2 mm \times 7 μm (height). (b) Commensurable effect of silica microspheres on a horizontal scale. The widths of the channels are 10 μm (top left), 13 μm (top right), 16 μm (bottom left) and 20 μm (bottom right). The length (3 mm) and height (7 μm) of four micro channels are identical. The numbers of particle layers are three (top left), four (top right), five (bottom left), and six (bottom right). (c) Commensurable effect of 3 μm silica microspheres on a vertical scale. (d) Cross section view of 5- μm silica microspheres (left) and 3 μm silica gel microspheres (right). The widths of the channels are 20 μm (right). Optical microscope (left column) and SEM (right column) images of assembled silica microsphere structures in rhombus-shaped (top), square-shaped (upper middle), triangle-shaped (lower middle) and star-shaped (bottom) channels. The SEM images in the right column represent particle assemblies at the diverted paths of channels.

2.5.2. Theoretical Analysis

Data on the length of crystal growth versus time was obtained by taking snapshots of the crystallization of silica microspheres in open microchannel with an optical microscope. Detailed data are available in Table 2.1 and Table 2.2. Calculation of the theoretically estimated length of crystal growth was performed based on the model provided in the previous section. First, crystal-growth-rate, v_c , was calculated and integrated it to obtain the length of crystal growth, L_c . Also, the relation between the weight fraction of particles in a liquid suspension and v_c was obtained and the discrepancy between the measured and estimated v_c was observed. As shown in Figure 2.3, the theoretically estimated L_c and measured L_c values are similar to each other at the beginning of crystallization, however, they start to show larger discrepancy later on. The slope of the graph which indicates that v_c changes drastically from lower to higher in the middle of crystallization in the measured L_c , and the estimated L_c shows the trend of a linear increase until the completion of crystallization. Because of the rapid increase in measured v_c , the overall times required for crystallization for both the theoretical estimation and experiments are similar although the dynamics of v_c is different during the crystallization. The discrepancy between estimated and measured L_c is attributed to the effects of natural evaporation of droplets and the loss of a pressure gradient caused by the crystallized column. The significant decrease in measured v_c after initial crystallization is caused by the effect of the loss of the pressure gradient. This loss increases as the crystallization proceeds, thus, v_c also decreases. Although the loss of the pressure gradient increases until the completion of crystallization, because of the natural evaporation of the medium in suspension, the concentration of particles in suspension increases and v_c increases. The significant upsurge of concerning v_c is caused by the nonlinear nature of the evaporation of the medium. Although quantitative characterization of the evaporative power of the medium in a suspension-droplet was not estimated with respect to time, it was observed that the evaporative rate increases drastically as the droplet evaporates because the surface-to-volume-ratio of a single droplet also increases. Therefore, it is speculated that this nonlinear increase in the evaporative power of the medium in the suspension droplet drives the significant increase in v_c in spite of the larger loss

of the pressure gradient in the late stage of crystallization. As stated in chapter 2.5, the effects of the natural evaporation of a droplet and the loss of the pressure gradient caused by the crystallized column were not considered in the theoretical modeling; therefore, the discrepancy between the estimated and the measured L_c was observed in the middle of the crystallization. However, in an early stage of crystallization, when the crystallized particles dwell at the interface between the outlet reservoir and channel, the estimated v_c agrees well with the measured one because the pressure loss caused by the crystallized column is not large and the evaporative rate of the droplet is also negligible. The ratio of the estimated to measured v_c was calculated at the point where the first two snapshots of crystallization were taken. It was maintained at about 0.7~0.8 throughout all of the fractions of particles, implying that the theoretical model is valid around the interface between the outlet reservoir and the channel and also that the contribution of capillary action of flow to crystal-growth is more dominant than the evaporation of the medium at the interface. Therefore, it was concluded that the surface treatment of the channel by oxygen plasma is very critical to achieving the high-speed crystallization of particles in an open micro channel. The estimated crystal growth-rate, v_c was obtained by the theoretical model and the measured v_c was obtained from measuring the displacement of crystallized columns from the first two snapshots of crystallization of particles. The channel width was 20 μm , the height was 10 μm and the length was 4 mm. The suspension volume was 0.2 μL and summarized in Table 2.1.

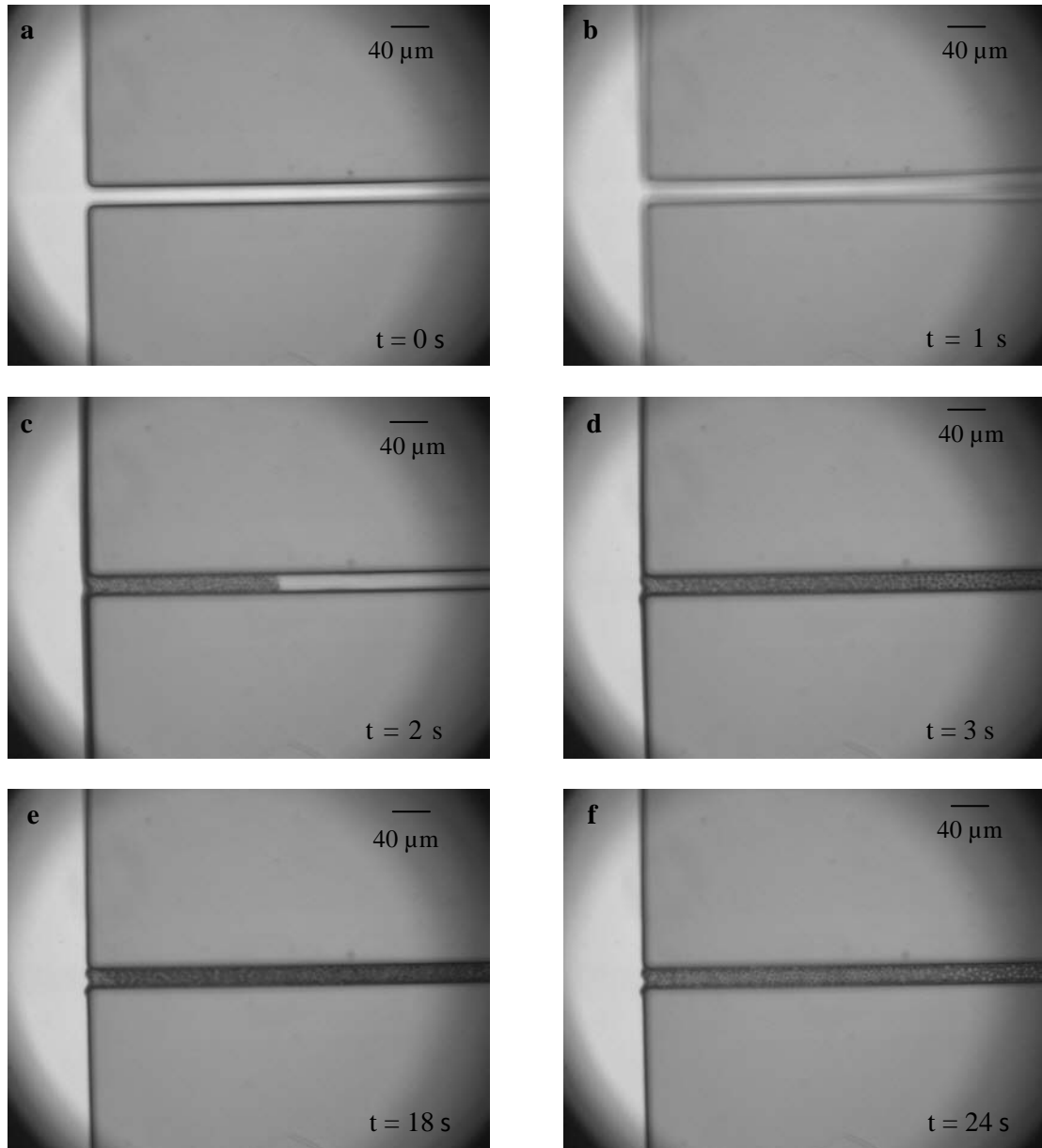


Figure 2.3 Sequences of 3 μm silica assembly at the interface between channel and outlet (channel width: 20 μm , height: 7 μm , length: 4 mm). The concentration of particle suspension is 2.5 wt%. (a) The suspension droplet is placed in the inlet (b) The suspension proceeds along the channel. (c) The silica particles are nucleated from the channel-outlet interface. Medium overflows while particles do not. (d) The nucleation of particles propagates via the crystallization. (e) The evaporation of medium starts from the interface between the outlet and inlet channel. (f) The evaporation of medium over observed distance of the channel is completed.

Table 2.1 Data for measured, estimated crystal growth-length and crystal growth-rate

Time(s)	Measured L_c (μm)	Measured v_c ($\mu\text{m/s}$)	Estimated v_c ($\mu\text{m/s}$)	Estimated L_c (μm)
0	140			
1	350	210	182	182
2	460	110	187	370
3	540	80	192	562
4	570	30	193	756
5	590	20	195	951
6	610	20	196	1150
7	630	20	197	1340
8	640	10	197	1540
9	680	40	200	1740
10	700	20	201	1940
11	720	20	203	2140
12	760	40	205	2350
13	780	20	207	2560
14	810	30	209	2770
15	860	50	212	2980
16	910	50	215	3190
17	960	50	219	3410
18	1040	80	225	3640
19	1220	180	239	3880
20	1600	380	277	4150
21	2000	400		
22	2400	400		
23	2800	400		
24	4000	1200		

Table 2.2 Data for the measured, estimated crystal growth-rate versus weight fraction of particles in suspension

Fraction (wt%)	Estimated v_c ($\mu\text{m/s}$)	Measured v_c ($\mu\text{m/s}$)	(Estimated v_c)/ (Measured v_c)
0.3125	20	30	0.67
0.625	42	50	0.84
1.25	88	120	0.73
2.5	170	210	0.81

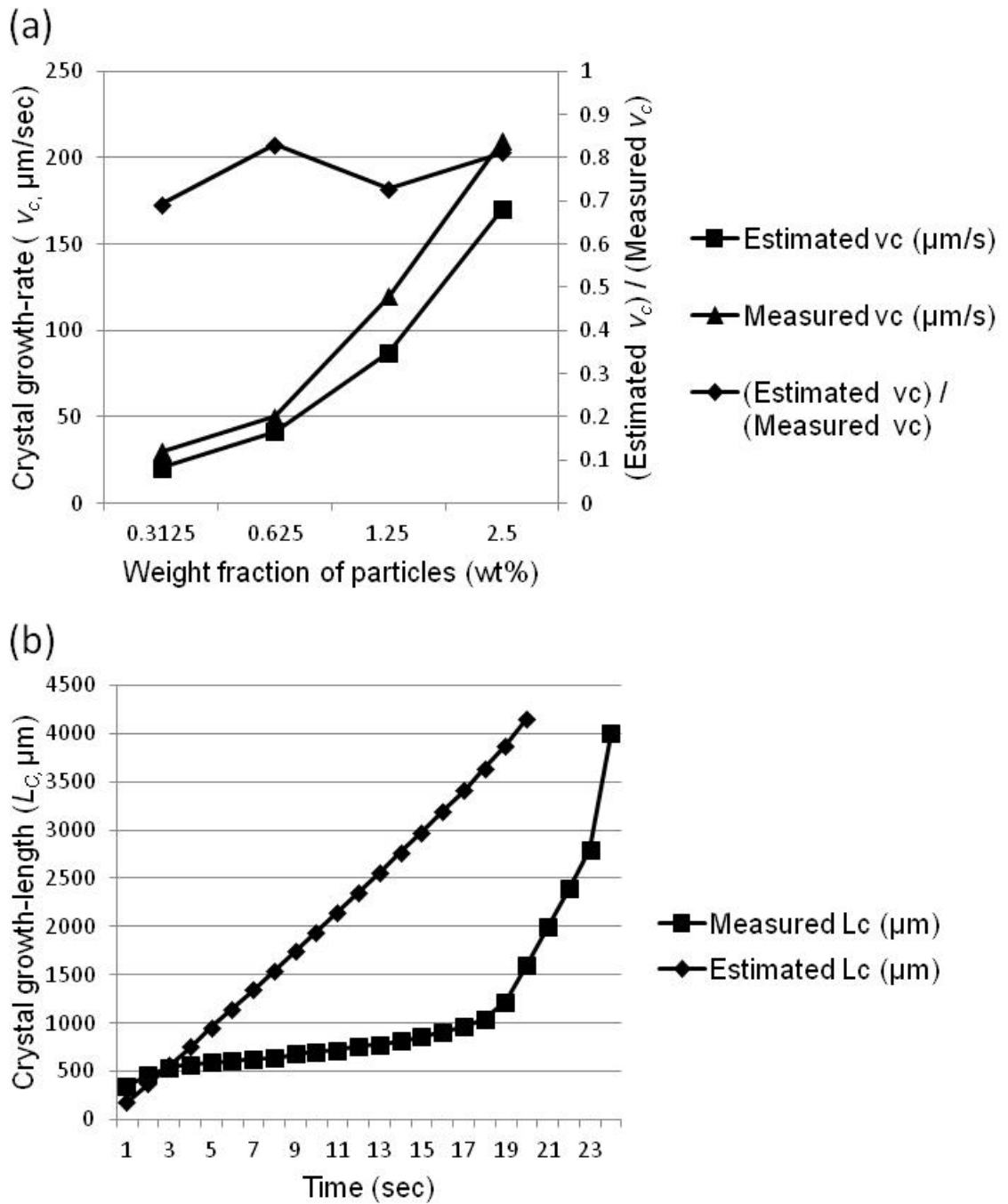


Figure 2.4 Graphs of the crystal growth length (L_c) versus time (left) and the crystal growth rate (v_c) and the ratio of estimated to measured v_c versus the weight fraction of particles (right).

2.5.3. Release of Particle Assembly

Self-supported line patterns based on the assembly of silica microspheres were fabricated by flowing silica suspension in the photoresist-based open-channel and subsequent removal of the photoresist by solvent. A thick photo-resist (SPR 220-7, MEGAPOSIT, depth|10 μm) was used to define the channel geometry and it is dissolved by nonpolar solvent (PRS 3000, J.T. Baker) after the particle assembly is completed. Single and multichannel patterns have been used in this patterning. Both ends of the open micro channel were designed to be closed in order to prevent the flow in one channel from being disturbed by the outflows from other channels. The droplet is placed at one end of the channels as shown in Figure 2.5.

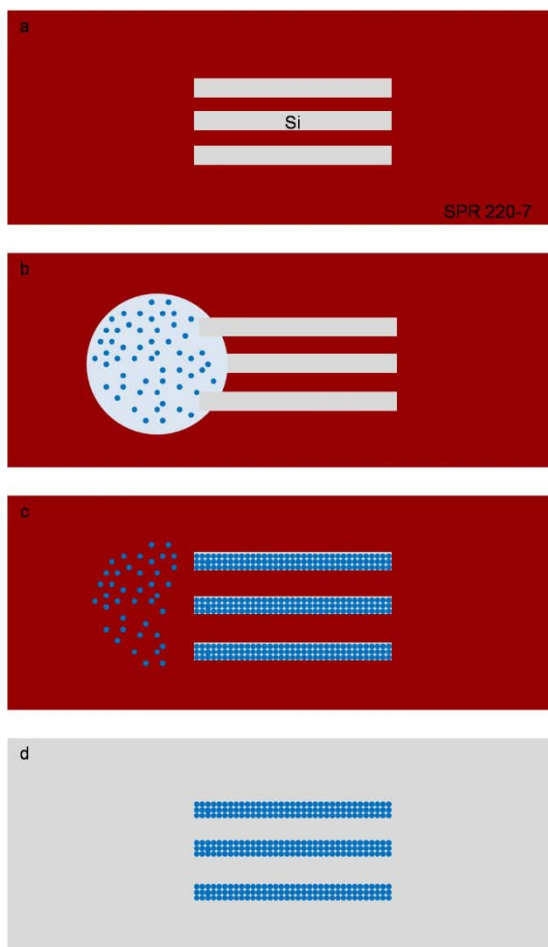


Figure 2.5 Fabrication of microparticle self-supported line patterns based on microspheres. (a) Multiple (or single) lines were patterned onto photoresist. (b) Droplets of the liquid suspension were placed on one end of the channel. (c) Particles were assembled inside the line patterns. (d) The photoresist was dissolved and a particle assembly is formed.

In spite of the expected higher flow resistance at the end of the channels, close packing of particles was achieved over the entire length of lines as shown in Figure 2.6. It was also observed that the crystallization of particles starts at the end of the channel in the case of a closed channel, which was observed in an open channel as well. Once the medium reached the end of channel, the thickness of the medium was forced to decrease in order to satisfy the continuity of fluid. This significant decrease in the flow started at the end of channel, thus, the crystallization also began there. The particles were completely filled from the front end of the channel, the furthest point from the droplet to the rear end of the channel, inside the droplet, without any depletion of particles. It is noteworthy that the packing structure can be preserved without any perturbation during the removal process of the photoresist. The assembled structure was preserved when the diameter of silica microspheres was 3 μm or less. However, the structure was perturbed when the diameter of microspheres was 5 μm or larger. If the particle size decreases, then the surface-to-volume-ratio and the contact-area increases, thus a stronger Van der Waals force may preserve the particle assembly intact. Also, the surface charge condition of particles is another crucial factor in the stability of the structures. The microstructure based on polystyrene microspheres (diameter|1 μm) is deteriorated after the photoresist removal. From these observations, one can conclude that the interparticle forces of assembled structure are dependent on the surface charge property of particles as well. Negatively charged colloidal particles, such as polystyrene, cannot withstand the resist-removal process because the interparticle electrostatic repulsion force is stronger than the attractive force in nonpolar solvents[115]. It is anticipated that the smaller, insulating, or semiconducting particles will be more advantageous in line patterning than the larger and metallic particles. Another interesting feature is the dependence of pattern shape on the number of microchannels when the same volume of microparticle suspension is used. Whereas a meniscus effect of the fluid-channel wall interface was not observed in the patterning of single channels, a huge meniscus effect was found in the multichannel patterning and the thickness of the pattern at the center of the channel was decreasing. This dependence was caused by the difference of capillary pressure at the inlet. In single channels, the dispensing port has a relatively large wetted perimeter compared to the microchannels and the driving pressure was

equal to the capillary pressure between two liquid fronts as discussed previously[114]. However, in multi-channels, the perimeter of the suspension droplet per channel was not as sufficient as that for a single-channel case, thus resulting in the decrease of capillary pressure. Therefore, a thinner medium flow will be established, and this flow drives fewer particles and forms a thinner particle assembly. This patterning process is expected to be easily extended to multilayer processes and integrated with other IC processes because the geometry of the assembly can be easily tuned by setting the resist thickness and channel features, and an accurate alignment can be achieved.

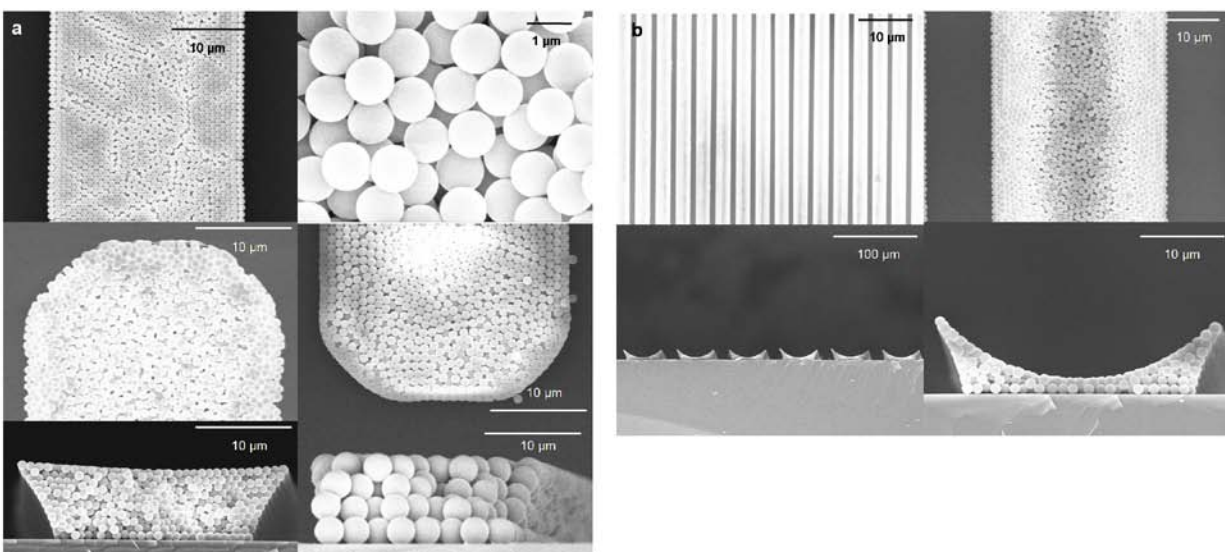


Figure 2.6 SEM images of self-supported line patterns based on silica microspheres. (a) Line patterns generated by a single channel. (Center, Top left) Close view of assembled particles (top right), front end (middle left), bottom end (middle right), cross-sectional views of a 1 μm silica microspheres- based line (low left) and cross-sectional view of 3 μm silica microspheres (low right). The length (4 mm) and width (20 μm) of channels and volume of a droplet (0.2 μL) are fixed. (b) Line patterns generated by multichannels based on 1 μm silica microspheres. Top view of the overall pattern (top left) and magnified view (top right) of the line patterns. Cross section view of the overall (lower left) and individual lines (lower right).

Chapter 3. Templated Micro, Nanoparticle Assembly by Thin-Liquid Film Flow

3.1. Introduction

Creating regular, repetitive, and well-defined three dimensional patterns of crystallized particle assemblies in targeted area is a major bottleneck in various applications such as the fabrication of 3D photonic crystals[61-63], printed electronics on flexible substrate[64, 65], colloidal quantum dot-based devices for display[116-118], plasmonics[66, 67], and so forth. Previous approaches to pattern crystallized particle assemblies, however, are required to use entire substrates without selective positioning of the assemblies[96], chemically pre-patterned substrates[119-121], or soft-lithographic methods where applicable particles are largely constrained by molds and substrates[53, 98, 122]. There have been several attempts to control the crystallization of 2D micro, nanoparticle assembly from a liquid suspension[53, 60, 86, 96, 98, 110-112, 123-127]. In particular cases, the particles have been confined in various geometries of trenches by several approaches such as receding a contact line[60, 112, 126], electrostatic force[111], or assisted directed evaporation-induced self-assembly (ADEISA)[123, 124, 127] and the particles have been transported from the suspension to fill the trenches in as a result. In particular, it is reported that evaporation induced self-assembly of microparticles on modulated thickness show superb optical quality from which even intense optical reflectance spectra was measured[123, 124, 127]. These approaches require the fine control of the receding speed of contact line, the contact angle of meniscus of fluid with respect to the substrates[60, 111, 112, 126] or an additional agitation of suspension with a long-channel, geometrical constraint[123, 124, 127]. Also, the release of the crystallized particle assemblies in the confined geometries, a crucial issue in the integration of the on-chip particle assembly with other microelectronic devices, was not demonstrated yet. Moreover, most of the previous techniques are grounded on 2D interaction between the substrates and particle assemblies; thus, structuring 3D crystallized particle assemblies has been a huge challenge with those approaches. Evaporative self-assembly of meso, micro, and nanoscale particles[96, 107, 110, 125] is well known;

interesting physical phenomenon at three-phase boundaries (particle-medium-air) and its applications have been mainly restricted to fabricate planar structures because technical difficulty lies in controlling interaction between the medium and the particles in 3D[115, 128-142]. In this chapter, a unique and counterintuitive idea is introduced that the coffee-ring effect of an evaporating suspension can offer a governing method to create 3D crystallized patterns of micro/nanoparticle assembly via evaporative self-assembly[49]. At first, the principle of the process is presented with qualitative descriptions. Provided the principle of the patterning, the patterns of 3D assembly of various sizes of microparticles (Silica), metal oxide nanoparticles (TiO_2 , ZnO), and metallic nanoparticles (Ag) have been successfully fabricated by an evaporating, low-concentration particle suspension on the photopatterned substrate with proper surface treatment without any thermal or electrical sintering processes. Also, the geometries of the patterns were finely controlled by adjusting the parameters of the process. Then, the validity of the process is critically studied in-depth with the scaling analysis of main parameters of the process and the scaling effect, the effect of the volume, the concentration of the suspension, and the effect of surface treatment on the patterning are discussed as well.

3.2. Experimental Methods

3.2.1. Materials

A liquid suspension of silica microspheres (Silicon dioxide-based micro particles; diameter, 0.5, 1, 3, and 5 μm ; water, 95 wt%; silica: 5 wt%, Sigma-Aldrich), Titanium oxide nanoparticles (diameter, 70 nm; water, 90 wt%; TiO_2 , 10 wt%; Sigma-Aldrich), zinc oxide nanoparticles (diameter, 30 nm; water, 60 wt%; ZnO , 40 wt%; MK nano) were diluted into various concentrations of suspension (2.5, 1.25, 0.625, and 0.3125 wt% silica) by adding a controlled volume of deionized water. A liquid suspension of silver nanoparticles (diameter, 7 nm; toluene, 70 wt%, Ag, 30 wt%) was synthesized according to the recipe in the literature.

3.2.2. Design and Fabrication of Photopatterned Substrate

Various geometries of photomasks have been designed for the patterning. Various widths (4, 10, 20, 60 and 100 μm) and heights (2, 5, 10, 30, 50 μm) have been defined and the combination of the width and the height of the trenches was chosen in a way the high-aspect ratio is constant to 0.5 while the length of the trenches vary according to the defined geometries. A lightly doped p-type silicon wafer (Silicon Quest International Inc.) was used as a substrate and SU-8 2005, 2010, 2030, 2050 (Microchem Corp.), SPR 220-7 (Megaposit), OIR 897-10I Positive I-line Photoresist (Fujifilm) was used as UV-sensitive photoresists. For the SU-8 patterns, SU-8 2005, 2010, 2030 and 2050 were spin coated onto a silicon substrate at 3000 rpm for 30 s to achieve the thickness of 5, 10, 30 and 50 μm and soft baked at 95 $^{\circ}\text{C}$ for 2, 3, 7 and 10 min respectively. After UV-light exposure, the sample was baked at 95 $^{\circ}\text{C}$ for 2, 3, 6 and 10 min for post-exposure bake and developed for 1, 2, 5 and 7 min. For the SPR 220-7 patterns, the photoresist was spin coated onto a silicon substrate at 2200 rpm for 30 s (thickness|10 μm) and soft baked at 115 $^{\circ}\text{C}$ for 5 min. After UV-light exposure, the sample was developed for 4 min. For the I-line patterns, the photoresist was spin coated on a silicon substrate at 2200 rpm, 5000 rpm for 30 s to achieve the thickness of 2, 1.2 μm respectively and soft baked at 90 $^{\circ}\text{C}$ for 1 min. After the lithography step, oxygen plasma treatment (50 W, 260 mTorr, 30 s) enhanced the hydrophilicity of the patterned surface and the substrate.

3.2.3. Design of Experiments for Scaling Analysis

The scaling effect of the patterning was studied by the experiments of four-different length-scales. Silica microspheres whose diameters are 0.5, 1, 3 and 5 μm were used for the patterning of the dots whose widths are 10, 20, 60 and 100 μm respectively. According to each size of the particle, four different concentrations (0.3125, 0.625, 1.25 and 2.5 wt%) of the suspension were used. The volume of the suspension used for the patterning was calculated in a way that the number of particles per unit area of the patterning is constant to $4 \times 10^{-9} \sim 4.2 \times 10^{-9}$ throughout the experiments of all the length-scales. That results in the patterning of

the same number of the patterns. The volumes of 0.125, 1, 8 and 27 μL were used in the patterning of 0.5, 1, 3 and 5 μm of the silica microspheres respectively.

3.2.4. Patterning of Micro, Nanoparticles

All the patterning experiments on the photopatterned substrate were conducted in air environment at atmospheric pressure and room temperature conditions. Micro syringe (Microliter Syringes 5 μL , Hamilton) was used to extract a small volume (0.125 ~ 2.0 μL) of the micro, nanoparticle solution and a single droplet was placed on the photopatterned substrate. After the particle assembly was completed, the sample was placed at room temperature for 1 h to evaporate the solvent completely and the photoresist was dissolved by either acetone or PRS 3000 Baker (J.T. Baker).

3.2.5. Imaging

The samples were imaged by optical microscope (Polylite 88, Reichert-Jung) and scanning electron microscopy (LEO 1550, ZEISS). A cross section of the channel was imaged after the sample was coated via the sputtering of a Au / Pd thin film.

3.3. Principles of Confinement of 3D Micro, Nanoparticle Assemblies in Micro-Scale Templates

This technique is mainly grounded on the coffee-ring effect of solutes in an evaporating suspension. When a spilled drop of coffee dries on a solid surface, it leaves a dense, ring-like deposit along the perimeter. Such ring deposits are common wherever drops containing dispersed solids evaporate on a surface[130]. While a number of theoretical descriptions have been reported to estimate the growth-rate of ring deposit[130], velocity fields of a drying droplet[131, 134, 135] and the dynamics of particle deposition[129], applying the coffee-ring effect to pattern particle assembly has not been realized in current micro fabrication

technology. It is demonstrated that photopatterns with proper surface treatment can be used as an effective template to structure particle assembly.

3.3.1. Preparation of Photopatterned Substrate

At first, conventional photoresist such as I-line (OIR 897-10I, Fujifilm) or SPR 220-7 (Megaposit) was spin coated onto a substrate and patterned by UV exposure with followed development and oxygen RF plasma was applied on the patterns. In case the medium of the particle suspension was hydrophilic as water is, a droplet of the suspension was placed on the pattern immediately after the surface treatment. Details on the preparation of photopatterned substrate are described in Experimental section. The oxygen plasma was used to make the surface hydrophilic and eliminate probable residue of the photoresist.

3.3.2. Description of Sequential Processes of Self-Assembly of Particles

Figure 3.1 illustrated the sequential processes of the evaporative self-assembly of particles on photopatterned substrate. At first, a droplet of liquid suspension where micro or nanoparticles are well dispersed was placed on the photopatterned substrate. After then, the evaporation of the medium began to occur and the particles were driven to the peripheral area of the droplet. This action of the particles, the coffee-ring effect, was mainly driven by the hydrodynamics of a drying droplet. It is reported[134] that the contact line of droplet is pinned and the contact angle decreases for the most of drying time (98% of entire drying time). In this stage of the evaporation, the medium should flow from the center to the peripheral area to compensate for the loss of water, thus, the particles are also driven from the center to the peripheral region, creating coffee-ring deposit. When the contact angle reached the critical contact angle around $2\sim 4^\circ$, the contact line starts receding and the evaporation of the droplet is completed[134].

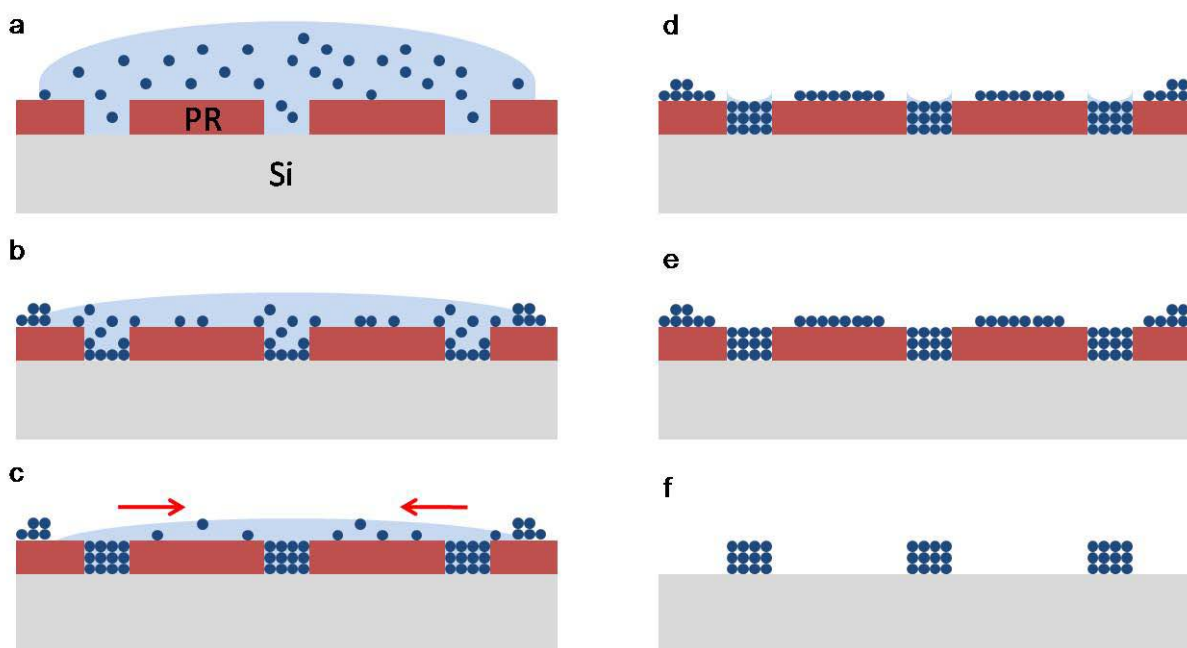


Figure 3.1 Schematics of the self-assembly of the micro particles on a photo-patterned substrate. (a) A droplet of the suspension is placed on the patterned substrate. (b) The evaporation of the solvent is initiated. After contact-line pinning, the particle starts being confined. (c) After critical angle, the droplet starts receding. Confinement of the particles is completed. (d) Global-evaporation is completed, the evaporation of local solvent forms tight assemblies of the particles. (e) The evaporation of the local fluid is completed. Tightly packed particle assemblies are formed. (f) The photoresist is removed. The patterns of particle assemblies are formed.

The snapshots of the evaporating droplet were taken prior to the completion of the evaporation as shown in Figure 3.2. These snapshots showed that the time consumed in de-pinning of the evaporating droplet was 3 s which was only 1.9 % of the overall drying time. A single, thick coffee-ring deposit at the edge of the droplet was observed from the snapshots. It may be seemingly contradictory to the observation of multiple concentric rings after the evaporation of a single droplet in Adachi's work[128]. In Adachi's work, the volume fraction of the suspension was around 0.4 ~ 0.8 % which was much lower than the ones in this work and the particle size was around 100 nm and monolayer of the particles is deposited at the edge of the droplet.

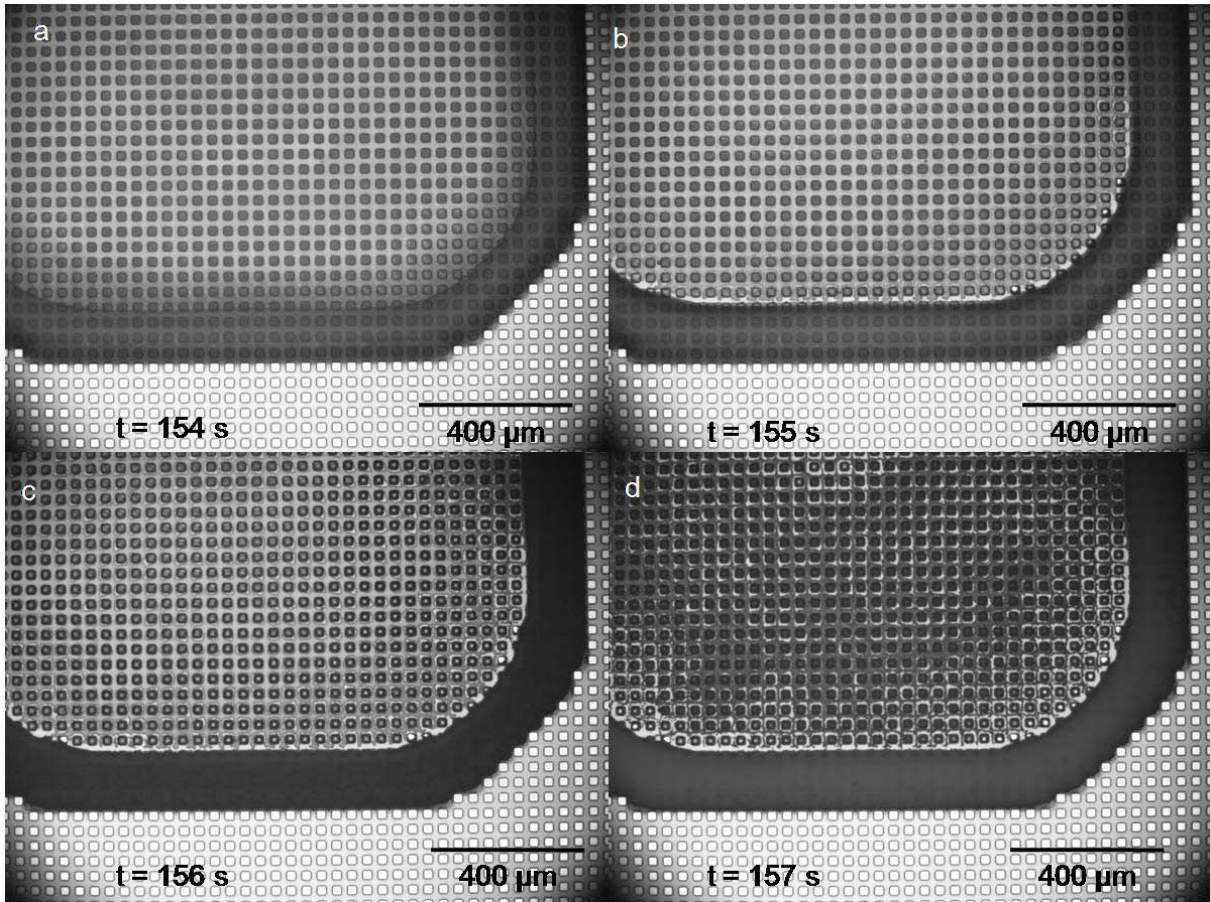


Figure 3.2 The snapshots of the particle assemblies before the completion of the evaporation. (a) 3 s before the completion, the solutes were being transported to the peripheral region. (b) 2 s before the completion, de-pinning of the contact line was initiated. (c) 1 s before the completion, the evaporation of the local fluid was initiated. (d) The evaporation was completed. A thick, single coffee-ring deposit was generated at the edge of the droplet.

With the suspension of low concentrated suspension, the contact angle of the droplet was constantly maintained and de-pinning and deposition of coffee-ring deposit were periodically repeated to form multiple concentric rings of the deposit. However, if the fraction of the suspension reached to around 0.3 ~ 2.5 wt% with larger particles as used in this work, the coffee-ring deposits consisted of multiple layers of particle assembly and prevented de-pinning of the contact line of an evaporating droplet. In this experimental platform, the over-pressure gradient generated by the curvatures of the patterns[140] also locally drove the particles to the trenches formed by the patterns while the particles were transported to the edge of the droplet globally.

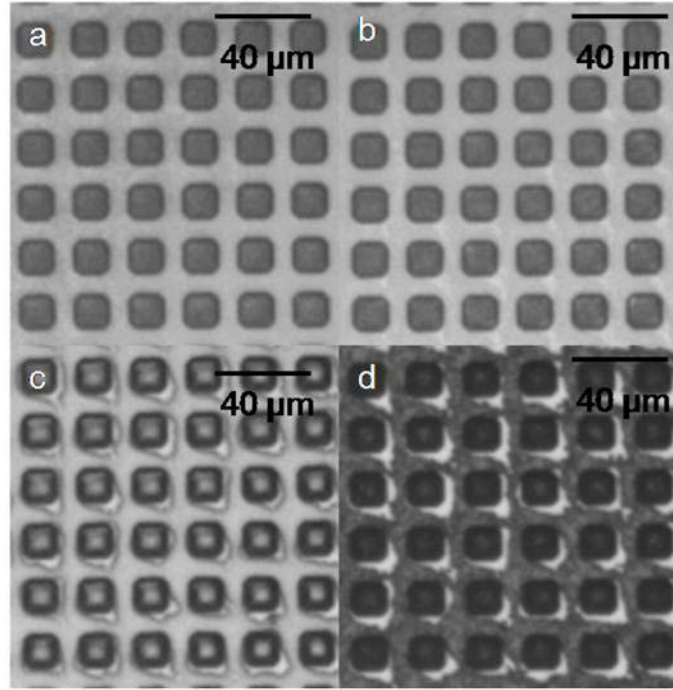


Figure 3.3 The magnified views of images from Figure 3.2 at the center of the droplet. (a) 3 s before the completion, the solutes were confined to the well (b) 2 s before the completion, slight evaporation of the medium was observed. (c) 1 s before the completion, the evaporation of the local fluid was initiated, the separation of the fluid inside the well and outside the well was observed. (d) The evaporation was completed. The particle assemblies inside the trenches and outside the trenches were clearly separated.

As can be seen from Figure 3.3, the particles inside the trenches and the particles on the photoresist were clearly separated throughout the entire droplet so that the lift-off process would not perturb the particle assembly inside the trenches. The separation of the particles inside the trenches and the particles on the photoresist occurred because of the meniscus effect of the evaporating medium in the trenches[60, 111, 112, 126] and it lasted until either the concentration or the volume of the suspension stayed optimal ranges for the process. Additional images to show the relationship between the volume of suspension and the nature of the particle deposition are available in Appendix A.1. Also, the clear separation of the particles inside the trenches from the ones on the resist was also shown in Appendix A.1. In order to verify theoretically that this phenomenon is general regardless of different parameters of the processes, the scaling analysis of the pressure and time scale of global and local fluid behaviors in the evaporating

droplet were performed in section 3.5. Also, the scaling effect of the patterning, the effect of the volume and the concentration of the suspension and the effect of surface treatment were studied in chapter 3.5.

3.4. Release of Particle Assemblies from Templates

After the particles were confined inside the trenches, the photoresist was dissolved by remover (either Acetone, or PRS 3000 (J. T. Baker)) and microspheres-based 3 D structures were released as shown in Figure 3.4, 3.5. It is noteworthy that the packing structure was preserved without any perturbation during the removal process of the photoresist. The assembled structure was preserved when the diameter of silica microspheres was 3 μm or less (the images of 3 μm silica microspheres-based structures are attached in Appendix A.2.). However, the structure was perturbed when the diameter was 5 μm or larger. The size of particle decreased, the surface- to-volume ratio increased, thus, a stronger Van der Waals force preserved the particle assembly intact. Also, the surface charge condition of the particles is another crucial factor in the stability of the structures. The microstructure based on polystyrene microspheres (diameter|1 μm) was deteriorated after the photoresist removal. From these observations, one can conclude that the interparticle force of the assembled structure is dependent on the surface charge properties of the particles as well. Negatively charged colloidal particles, such as polystyrene, cannot withstand the photoresist removal process since the interparticle electrostatic repulsion force was stronger than the attractive force in nonpolar solvents[115]. It is anticipated that the smaller, insulating or semiconducting particles, will be more advantageous in line patterning than the larger and metallic particles. Uniform patterning of silica microsphere based, high-aspect ratio structure was achieved inside the coffee-ring region as shown in Figure 3.4. Interesting feature is that the particles of the coffee-ring region where the excessive particles were connected to the particles inside the trenches form bridge structure without collapse after the removal of the photoresist. This indicates that the attractive force between the particles outdid the gravity force. This suspended

structure can be potentially used for various MEMS (microelectromechanical systems) applications such as microfilters or cell sorting devices.

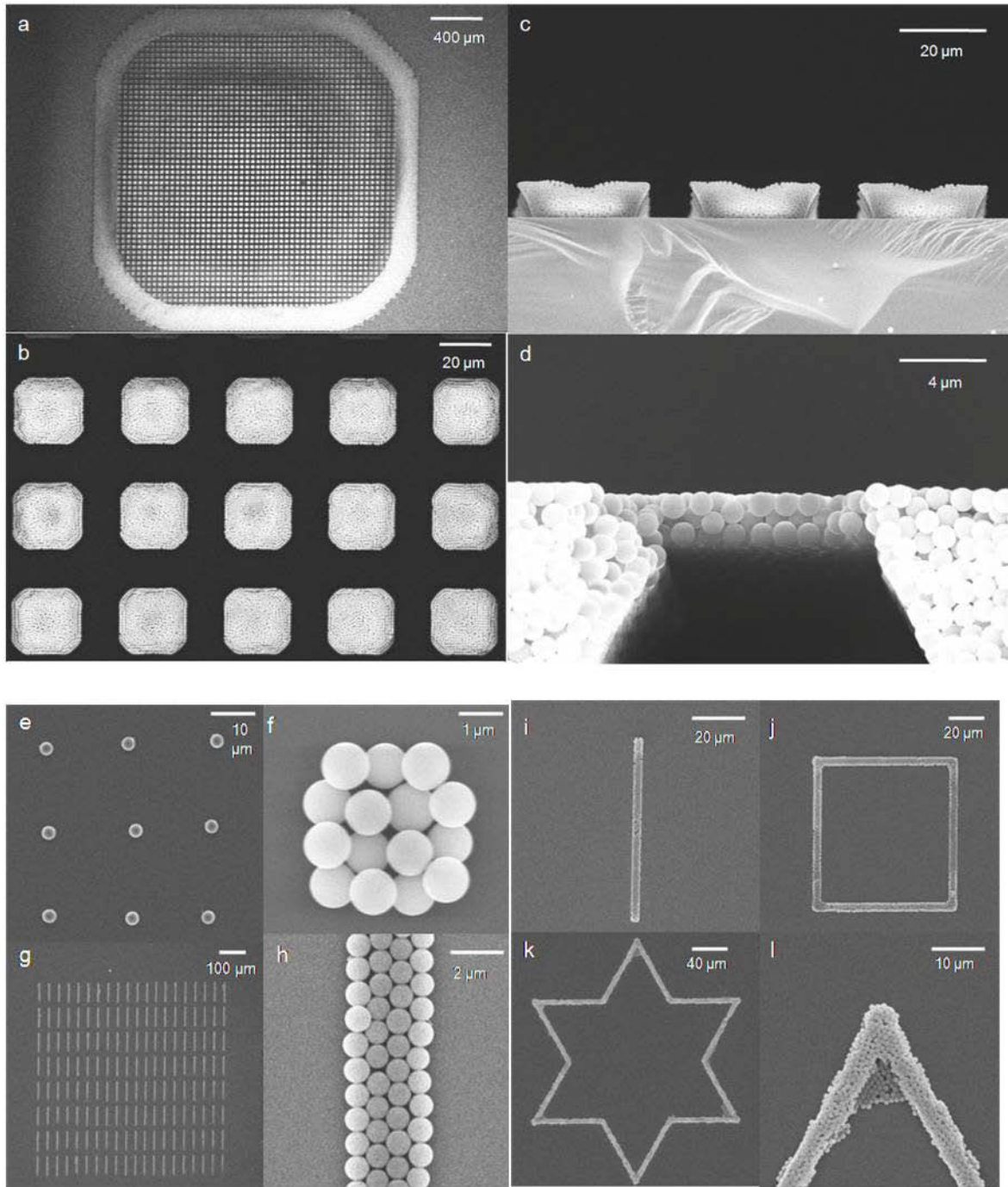


Figure 3.4 The images of the patterns of the microparticle assembly (after lift-off) (a) An overall top view of the patterns. (b) A close top view of the patterns. (c) A cross sectional view of the patterns. (d) A bridge-structure formed in the coffee-ring region. (e) The patterns of single particles (diameter, 3 μm). (f) A pattern of mono-layer particle assembly (diameter, 1 μm). (g) The line patterns of particle assembly (diameter, 1 μm). (h) A close view of a single line. (i) An

overall view of single lines. (j) An overall view of a rectangle. (k) An overall view of a star. (l) A close view of a star.

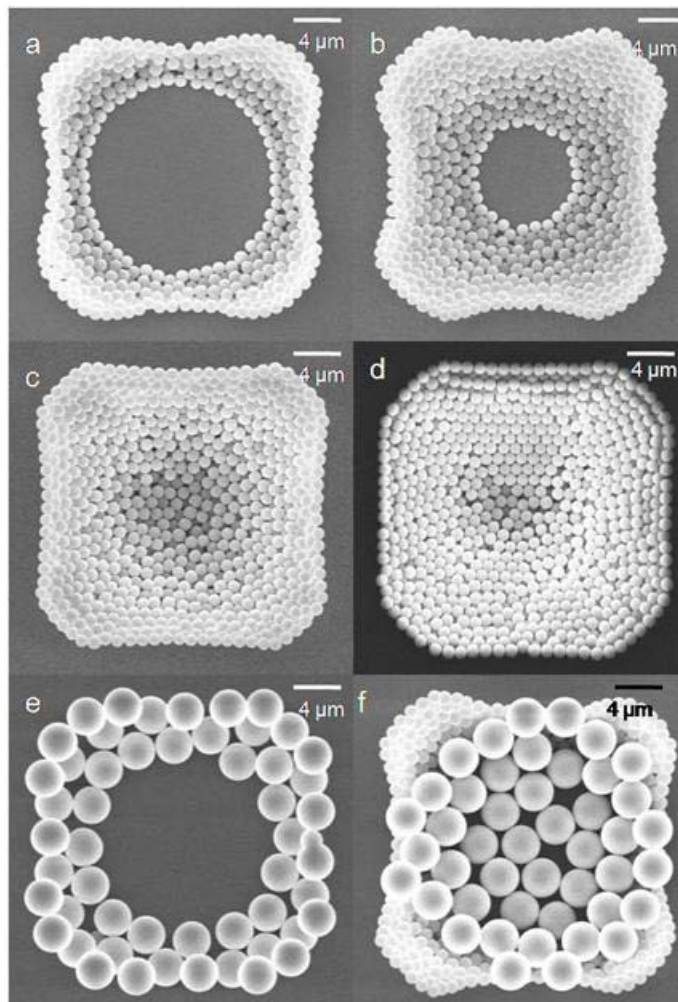


Figure 3.5 The dependence of the patterning with the concentration of the suspension. (a) 0.3125 wt% of the suspension (silica microspheres, diameter, 1 μm , 2 μL). (b) 0.625 wt% of the suspension (silica microspheres, diameter, 1 μm , 2 μL). (c) 1.25 wt% of the suspension (silica microspheres, diameter, 1 μm , 2 μL). (d) 2.5 wt% of the suspension (silica microspheres, diameter, 1 μm , 2 μL). (e) 0.3125 wt% of the suspension (silica microspheres, diameter, 3 μm , 2 μL). (f) A hybrid structure made by two 0.3125 wt% of the suspension of the different microspheres (silica microspheres, diameter, 3 μm (first), 5 μm (second), 2 μL).

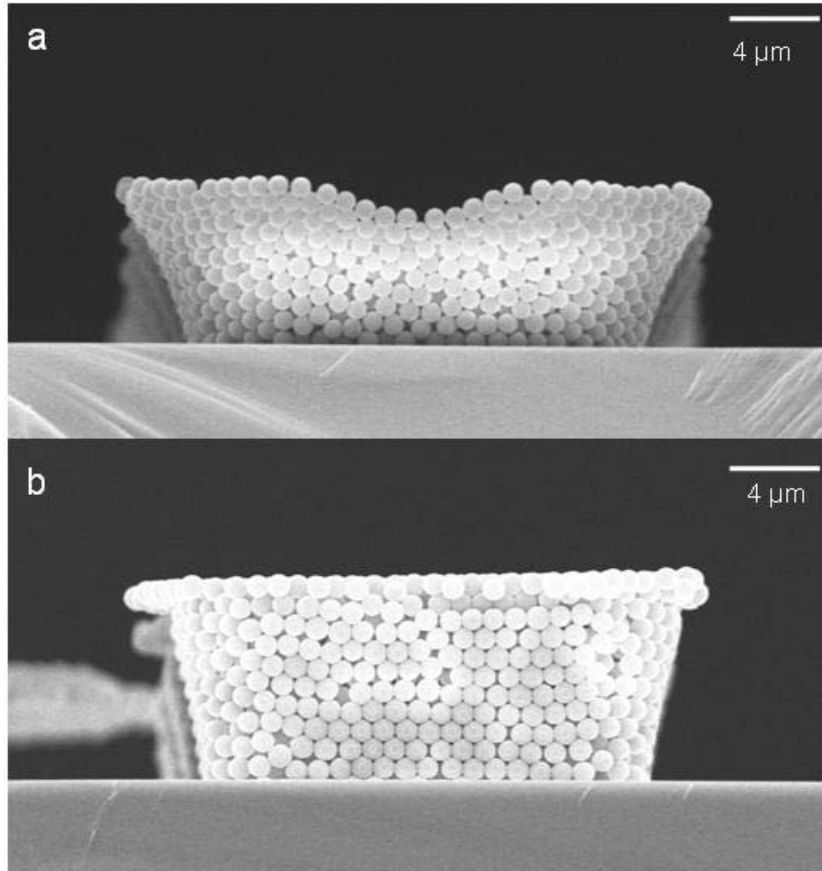


Figure 3.6 (a) A cross sectional view of the pattern made from 2.5 wt% of the suspension (silica microspheres, diameter, 1 μm , 2 μL). (b) A cross sectional view of the pattern made from 5 wt% of the suspension (silica microspheres, diameter, 1 μm , 2 μL).

Also, various structures are fabricated by adjusting the concentration of the suspension. Designing arbitrary geometries on photomask for photolithography with setting proper photoresist thickness, 3D patterns can be defined and this pattern can serve as an effective template to structure the particle assemblies. The trenches comparable to the size of the single particles, lines, rectangle, star-shaped were fabricated and used for the templates to pattern the particle assemblies. In this patterning, the patterning area was designed smaller than the contact-line area of the droplet so that the bridge structure at the coffee-ring region was not formed. At the lift-off step, the particles which are located at the corner whose angle is smaller than 90° were harder to be resolved because the excessive particles were driven by higher “over-pressure” gradient and attached to the particles inside the trenches. However, simple, symmetric patterns such as dots and lines were resolved well. If

the spacing of the patterns was too small, or if the ratio of the particle diameter to the length of the pattern was too low, the patterns are not resolved well. It was found that the presented technique may not offer as small resolution as the reported previous technique[53], however, it still holds the advantages in terms of 3D structuring of the assembly and superb simplicity. The commensurable effect was observed in the line and dot patterns. The number of the particles across the width ($=N_1$) is equal to $f\left[\frac{W(\text{Width})}{D(\text{Particle Diameter})}\right]$ where function $f[x]$ returns the largest integer less than or equal to x . This effect is verified down to the limit of conventional contact-photolithography ($\sim 4 \mu\text{m}$). The single particles (diameter, $3 \mu\text{m}$), dots and lines where the number of the particle (diameter, $1 \mu\text{m}$) across the width is four were patterned. With the proper choice of the dimensions of the template, desirable structures of the particle assembly was fabricated as demonstrated. As stated previously, the corner effect caused “over-pressure” gradient at the corner of the patterns hinged on the substrate. Therefore, the particles were transported to the corner first. In case of lower concentration suspension, fewer particles were transported to the corner until the evaporation of the droplet was completed, thus, ring-shape structures were generated. As the concentration increased, the particles were deposited from the corner to the top of the pattern symmetrically as shown in Figure 3.5. By simple multi-step process, hybrid ring structures of the different size-particles were fabricated too. This showed that the multi layer patterns can be easily formed by placing multiple different droplets in the same location in serial.

3.5. Theoretical Analysis of Patterning Results

As mentioned in the previous section, the scaling analysis of the pressure and time scale of global and local fluid behaviors in the evaporating droplet were attempted in order to verify the validity of the process. Figure 3.6 shows an axisymmetric droplet on a horizontal substrate with the fluid density ρ^* , viscosity μ^* , initial height h_0^* and initial radius r_0^* . Asterisk * denotes the dimensional parameters and the other denotes non-dimensional parameters. The scales of global pressure P_1^* and global time t_1^* can be obtained from Fischer’s model[131].

3.5.1. Scaling Analysis of Main Parameters in Hydrodynamics of Process

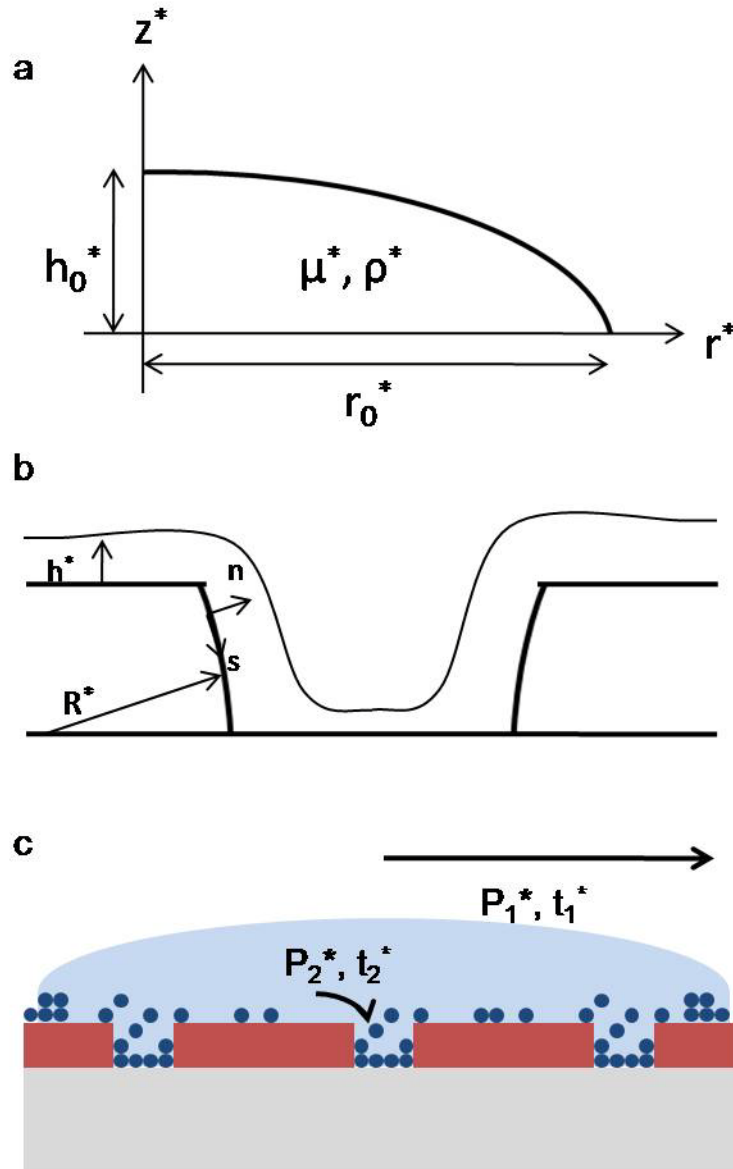


Figure 3.7 Notations for the scaling analysis. (a) Global coordinates with respect to the droplet. (b) Local coordinates with respect to a single pattern. (c) A schematic of the definition of global, local pressure and time.

The governing equations for the global fluid flow are

$$0 = \frac{1}{r} \frac{\partial}{\partial r} (ru) + \frac{\partial w}{\partial z} \quad (3.1)$$

$$0 = -\frac{\partial p}{\partial r} + \frac{\partial^2 u}{\partial z^2} \quad (3.2)$$

$$0 = -\frac{\partial p}{\partial z} \quad (3.3)$$

where radial velocity u^* is scaled by the characteristic viscous velocity, $u_c^* = \frac{\mu^*}{\rho^* h_0^*}$, pressure p^* is scaled by the characteristic pressure, $p_c^* = \frac{\mu^* u_c^* r_0^*}{h_0^{*2}}$, vertical velocity, w^* is scaled by $\epsilon u_c^* = \frac{\mu^*}{\rho^* h_0^*}$ and $\epsilon = \frac{h_0^*}{r_0^*}$ is the ratio of the initial height to the initial radius of the droplet. Also, radius (r) and height (z) are non-dimensionalized by the initial radius of the droplet, r_0^* , the initial height of the droplet, h_0^* . The global, dimensionless radial velocity, u , to drive the particles from the center to the peripheral area can be expressed as

$$u = -\frac{1}{Ca} \frac{\partial}{\partial r} \left[\frac{1}{r} \frac{\partial}{\partial r} \left(r \frac{\partial h}{\partial r} \right) \right] \left(\frac{1}{2} z^2 - hz \right) \quad (3.4)$$

where $Ca = \frac{\mu^* u_c^*}{\epsilon^3 \sigma^*} = \frac{\mu^{*2}}{\epsilon^3 \rho^* \sigma^* h_0^*}$ is the capillary number, μ^* is the viscosity of the medium, and σ^* is the surface tension of the liquid. The height (h^*) of the droplet is non-dimensionalized by the initial height of the droplet, h_0^* .

Also, full height evolution profile can be expressed as[131]

$$\frac{\partial h}{\partial t} = -\frac{1}{3Ca} \frac{1}{r} \frac{\partial}{\partial r} \left[r h^3 \frac{\partial}{\partial r} \left(\frac{\partial^2 h}{\partial r^2} + \frac{1}{r} \frac{\partial h}{\partial r} \right) \right] - EJ \quad (3.5)$$

where $E = \frac{k^* \Delta T^*}{\epsilon \mu^* L^*}$ is the evaporation number and J is a spatially and time-dependent mass-flux which is scaled by the characteristic mass flux $J_c^* = \frac{k^* \Delta T^*}{h_0^* L^*}$. On this scale, k^* is the thermal conductivity of the liquid, L^* is the heat of vaporization and ΔT is the temperature difference between the temperature on the substrate and the saturation temperature. Time t was non-dimensionalized by $t_c^* = \frac{r_0^*}{u_c^*}$. From the relations above, u can be scaled as $\frac{1}{Ca}$ thus, the global pressure P_1^* can be scaled as $\frac{1}{Ca} \frac{\mu^* u_c^* r_0^*}{h_0^{*2}} = \frac{p_c^*}{Ca}$ from equation (3.2). Also, the global time t_1^*

can be scaled as the larger one of either Cat_c^* or $\frac{t_c^*}{E}$. The scale of the local pressure P_2^* and the local time t_2^* can be obtained from Schwartz's model[131] of coating flows on curved surface since the medium can be regarded as a thin coating layer on the curved substrate in the thin droplet. In Figure 3.6, (s, n) are local orthogonal coordinates with s being arc-length along the surface and $n = h(s, t)$ is the layer thickness to be determined. R^* is the mean curvature of the patterns. The expression for the pressure inside the coating flow is composed of two parts: 'overpressure' distribution by the curvature of the patterned substrate ($\frac{\sigma^*}{R^*}$) and hydrodynamic effects by the fluid height ($\sigma^* \frac{\partial^2 h^*}{\partial s^2}$).

$$p^* = -\frac{\sigma^*}{R^*} - \sigma^* \frac{\partial^2 h^*}{\partial s^2} \quad (3.6)$$

The height-evolution profile in dimensionless forms can be expressed

$$\frac{\partial h}{\partial t} = -\frac{\partial}{\partial s} [h^3 (\frac{\partial^3 h}{\partial s^3} + M\delta(s))] \quad (3.7)$$

where $\delta(s)$ is the Dirac delta function. In our geometries, M can be expressed as $\frac{\pi w^*}{4 h_0^*}$ where w^* is the width of the pattern. Time t and height $h(s, n)$ was non-dimensionalized by the larger one of either $T^* = \frac{3\mu^* w^{*4}}{\sigma^* h_0^{*3}}$ or h_0^* . Therefore, the local pressure P_2^* can be scaled as either $\frac{\sigma^*}{R^*}$ or $\sigma^* h_0^*$ and the local time t_2^* can be scaled as the larger one of either T^* or $\frac{T^*}{M}$. In order for the particles to be confined in the trenches before the evaporation of the droplet is completed, two conditions are required: the local pressure has to be greater than the global pressure ($P_1^* \ll P_2^*$) around the patterns and the time for the particles to be transported from the droplet to the trenches has to be shorter than the time for the droplet to be evaporated. ($t_1^* \gg t_2^*$) If the experimental parameters of the processes are input (see the details of calculation in Appendix A.3.), the scale of P_2^* is $\frac{\sigma^*}{R^*}$, the scale of t_1^* is $\frac{t_c^*}{E}$ and the scale of t_2^* is T^* . Therefore, $\frac{P_2^*}{P_1^*} \approx \frac{r_0^{*2}}{w^* h_0^*} \gg 1$ and $\frac{t_2^*}{t_1^*} \approx \frac{3k^* \Delta T^* u_c^* w^4}{\sigma h_0^{*4} L^*} \ll 1$.

This analysis indicates that the negative curvature of the radius of the patterns can serve as particle sinks while the convective transport of the medium drives the excessive particles to the edge of the droplet. It has an analogy with iron filings on paper where series of magnets backing the paper withhold filings and wind blow eliminates extra filings where the magnetic force cannot reach. It is important to note that diffusion is not a major governing factor in the process. This can be easily verified by the comparison of the time scale of the diffusion process with the time scale of the convective transport which has been already calculated previously. The time scale of diffusion, t_3 can be expressed as $\frac{x^2}{D}$ where x is the travel distance of micro, nanoparticle and D is a diffusion coefficient of particles in liquid. After the parameters of the processes are input to the calculation (see the details of calculation in Appendix A.3.), it is $\frac{t_2^*}{t_3^*} \approx \ll 1$ which means the process is completed much before diffusion plays a major role in the process, thus, diffusion can be neglected. The deposition of particles is mainly concentrated inside the trenches more than on the resist because of over-pressure gradient. If diffusion is dominant, the deposition of particles would be uniform throughout the entire droplet area, thus, the separation of the particles between the trenches and the resist cannot be achieved. Therefore, the separation of the particles can be attributed to the nature of the convective transport of the particles during the process.

3.5.2. Studies of Scaling Effect, Effect of Volume and Concentration of Suspension on Patterning

After the particles are confined in the trenches, it is important for the particle assemblies in the trenches to be separated from the particles on the photoresist since the particle assemblies inside the trenches should not be perturbed by the particles on the photoresist during lift-off processes. Therefore, it is important to adjust process parameters such as the length-scale of the trenches, the volume, the concentration of the suspension and the surface charge condition in order to fill the trenches completely without being connected to the particles on the photoresist. At first, the scaling effect of the patterning was studied by the experiments of four-different length-scales. The details of the experiments were described in chapter

3.2.1. The volume of the suspension used for the patterning was determined in a way that the number of particles per unit area of the patterning was constant throughout the experiments of different length-scales. The analysis showed that there is an optimal range of the length scale of trenches and the particles for effective patterning by using presented technique.

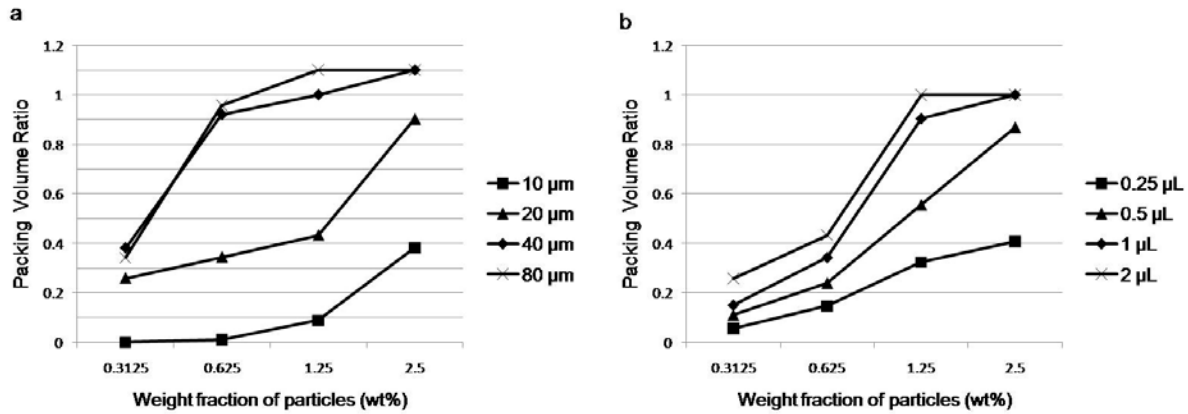


Figure 3.8 The graphs of the packing volume ratio versus the weight fraction of a suspension. (a) The graph of scaling effect. The packing volume ratio, 1 refers to the complete filling of the trenches without interconnection between particles inside the trenches and outside the trenches. The packing volume ratio over 1 refers that the particle assemblies inside the trenches to the particles on the photoresist are connected. (b) The graph of volume effect.

As shown in Figure 3.8, the packing volume ratio (defined as (the volume of occupied particles) / (the volume of particles at complete filling of the trenches), the details of the calculations were described in Appendix A.5.) increased at given weight fraction of the particles as the length-scale increased. This implies that smaller weight fraction of the particles was required to achieve the complete filling of the trenches in case of larger length-scales. The previous scaling analysis showed that $\frac{P_2^*}{P_1^*} \approx \frac{r_0^{*2}}{w^*h_0^*}$ remained constant regardless of the length-scales, however, $\frac{t_2^*}{t_1^*} \approx \frac{3k^*\Delta T^*u_c^*w^4}{\sigma h_0^{*4}L^*}$ is proportional to $\Delta T^*u_c^* \propto \frac{\Delta T^*}{h_0^*}$. Assuming the change of ΔT^* is negligible in different length-scales, $\frac{t_2^*}{t_1^*}$ decreased as the length-scale increased. Therefore, the required time for the global transportation of the particles from the center of the droplet to the edge of the droplet became relatively larger in

the larger length-scale and more particles were inclined to be confined to the trenches than being transported to the edge of the droplet. This analysis indicated that the patterning of smaller particles in smaller length-scale trenches require highly concentrated suspension which is harder to be made in nanoparticle-synthesis. Furthermore, the size of the droplet required for the uniform patterning is inversely proportional to (Length scale of the pattern)³ and the size of the droplet has to shrink down significantly in smaller scale patterning, however, generating ultra small droplet is also a challenge. Although the patterning of larger particles in larger length-scale patterns required smaller weight fraction of the suspension, the patterning in large scale require long process time because the time for the droplet to evaporate correlates approximately with (Length-scale)² (see Appendix A.5. for a verification of this claim.). Also, extremely low concentration of the suspension which was needed in very large scale patterning also undermines effective patterning because the deposition of the particle assemblies was non-uniform and stripe-patterns of the particle assembly were formed over the entire area of the droplet[129]. Therefore, right dimensions of the trenches and the particles have to be chosen, considering the trade-off between the concentration of the suspension and process time. The dependence of the packing volume ratio on different volume of the suspension was studied at the fixed length-scale of the trenches. The higher concentration and the larger volume of the suspension increased the packing volume ratio. As can be seen from Figure 3.7, there exist optimal ranges of the volume, the concentration of the suspension for complete filling of the particles in the trenches without overflow in the given length scale of the trenches.

3.5.3. Studies of Surface Charge Condition of Templates on Patterning

Surface charge condition is another crucial parameter to achieve uniform, well-defined patterning of particle assembly. If the surface of the photopatterned substrate was not treated by oxygen plasma, the contact angle of the droplet of the suspension with respect to the substrate increased and Marangoni flow caused the non-uniform deposition of the particles. Marangoni flow is generated by the thermal gradient induced by the different evaporative rate inside the droplet and the direction of this flow is from the edge of the droplet to the center[134, 135]. Marangoni number, the indicator of Marangoni flow, is the ratio of the Marangoni

force to viscous force and represented as $Ma \equiv \frac{-\beta\Delta T_0 t_f}{\mu R}$ where $\beta = \frac{d\sigma}{dT}$, ΔT_0 is the temperature difference between the edge and the top of the droplet, t_f is drying time, R is the radius of contact line radius. If the contact angle increased, R decreased at the fixed volume of the suspension and t_f increased because the surface-to-volume decreased. Also, ΔT_0 increased because the vertical distance between the top of the droplet and the edge of the droplet increased and higher temperature gradient was required to transfer the same amount of the heat. Therefore, Ma increases and Marangoni flow reverses the coffee-ring effect. As shown in Figure 3.9, when the patterning was achieved without the treatment of oxygen plasma, the Marangoni effect caused the particles to be transported from the edge of the droplet to the center and more particles were deposited in the center than the edge of the droplet. It is noteworthy that the complete packing of the particles without any particle on the photoresist was observed in the peripheral area of the droplet. Without the treatment of oxygen plasma, the photoresist remained hydrophobic while the substrate was still hydrophilic. The particles in water medium were driven by the corner effect of the trenches as well as the surface-tension gradient created by the different surface energies between the photoresist and the substrates. The excessive particles after complete packing of the particles in the trenches were mainly driven by Marangoni flow without being left on the surface of the photoresist because the hydrophobic surface of the photoresist drove the particles to the Marangoni flow. This interesting, physical phenomenon may not be suitable in large area-patterning of particle assemblies because of the non-uniformity caused by Marangoni effect. However, it can be used effectively for local patterning of micro and nanoparticle assemblies on the micro-and nano-scales as long as the particle concentration is low.

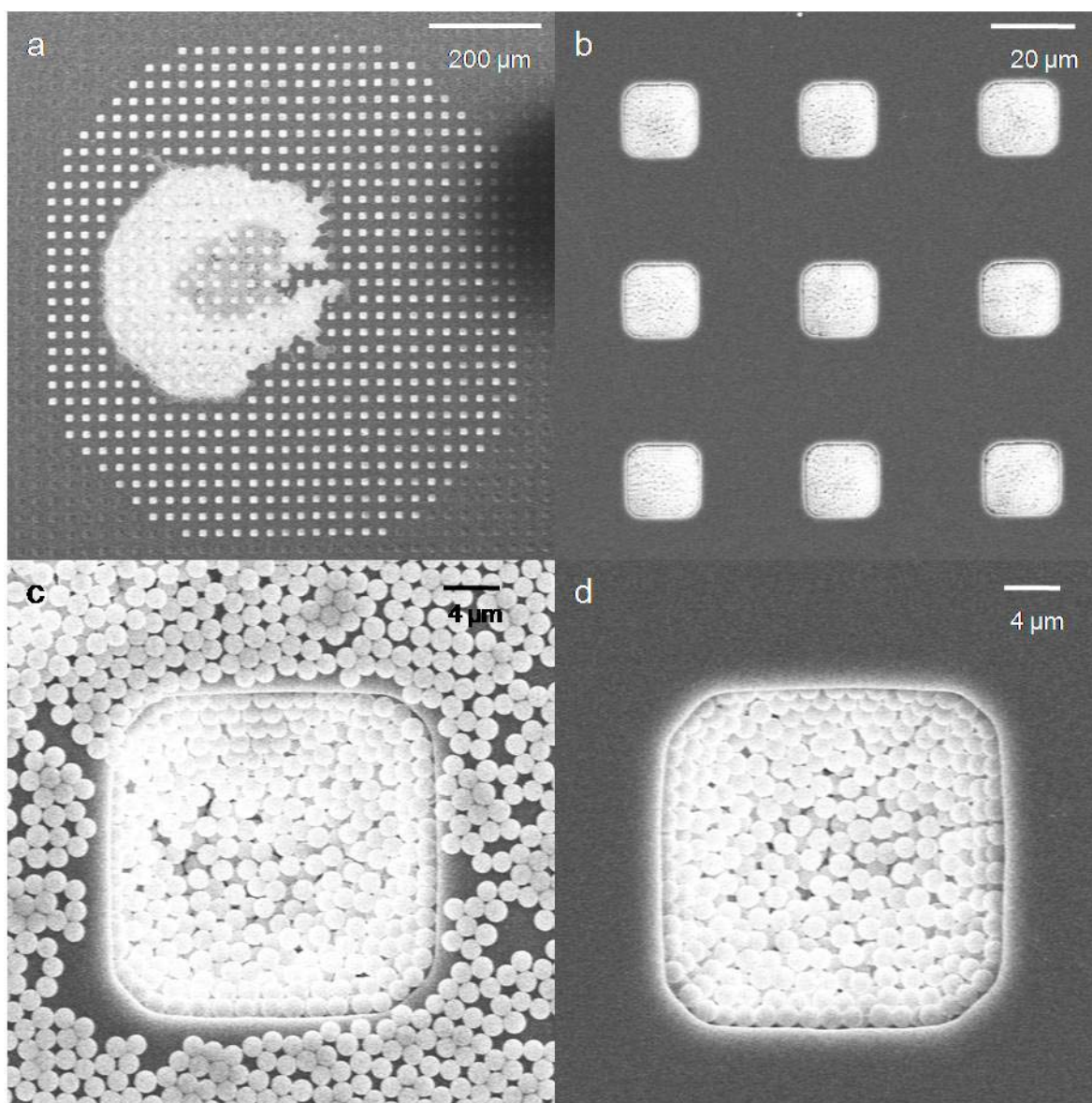


Figure 3.9 The images of the confinement of the particle assembly on a photopatterned substrate without surface treatment (before lift-off) (a) An overall view of the patterns. (b) The patterns in the peripheral area of the droplet. (c) A pattern in the centric area of the droplet. (d) A pattern in the peripheral area of the droplet.

Chapter 4. Printed Micro, Nanoparticle Assembly by Micro Scale Evaporative Flow

4.1. Introduction

In cutting-edge material science, significant efforts are made to manipulate, locate, and assemble micro, nanoparticles in targeted areas for numerous applications such as three-dimensional photonic crystals[61-63], circuitry of printed electronics on flexible substrates[64, 65], conductometric[116-118], and plasmonic-based biochemical sensors[66, 67]. Conventional approaches to create micro, nanoparticle assemblies - inkjet printing[51], electrohydrodynamic jet printing[57], dip-pen lithography[58], light-actuated dynamic patterning[50], gravure printing[53], template assisted evaporative self-assembly[48, 49, 143] or atomic force microscopy (AFM) tip-based contact printing[54, 55, 59] – have achieved a number of milestones in certain applications, however, these methods still suffer from many obstacles such as: long process time (> several minutes)[50, 51, 53, 54, 57-59, 64, 121, 122, 126, 144-146], low throughput,[50, 51, 57, 58] complicated and costly set-up[51, 57, 58] difficult control of pattern size and resolution[48, 49, 51, 53, 55, 57, 58, 121, 143] and challenges in an accurate alignment with other features[48, 50, 51, 53-55, 57-59, 143]. Also, large volume consumption of highly concentrated micro, nanoparticle inks increases material processing cost because the cost is mainly determined by the amount of the original materials used for synthesis and patterning of the inks. Here, a fast, high-throughput way to create size-controllable micro, nanoparticle-crystallized clusters is developed via evaporative self-assembly in picoliter-scale droplets of particle suspension[147]. Mediated by gravity force and surface tension force of a contacting surface, the picoliter-scale droplets were generated on a hydrophobic surface from bulk particle suspension in a nano-fabricated printing head. Rapid evaporative self-assembly of the particles on the surface led to fast clustering of microparticles and nanoparticles and formed crystallized particle clusters. Clustering of the particles in picoliter-scale droplets was observed in real-time and studied based on the physics of evaporative-assembly. Arrays of various

nanoparticle (zinc oxide, gold nanoparticles) clusters and microparticle (silica, polystyrene microspheres) clusters of controlled sizes and spacing were generated on a flat, hydrophobic substrate via fast evaporative self-assembly. The size of the clusters was tunable from single microparticle-scale ($\sim 1 \mu\text{m}$) to several hundred micro meters. Material consumption for creating clusters was lower than other existing approaches because the volume of the dispensed droplets were picoliter-scale and whole fraction of the particles were completely clustered upon the completion of the evaporation of the droplets. With this method, multiplex printing of various particle clusters with accurate positioning and alignment was demonstrated. Size-uniformity of the created clusters was thoroughly analyzed by examining uniform, large arrays of gold nanoparticle clusters based on Surface Enhanced Raman Spectroscopy (SERS). The SERS measurements showed that size-tunable, large arrays of nanoparticle-crystallized clusters were created from one-step printing of the presented method.

4.2. Experimental Methods

4.2.1. Materials

A liquid suspension of silica microspheres (Silicon dioxide-based micro particles; diameter, 1, 3, and 5 μm ; water, 95 wt%; silica: 5 wt%, Sigma-Aldrich) and a liquid suspension of fluorescent microspheres (Fluoresbrite Carboxylate[®]; diameter, 0.5 μm ; excitation wavelength maxima: 360 nm, 441 nm, 529 nm, 641 nm; water, 97.5 wt%; polystyrene microspheres: 2.5 wt%, Polysciences, Inc.) was diluted into various concentrations of suspension (1.25, 0.625, and 0.3125 wt% solutes). Zinc oxide nanoparticles (diameter, 30 nm; water, 60 wt%; ZnO, 40 wt%; MK nano) were diluted into various concentrations of suspension (2.5, 1.25, 0.625, and 0.3125 wt% solutes) by adding a controlled volume of deionized water. A liquid suspension of gold nanoparticles (diameter, 100 nm; water, 99.995 wt%, Au, 5×10^{-3} wt%; Nanopartz) was diluted into various concentrations of

suspension (5×10^{-4} wt%, 5×10^{-5} wt%, Au nanoparticles) and also was concentrated by 10 times (5×10^{-2} wt %, Au nanoparticles).

4.2.2. Fabrication of Printing Heads

A Silicon-on-Insulator (SOI) wafer (Diameter 150 mm, Top device layer: silicon 100 nm, Buried oxide layer: silicon dioxide 400 nm, Base: silicon 650 μ m, *SOITEC*, France) was used for the fabrication of the printing head. The backside of the SOI wafer was grinded by 400 μ m to reach the final thickness of 250 μ m and polished. Low-stress silicon nitride film of 35 nm was deposited on both sides of the wafer by Low-Pressure Chemical Vapor Deposition (LPCVD) for generating masking materials of wet-etching process. Then, back-side of the wafer was spin-coated with photoresist and baked at 120 °C for 5 min and placed in Buffered-Oxide-Etcher (BOE, BHF: DI water = 10:1) for 10 hours to etch the silicon nitride layer of top-side of the wafer. After complete etching of the silicon nitride layer on the top-side, the photoresist was removed by photoresist removal (PRS-3000, *J.T. Baker*, USA) overnight. The wafer was diced into 1 cm \times 1 cm dies and both top and back sides of each die were coated with photoresist. Photolithography was performed on top-side to define holes for a porous membrane of the printing head and Reactive-Ion Etching (RIE) to etch top side silicon through the defined photopatterns was followed by taking advantage of buried oxide as an etch-stop layer. After the removal of the photoresist, the top and backsides of the chip were coated with photoresist and reservoir area of the bulk suspension was defined by photolithography followed by RIE etching to open area for silicon wet-etching. Before wet-etching of bulk silicon layer, top-layer was coated with 10 μ m-thickness protective polymer (ProTEK B3, *Brewer science*, USA) to protect porous membrane structures on top-side from being etched by wet-etchant. The prepared chips are wet-etched for 4 hours in the bath where 15 Liter of 5 % Tetramethylammonium hydroxide (TMAH) solution was prepared at 90 °C. After wet etching is completed, the protective polymer was removed by PRS-3000 / IPA / water rinse and BOE etching (5:1 BHF, 5 min at room temperature) was followed to etch a buried oxide layer completely. By design, thin, microporous membrane is released where the area of the membrane is 2 mm \times 2 mm. The membrane side of

the fabricated devices was treated by oxygen plasma (300 Watt, 250 mTorr, 1 min) to eliminate possible residue of protective polymer and the devices were placed on hot plate at 120 °C overnight to neutralize charge state of the membrane surface from hydrophilic state. Finally, the fabricated printing heads were coated with Fluorooctatrchlorosilane (FOTS) monolayer by Metal-Organic Chemical Vapour Deposition (MOCVD) to maintain the top side of membrane hydrophobic.

4.2.3. Fabrication of Handling Wafer

A 4 inch-silicon wafer (Lightly p-type doped, Thickness: silicon 500 μm) was used for the fabrication of the handling wafer. Low-stress silicon nitride film of 35 nm was deposited on both sides of the wafer by Low-Pressure Chemical Vapor Deposition (LPCVD) for generating masking materials of wet-etching process. Top side of the wafer was coated with photoresist. Photolithography was performed on top-side to define a wafer-through hole (6 mm \times 6 mm square) and Reactive-Ion Etching of silicon nitride layer through the defined photo-patterns was followed to define etching area. The wafer is wet-etched for 16 hours in the bath where 15 Liter of 5 % Tetramethylammonium hydroxide (TMAH) solution was prepared at 90 °C. After wet etching is completed, the protective polymer was removed by PRS-3000 / IPA / water rinse and the surface of the wafer was cleaned by oxygen plasma (300 Watt, 250 mTorr, 1 min) to eliminate the residue of the protective polymer.

4.2.4. Fabrication of Printing Head- Handling Wafer Complex

At first, a fabricated handling wafer was spincoated with photoresist. The printing head is placed on the center of handling wafer in a way that the membrane of the printing head is exposed to air without any blocking. Then, the printing head - the handling wafer with photoresist complex are baked together at 120 °C for 1 min on hot plate with heavy load press to promote the adhesion between the printing head and the handling wafer.

4.2.5. Micro-and Nano-particle Printing

A printing head – handling wafer complex was attached to a mask holder of uv-exposure system for contact- photolithography (MA/BA6, Suss MicroTec, Germany) via vacuum. The mask holder was inserted to the system and a substrate for printing was loaded to the stage. After loading the substrate, the alignment of the printing head to the patterns on the substrate wafer was performed and the spacing gap between the printing head and the substrate was controlled and placed by taking advantage of the embedded electronics of the system. The minimum threshold gap was a half of the width of pore size of the membrane. The micro, nanoparticle suspension was loaded to the reservoir of the printing head. Initially, 10 μ l volume of the suspension was loaded by micro-pipette to the reservoir forming a circular contact line of an overflowed droplet on top of the fluid-cell. Then, the meniscus of the suspension was flattened by drawing excessive volume of the suspension to ensure two-dimensional symmetry of the meniscus surface is not perturbed. A thin, glass cover-slide was capped on the mask holder to prevent the evaporation of the suspension during printing. The contact of the extruded membrane of the printing head was performed by driving the mask holder to the substrate. After 1 second of the contact, the printing head was driven back to the original position and the evaporation of the printed droplets were observed in-real time by optical microscope embedded in the printing system in case the concentration of the suspension was sufficiently low to be transparent. After the evaporation of the droplets was completed, the substrate with printed patterns was unloaded.

4.3. Generation of Picoliter-scale Droplets of Particle Suspension

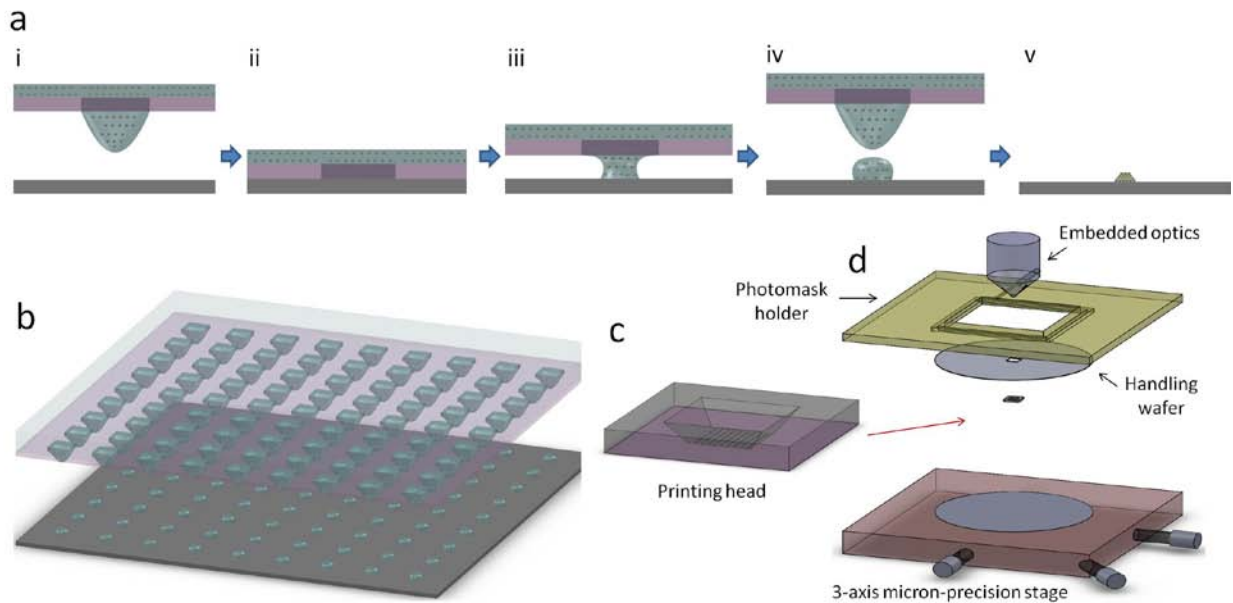


Figure 4.1 Schematics of printing procedure a. Serial processes. (i) Particle suspension menisci are extruded to the upfront end of the membrane by gravity. (ii) Contact of the head with the substrate is achieved. (iii) Surface tension of the substrate attracts a fraction of the suspension fluid. (iv) Picoliter- scale droplets are transferred to the substrate via pinch-off processes. (v) Rapid evaporative self-assembly of the particles forms 3-D clusters. b,c. A high-throughput printing head. d. A global printing system. A printing head is attached to conventional photolithography tool. 3-axis micron-precision stage and embedded optics performs accurate positioning and alignment of clusters.

Figure 4.1 illustrated the general procedure of printing micro, nanoparticle clusters. The printing head was fabricated by applying conventional micro-fabrication technology to SOI (Silicon-On-Insulator) substrates. Holes of the printing head were defined by photolithography and reactive-ion-etching was followed. Backside was wet-etched in order to define a reservoir region to contain micro, nanoparticle suspension. After the final etching step, a microporous membrane with two hundred nanometer thickness was released on the head. It was mechanically robust and did not break by fluid rinsing steps. After the fabrication of a die-size, printing head, the head was attached to a handling wafer and this handling wafer-printing head complex was directly attached to the mask holder of

conventional UV-exposure system for photolithography. Micron-precision, three-axis stage controller of the system allocated the printing head to the targeted area aided by the optics in the system. The suspension was loaded by micropipette to the head within a few seconds and the printing head with loaded suspension was covered with a transparent glass cover slip in order to prevent premature drying during the printing processes. Since the patterning of the droplet is not greatly sensitive to the loaded volume of the suspension to the head, the inherent error caused by micropipetting was not considered to be significant. After loading the suspension to the head (0.1 μL – 10 μL), meniscus of the droplet was fully extruded to the front end of the head within a second. Direct contact of the head with the substrate was performed to transfer multiple picoliter (2 pL – 20 pL)-scale droplets of particle suspension from the bulk suspension to the substrate through porous membranes of the head. This whole printing process takes less than 5 seconds. As illustrated in Figure 4.1, the printing process of the picoliter-scale droplets is divided into two main steps; a) Extrusion of the meniscus of the fluid and b) Transfer of the droplets to the substrate. The extrusion of fluid meniscus is driven by gravity force. If gravity force drives the fluid by overcoming pressure drop across the membrane, the meniscus is extruded. When the membrane thickness was 10 μm , pressure drop across the membrane with 20 $\mu\text{m} \times 20 \mu\text{m}$ cross sectional area was calculated to be on the order of 10^{-1} Pa and the meniscus was not extruded. However, when the thickness of the membrane was 200 nm, the pressure drop across the membrane was calculated to be on the order of 10^{-3} Pa and gravity drove the fluid meniscus upfront the membrane. The level of extrusion is determined by the competition between inertia force of a droplet and surface tension force of the suspension fluid. In other words, if the gravity force of the fluid outdoes surface tension force of the fluid, the transfer of the droplets is more inclined to occur. The dimensionless number, Weber number, $We = \frac{\rho V^2 D}{\sigma} = \frac{\text{(Inertia force driven by gravity)}}{\text{(Surface tension force)}}$ where ρ is the density of the solvent, V is the characteristic velocity of the fluid inside the pore, D is the diameter of the pore and σ is the surface tension of the solvent, is a good parameter to analyze the relative force scale of the viscous force to the surface tension force of the fluid. When the width of each pore was 20 μm , the pinch-off and transfer of the droplets from the bulk solvent occurred and the corresponding We was calculated to be on the order

of 10^{-8} . However, when the width of each pore was $4\ \mu\text{m}$, the droplets were not transferred to the substrate and the corresponding We was calculated to be on the order of 10^{-3} . It implies that there exists a minimum pore size where the transfer of the droplets from the printing head can be achieved. After the extrusion of the droplet meniscus is completed, the droplets of particle suspension are transferred to the substrate. Surface tension force of the printing head surface and the substrate are crucial factors in this step. While the extruded fluid meniscus is in contact with the substrate, the surface tension force of the substrate attracts a fraction of the fluid and picoliter scale droplets are transferred to the substrate after the pinch-off of the droplet. When the printing head surface was hydrophilic (water $\theta_c | 50^\circ$), the fluid wet the head surface and transfer of the droplets did not occur. When a printing head surface was hydrophobic (water $\theta_c | 109^\circ$) and the substrate was hydrophilic (water $\theta_c | 50^\circ$), high surface tension force of the substrate attracted the fluid and most of the fluid overflowed to the substrate and droplets were merged altogether. When both the head surface and the substrate were hydrophobic, surface tension force balance between the substrate and the head was achieved and picoliter scale droplets were transferred from the head to the substrate successfully. Also, when large volume of bulk suspension was loaded to the printing head, gravity-field force overwhelms the surface tension force of the fluid- meniscus and overflow of the fluid to substrate was observed during contact. The relative ratio of the gravity force of a global droplet contained in the printing to the surface tension force of the solvent is given by: Bond number, $Bo = \frac{\rho g R^2}{\sigma} = \frac{\text{Gravity force}}{\text{Surface tension force}}$ where ρ is the density of the solvent, g is the gravity acceleration, R is the radius of the global droplet, and σ is the surface tension force of the solvent. When $10\ \mu\text{l}$ volume of the bulk suspension was used with $200\ \mu\text{m}$ pore size of the head, Bo was calculated to be on the order of 10^{-1} . In this case, the transferred droplets were merged together to form a single droplet and separation of the individual droplet was not achieved. However, when $0.1\ \mu\text{l}$ volume was used, the corresponding Bo was calculated to be on the order of 10^{-3} and each droplet was separated implying that there exists a maximum threshold Bo number for the separation to occur. Generally, the volume of the loaded suspension does not affect the diameter of the transferred droplet on a surface significantly as long as the droplet merge does not occur. The volume of bulk suspension, pore size of

the printing head, and surface tension energy of the surface are critical parameters for the gravitational force, the surface tension force, and the viscous force to be placed in a right regime to accomplish successful transfer of the droplets. It is observed that the types of solvents, the types of the particles and the volume fraction of the particles affect the diameter of the transferred droplet since those factors determine the viscous and gravitational forces of each droplet. Creating a phase diagram for dimensionless parameters by incorporating various parameters of the suspension to predict the feasibility of the contact printing would be interesting subject of future work. Detailed calculations for this scaling analysis and pressure loss are included in Appendix B.1.

4.4. Rapid Evaporative Self-Assembly of Micro, nanoparticles on a Hydrophobic Surface

Evaporative self-assembly of micro, nanoparticles on a hydrophobic surface is a key phenomenon in forming 3D, high-aspect ratio particle clusters. It was previously reported that particles in colloidal suspensions form defect-free, 3D lattices after evaporation of the drops on hydrophobic surfaces[53, 55, 59, 94, 148-154]. Although some works featured rapid assembly during the formation of the lattices[94, 149, 154], quantitative, systematic studies of the evaporative self-assembly on a hydrophobic surface have not been performed due to lack of experimental platforms to observe evaporation processes. In this work, high optical transparency of a thin membrane of the printing head and low-concentrated suspensions enabled the real-time observation of the convective motion of particles through the optics in the system. Although it is still challenging to identify the exact particle clustering time, the time required for the evaporation of the picoliter-scale droplets, which is very valuable information to examine the kinetics of evaporative self-assembly of the particles, was able to be acquired through this method. Evaporation of picoliter-scale droplets of nanoparticle (100 nm gold, 30 nm zinc oxide) suspension was monitored by optical microscope in the system. Once the picoliter-scale droplet was generated by contacting the printing head with the substrate and following droplet pinch-off, contact line of the droplet receded

very fast and the evaporation of the droplet was completed by forming particle deposits at the center of initial droplet-contact line as shown in Figure 4.2.a.

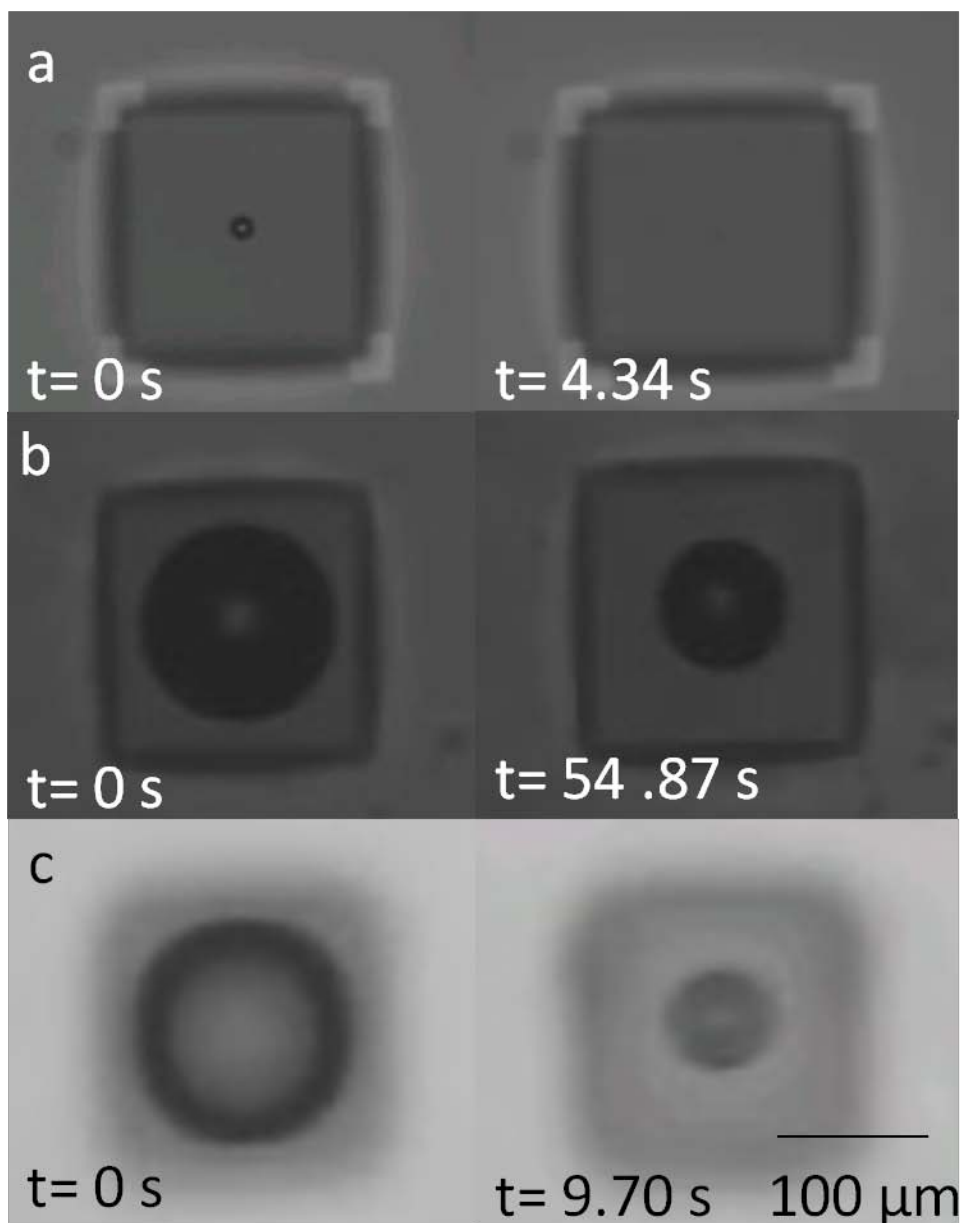


Figure 4.2 Optical snapshots of evaporating droplets after the pinch-off. (left) Right after the pinch-off. (right) After the completion of the evaporation a. Evaporation of 5×10^{-3} wt% gold nanoparticle suspension. A zoomed-in image is found in Figure 4.3.d.(iv). b. Evaporation of 1 wt% zinc oxide nano-particle suspension. c. Evaporation of 0.25 wt% zinc oxide nano-particle suspension.

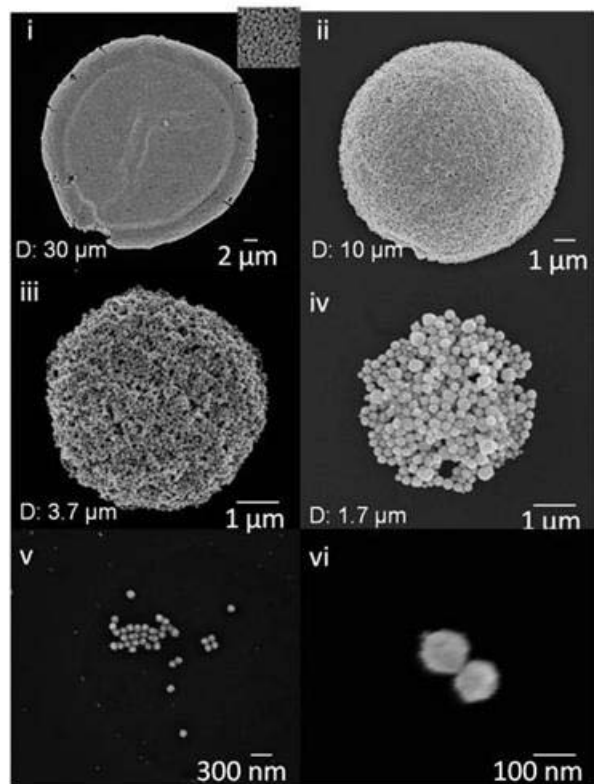


Figure 4.3 SEM views of gold nanoparticle (diameter ~ 100 nm) clusters printed from $200 \mu\text{m}$ head pore size. (i) A $30 \mu\text{m}$ diameter cluster printed from 5×10^{-1} wt%. (ii) A $10 \mu\text{m}$ diameter cluster printed from 5×10^{-2} wt%. (iii) A $3.7 \mu\text{m}$ diameter cluster printed from 5×10^{-3} wt%. (iv) A $1.75 \mu\text{m}$ diameter cluster printed from 5×10^{-4} wt%. (v) Dispersed particle clusters printed from 5×10^{-5} wt%. (vi) A bi-particle cluster printed from 5×10^{-6} wt%.

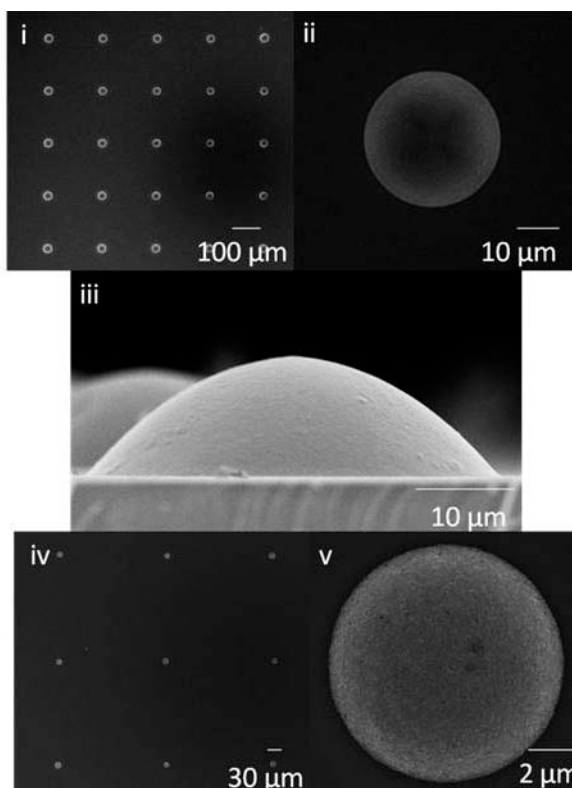


Figure 4.4 SEM views of zinc oxide nanoparticle (diameter/30 nm) clusters. (i-iii) 30 μm diameter clusters printed from 40 μm head pore size and 40 wt% concentration suspension. (i) High-throughput nanoparticle clusters. (ii) A close view of a single cluster. (iii) A cross sectional view of a single pattern (iv,v) 8 μm diameter clusters printed from 40 μm head pore size and 1 wt%. (iv) High-throughput nanoparticle clusters (v) A close view of a single cluster.

Generally, from macro to microliter scale of the droplet, either ring deposits are generated at the perimeter of the droplet by coffee-ring effect in case of high fraction suspension[49, 129, 130] or non-uniform deposits are generated inside the perimeter by Marangoni effect[49, 135]. According to the literatures[155-157], there are exceptional cases where a partial fraction of the particles are centered along with coffee ring deposits at certain special conditions, however, complete centering of all particles has not been reported yet. This is attributed to the fact that previous printing technologies were not capable of monitoring both the generation and the evaporation of picoliter-scale droplets of low concentrated-particle suspension simultaneously in-real time. This unique evaporating characteristic is explained by the scaling effect of picoliter scale droplets. Evaporation time of a droplet scales quadratically with length-scale of the droplet[158, 159]. In

evaporating, picoliter scale droplets on a hydrophobic surface, the evaporative rate is 100 times faster than microliter scale droplets and the evaporation proceeds by shrinking the contact line at constant contact angle mode[158]. In this mode, the transport of the particles is mainly dominated by the evaporation of the droplet, not the convective transport induced by hydrodynamic effect or thermal gradient of the droplet-Marangoni effect. Along with shrinking perimeter by evaporation, all particles in the droplet are centered. Generally, hydrophilic particles such as gold nanoparticles or silica microparticles, are not attracted to the hydrophobic substrate. Instead, dominant inter-particle forces such as electrostatic forces or van der Waals force cluster the particles during the evaporation of the droplet.[49] If the evaporation time is longer than clustering time, all particles are clustered first and centered after the completion of the evaporation. However, if the particle concentration is extremely low, inter-particle forces decrease and clustering of the particle proceeds slowly. Assuming that the change of low volume (weight) fraction of the particles does not affect the evaporation time of the fluid, there could exist a critical concentration where the deposition of the particles on the substrate is initiated before clustering of the particle is completed. In Figure 4.3.a, centering of the particles was observed until particle fraction of 5×10^{-4} wt% and dispersed clusters were observed from particle fraction of 5×10^{-5} wt%. It implies that the critical concentration for this particular system lies between those two concentrations. However, when hydrophobic particles such as zinc oxide particles were used, the particles are also attracted to the hydrophobic substrate. In this case, the particles are pinned at the contact line when the particle concentration of the droplet reaches to critical concentration.[129] As shown in Figure 4.2.b-c, when the concentration was very high, up to 40 wt%, the pinning of the particles occurred immediately after the droplet was transferred to the substrate. However, when the concentration was low, down to 1 wt%, the evaporation of the suspension had proceeded first and the pinning of the particle began when particle concentration inside the droplet reached to the critical concentration required for contact-line pinning. As a result, different concentrations of the particle suspension caused different timing of contact-line pinning. When the contact-line pinning was initiated earlier, the zinc oxide nanoparticle clusters of larger diameters were printed while the clusters of smaller diameters were when the pinning began later as shown in Figure 4.3 and Figure 4.4. Along with the initial volume fraction of the

particles in the original suspension, initial timing for contact line pinning determines the diameter of the zinc oxide nanoparticle clusters. Also the cross-sectional view of the zinc oxide nanoparticle clusters shows that its high-aspect ratio is lower than that of the gold nanoparticle clusters because some fraction of the zinc oxide nanoparticles were deposited downward and overall shape of the structures became widespread while all the gold nanoparticles were centered and formed the high-aspect ratio clusters. The pitch of the clusters was determined by lithographically defined pitch of the pores of the printing head and the size of the clusters was controlled by the volume fraction of the particles in the suspension and solvent drying behavior during the evaporation.

Arrays (~ 100 patterns) of microparticle (silica, polystyrene microparticles) clusters were printed on a hydrophobic substrate as demonstrated in Figure 4.5 and 4.6. Contact-line pinning of the particles did not occur because the hydrophilic particles were not attracted to the substrate. By simply diluting or concentrating the suspension, the size of the cluster was controlled. Contrary to the gold nanoparticle clusters, a critical concentration where clustering of the particles stops was not observed and even a single particle was centered. It is speculated that the lowest particle concentration, 1 wt%, still generates sufficient inter-particle forces to cluster particles within the evaporation time of the droplets. Clustering behavior of various particles in picoliter scale droplets is expected to generate numerous subjects of studies on fundamental colloidal science. Also, with this method, most of micro, nanostructures, or even biological particle clusters such as protein clusters, DNA clusters with any size and spacing will be able to be created on a hydrophobic surface.

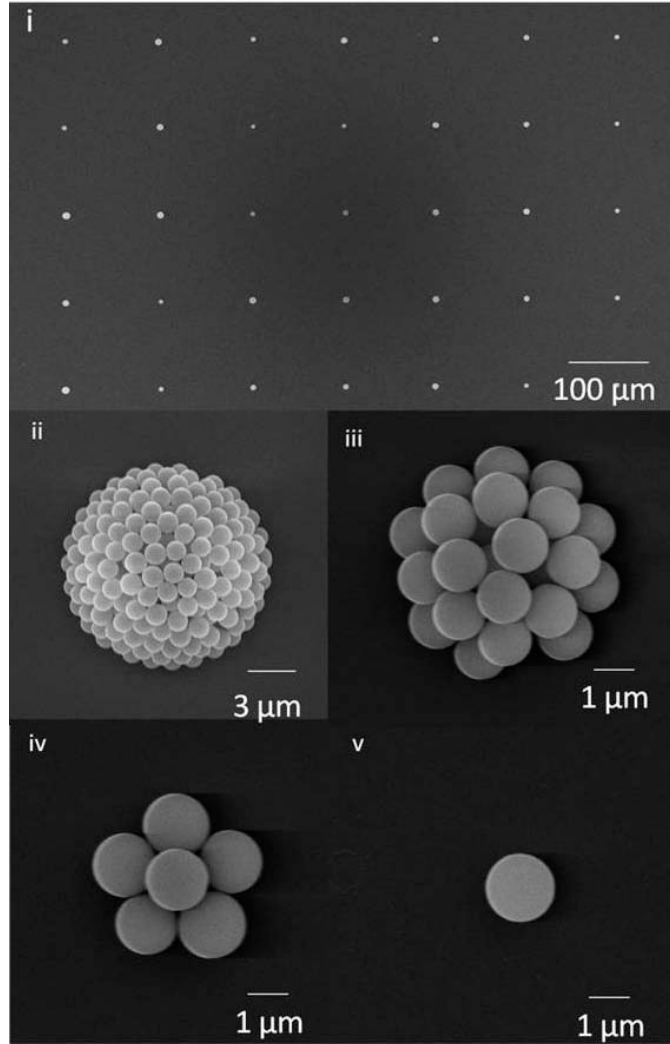


Figure 4.5 SEM views of silica microsphere (diameter/1 μm) clusters. (i) High-throughput clusters. (ii) A 10 μm diameter-cluster printed from 20 μm head pore size and 5 wt% (particle fraction) concentration. (iii) A 5 μm diameter-cluster printed from 20 μm head pore size and 2 wt% (particle fraction) concentration. (iv-v) Clusters printed from 20 μm head pore size and a 1 wt% (particle fraction) concentration. (iv) A 5-particle cluster. (v) A single particle. Note that the number range of particles are from 1 ~5 for entire area. This variation is caused by inherent statistical distribution of captured particle numbers per each pore.

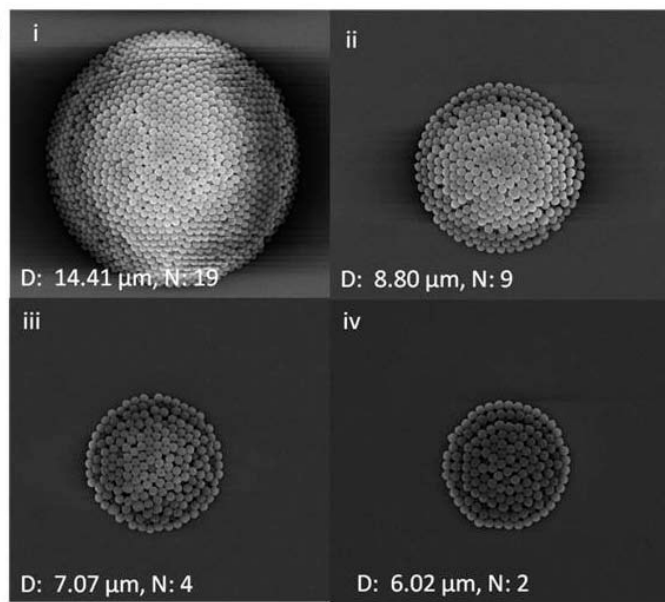


Figure 4.6 SEM views of polystyrene microsphere (diameter/1 μm) clusters. Clusters printed from (i) 0.34 wt% (ii) 0.68 wt% (iii) 1.35 wt% (iv) 2.70 wt% concentration. The number of layers, N , is corresponding to the center of the patterns.

4.5. Multiplexed Printing of Micro, Nanoparticle Clusters

A flexible membrane allowed the deformation of the head according to the previous clusters as illustrated in Figure 4.7.a. At given high aspect ratio, 0.33, a membrane (thickness: silicon: 100 nm, silicon nitride: 100 nm) was able to be conformed to 14 μm -height structure without breaking. Multi-layer process capability was demonstrated by printing zinc oxide nanoparticle clusters on gold electrodes. For the droplets of highly concentrated (~ 40 wt%) suspensions, contact line of the droplet was pinned and nanoparticles were continuously deposited on the electrodes-substrate interface as shown in Figure 4.7.b. A thin, single crystalline porous silicon membrane of the printing head has optical transparency over the visible light spectrum and the location of the printing head was monitored by optical microscope through the membrane. The location of the head was controlled by micron-axis stage of the stage as presented in Figure 4.7.c-d. The accuracy was realized to the equivalent level of conventional contact photolithography (~ 4 μm). Also, as shown in Figure 4.7.e-f, the alignment of the clusters with respect to previously printed clusters was demonstrated. Multiplex

printing of fluoro-microsphere clusters with different excitation/emission wavelengths were performed and visualized by fluorescence microscopy. Also, gold and zinc oxide nanoparticle clusters were printed on a target spot and the clusters were accurately positioned. Smaller patterns were created first to prevent the breaking of the membrane.

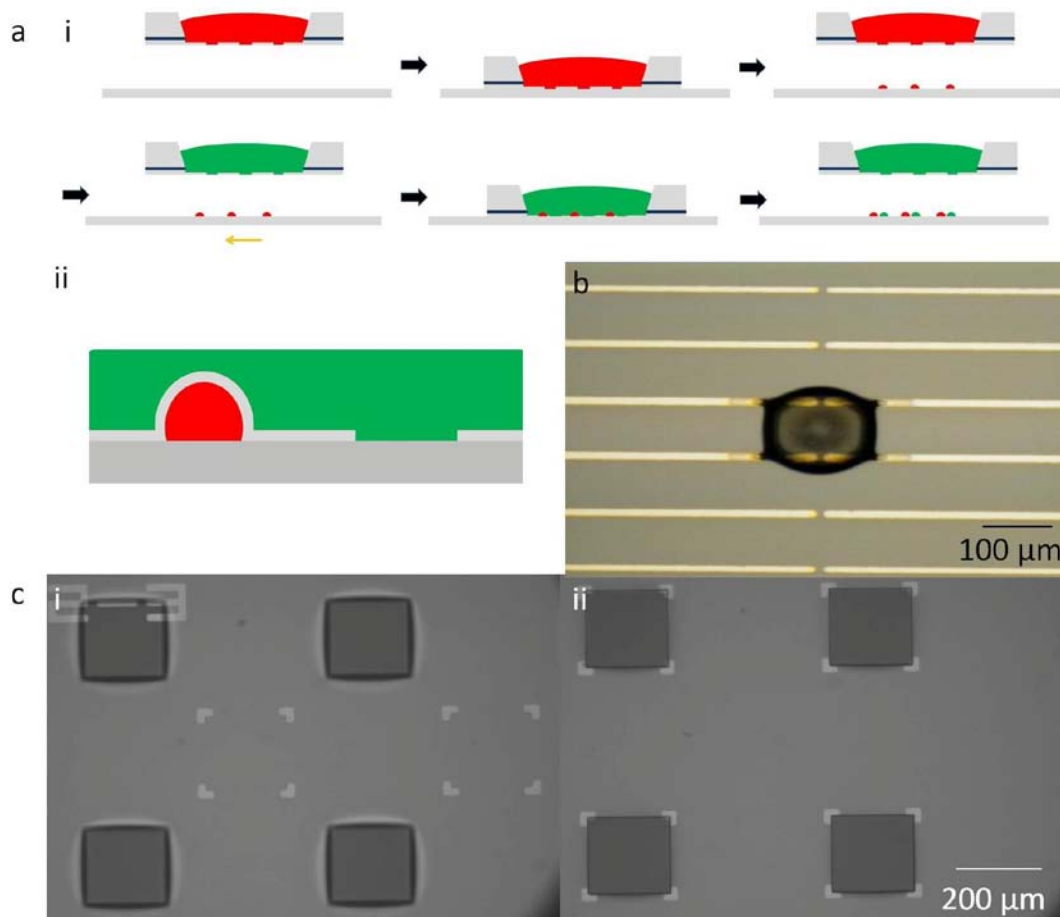


Figure 4.7 Multiplexed printing of micro, nanoparticle clusters a. Schematics of multiplex printing procedures. (i) A schematic of a series of printing methods. After an initial printing, the next step printing is achieved after the alignment of the head is achieved. (ii) An illustration of a deformed head membrane according to the previously printed clusters. b. A zinc oxide nanoparticle cluster (diameter: 40 nm) printed on gold electrodes (thickness: 25 nm) with alignment. The suspension concentration is 40 wt%. c. Top views from the printing head side. (i) Before alignment. (ii) After alignment. Alignment is achieved by manipulating a micro-precision stage.

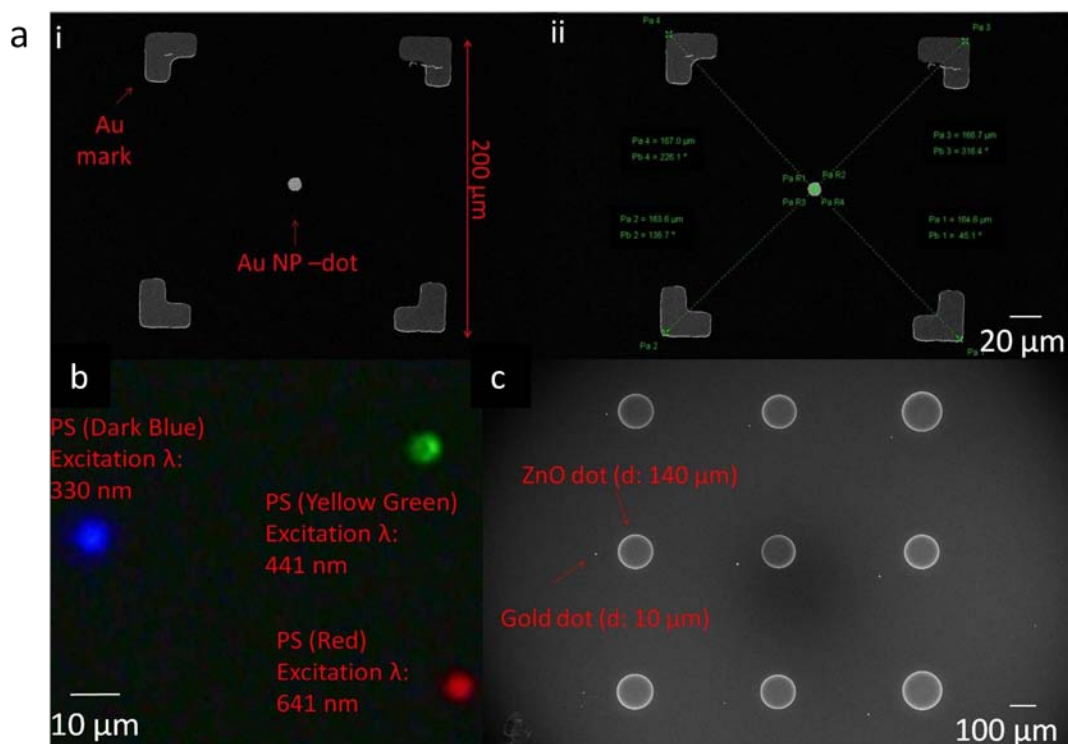


Figure 4.8 Multiplexed printing of micro, nanoparticle clusters a. SEM views of gold nanoparticle clusters (diameter: 100 nm) (i) A centered gold nanoparticle cluster with respect to gold alignment marks. (ii) An analyzed image of alignment accuracy. The accuracy is approximately 4 μm . b. Layover images of three different fluorescence images. Three different combinations of excitation filter and emission filter were used to acquire four different types of fluorescence light. c. Multi-step printing of zinc oxide nanoparticle (diameter: 140 μm) and gold nanoparticle clusters (diameter: 10 μm). Smaller clusters were printed first to prevent breaking the membrane.

Chapter 5. Studies on Particle Effects in Evaporative Self-Assembly by Numerical Simulation

5.1. Introduction

Evaporative self-assembly of solid-phase materials in liquid medium is beautiful science and envisions numerous engineering applications. Experimentally, the evaporative self-assembly of the various geometry-shaped solid materials have been successfully demonstrated in length scales from millimeter to nanometer scales in previous reports[96, 110, 125] for past decades. However, due to the complexity of the three-phase (liquid, solids and gas phases) systems, it is still challenging to understand and model the dynamics of the far-from-equilibrium, crystallization in evaporative self-assembly from theoretical stand point of views. Especially, in spite of its significance, there have been very few studies[96, 97, 160, 161] on examining the dynamics of the onset of the crystallization. In those studies, it has been generally accepted that the evaporative self-assembly of the particle is mainly initiated by the meniscus effect of evaporating, particle-carrier medium. However, lack of thorough analysis on the “onset” part of crystallization led to its incomplete justification because numerous hypothetical terms in those works, such as solvent evaporative flux, particle clustering flux, were not be able to be verified by adequate experimental apparatus or computational means. In this chapter, concrete experimental and computational evidences to claim that “particle effects” mainly drives the onset of the crystallization of the particles in far-from-equilibrium, evaporative self-assembly are reported. A new experimental apparatus was developed to study the regime where particle interactive forces become comparable to hydrodynamic, evaporative forces of an evaporating droplet.[147] The system was used to observe fast-evaporative self-assembly of particles in picoliter-scale droplets and evaporation time of the droplets was measured by real-time observation. Along with the experimental work, a particle-based computational model was developed to interpret the dynamics of evaporative self-assembly, to validate our claim. A particle-based computational method, which has been utilized to simulate the behaviors of particulate matters in “dry” conditions for numerous engineering applications[162-166], was used to simulate the

behaviors of particles in “wet” conditions by incorporating fluid-drag effect to Newton’s mechanics. Experimental and computational results were analyzed to support the argument that “particle effects” are majorly responsible for the onset of the crystallization in far-from-equilibrium, evaporative self-assembly of the particles.

5.2. Experimental Observation of Evaporative Self-Assembly of Particles

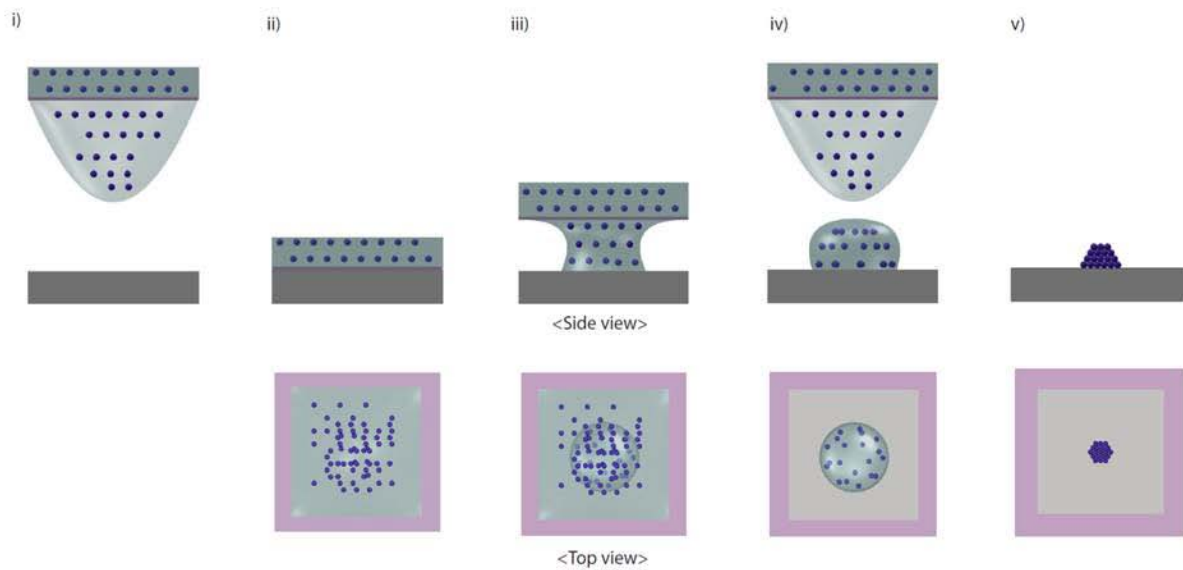


Figure 5.1 Schematics of printing procedure (i) Particle suspension menisci are extruded to the upfront end of the membrane by gravity. (ii) Contact of the head with the substrate is achieved. (iii) Surface tension of the substrate attracts a fraction of the suspension fluid. (iv) Picoliter-scale droplets are transferred to the substrate via pinch-off processes. (v) Rapid evaporative self-assembly of the particles forms 3-D clusters.

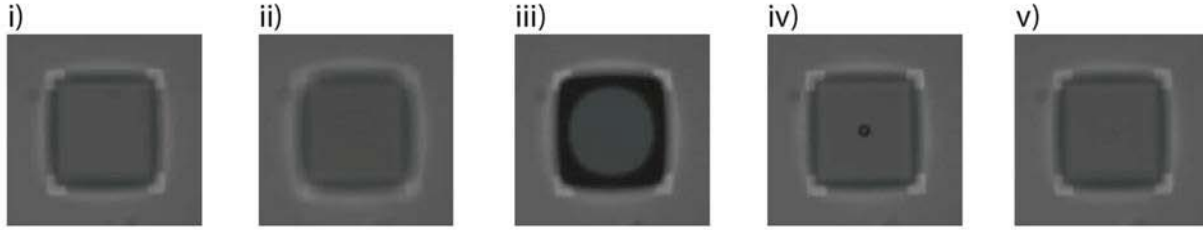


Figure 5.2 Optical snapshots of evaporating droplets after the pinch-off. Evaporation of 5×10^{-3} wt% gold nanoparticle suspension each part corresponds to the part in Figure 5.1. (i) Particle suspension menisci are extruded to the upfront end of the membrane by gravity. (ii) Contact of the head with the substrate is achieved. (iii) Surface tension of the substrate attracts a fraction of the suspension fluid. (iv) Picoliter- scale droplets are transferred to the substrate via pinch-off processes. (v) Rapid evaporative self-assembly of the particles forms 3-D clusters. A zoomed-in image is found in Figure 5.4.a.

5.3. Particle-based Computational Modeling

Conventionally, numerous multi-phase flow phenomena such as natural deposition of particles[49, 55, 56, 59, 129-131, 134, 135, 147, 148, 151, 153, 154, 167-172] or controlled-convective assembly[48, 93-100] of the particles in evaporative flows have been interpreted based on conventional hydrodynamic models. Assuming that the particles in evaporative flows behave as continuum species in the fluid, the motions of the particles are presumed to be coincided with the streamline of the fluid flow and only the ‘fluid’ part of particulate flow has been considered in the modeling. Although the global morphology of particles-deposits have been roughly simulated by these “fluid”-based approaches[49, 129-131, 134, 135, 173], micro-scopic views of particle-assembly behaviors were hardly studied due to the negligence of “particle effects” in the analysis. Particle effects, such as particle-particle, particle-solid or particle-fluid interactions, are generally caused by electrostatic forces, mass-based forces or surface-based forces.[166] Obviously, those forces present in evaporative self-assembly and actively associated with the evaporative flows, however, they have not been incorporated to conventional hydrodynamic models. Particle effects generally occur by non-continuous, discrete events and continuous function-based mathematical models in the hydrodynamic models are not capable of accounting

for those events. Recently, for the simulation of drying behavior of very small nanoparticles (diameter: $< 5 \text{ nm}$), a coarse-grain model was introduced to simulate the morphology of nanoparticle assembly by introducing particle-particle, particle-solid, particle-medium interaction factors.[125, 174, 175] This particle-based approach demonstrated accurate modeling of drying behaviors of very small nanoparticle assemblies in very small area ($< 10 \mu\text{m} \times 10 \mu\text{m}$), however, the range of the particle sizes and the area of modeling domains were hardly extended to macro- and micro- scales due to the computational limits. Also, the drag effect which is exerted by surrounding fluids to the particle, has not been considered in the analysis and the accuracy will be substantially degraded if this model is used for macro-, micro-scale particle simulations. Both previous approaches, hydrodynamic- and a coarse-grain-modeling methods, have been used to present either “fluid”-based or “particle”-based views of evaporative-self assembly, however, attempts to bridge these two views are lacking in concurrent studies. In order to develop integrative insights to understand evaporative self-assembly in a wide range of length scales of the evaporative system, it is desirable to implement adequate computational methods to observe and interpret the dynamics of the particles during the evaporative-self assembly.

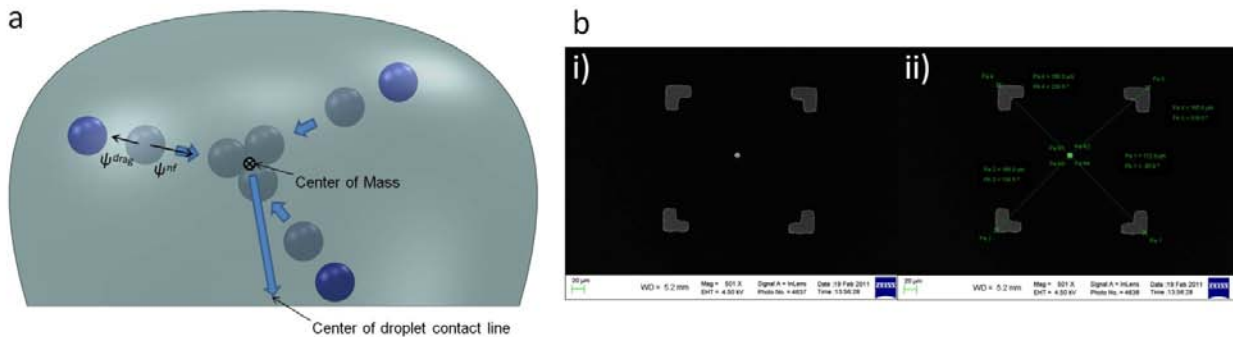


Figure 5.3 Centering of particle assemblies in evaporative self-assembly. a. A schematic of the motion of particles during assembly process. The particles are clustered to the center of mass of particle systems, first, and then, the cluster is deposited at the center of droplet contact-line. b. SEM views of gold nanoparticle clusters (diameter: 100 nm) (i) A centered gold nanoparticle cluster with respect to gold alignment marks. The marks indicate the location of the initial contact line of the droplet. (ii) An analyzed image of alignment accuracy. The accuracy is approximately $4 \mu\text{m}$.

A particle-based computational model was developed to simulate the crystallizing behaviors of particles in surrounding fluids during the evaporative self-assembly. By adding fluid-drag effect to the governing equations as described in Zohdi's work[166], newton's 2nd law of motion was implemented to each single particle. The governing equation is

$$m_i \ddot{r}_i + c_i \dot{r}_i = \psi_i^{tot} = \psi_i^{int} + \psi_i^{ext} \quad (5.1)$$

where r_i is the position vector of the i^{th} particle, m_i is the mass of a single particle, c_i is a drag coefficient applied on the i^{th} particle and ψ_i^{tot} is the sum of the forces acting on the i^{th} particle, due to other particles in the system (“internal” particle-to-particle near-fields, bonding forces, etc, ψ_i^{int} and due to the external electric and magnetic fields (ψ_i^{ext}).

In this system, it is assumed that

$$\psi_i^{ext} = 0 \quad (5.2)$$

$$\psi_i^{int} = \psi_i^{nf} + \psi_i^{con} + \psi_i^{fric} \quad (5.3)$$

where ψ_i^{nf} is the force due to near-field interaction, ψ_i^{con} is normal contact impulsive forces, and ψ_i^{fric} is frictional impulse forces. For ψ_i^{nf} , empirically-generated interaction laws for complex particulate ion-ion interaction were used to express attractive and repulsive components. A general form of ψ_i^{nf} is

$$\psi_i^{nf} = \sum_{j \neq i}^{N_P} (\alpha_{1ij} \|r_i - r_j\|^{-\beta_1} - \alpha_{2ij} \|r_i - r_j\|^{-\beta_2}) n_{ij} \quad (5.4)$$

where the α and β are empirical material parameters. In this work, the particles in an evaporating droplet were generally clustered to the center and only attractive forces were assumed to be present in the near-field interaction for the simplicity of computation and interpretation. It is very crucial to note that ψ_i^{nf} takes account not only inter-particle interaction forces but also the attraction generated by hydrodynamic effects. In other words, all factors which drives the particle assembly were incorporated into one source term, ψ_i^{nf} . A final form of ψ_i^{nf} is

$$\psi_i^{nf} = \sum_{j \neq i}^{N_p} (\alpha \|r_i - r_j\|^{-\beta}) n_{ij} \quad (5.5)$$

In this system, it is assumed that

$$\psi_i^{con} = 0 \quad (5.6)$$

$$\psi_i^{fric} = 0 \quad (5.7)$$

The governing equation can be solved recursively by recasting the relation as

$$r_i^{L+1,K} = G(r_i^{L+1,K-1}) + R_i \quad (5.8)$$

Where $K=1,2,3,\dots$ is the index of iteration within time step $L+1$ and R_i is a remainder term that does not depend on the solution, i.e.

$$R_i \neq R_i(r_1^{L+1}, r_2^{L+1} \dots r_N^{L+1}). \quad (5.9)$$

The position of i^{th} particle was implicitly expressed as

$$r_i^{L+1,K} = r_i^L + \underbrace{\frac{1}{1 + \frac{\Delta t}{m_i} \left(\frac{1}{2} \rho v_i^L C_D A \right) \phi} \left(v_i^L \Delta t + \frac{\phi (\Delta t)^2}{m_i} (1 - \phi) \psi_i^{nf,L} \right)}_R + \underbrace{\frac{1}{1 + \frac{\Delta t}{m_i} \left(\frac{1}{2} \rho v_i^L C_D A \right) \phi} \left(\frac{(\phi \Delta t)^2}{m_i} \psi_i^{nf,L+1} \right)}_{G(r^{L+1,K-1})}$$

(5.10)

where

$$\psi_i^{nf,L} \stackrel{\text{def}}{=} \psi_i^{nf,L} (r_1^L, r_2^L \dots r_N^L) \quad (5.11)$$

and

$$\psi_i^{nf,L+1,K-1} \stackrel{\text{def}}{=} \psi_i^{nf,L+1,K-1} (r_1^{L+1,K-1}, r_2^{L+1,K-1} \dots r_N^{L+1,K-1}) \quad (5.12)$$

Near-field potential, ψ_{ij} , was assigned in a form of $\psi_{ij} = \alpha \|r_i - r_j\|^{-\beta}$. For the convenience, β was set to 1 so that only one variable, α , can reflect all inter-active potential effects. The magnitude order of α was determined by finding the point where the iterative error and the discretization errors become comparable. Time step, Δt , needs to be properly determined in order for the iterative schemes to be converged within a designated number of time steps while the resulted iterative error does not reach the discretization error. Δt was set to be a certain value so that the magnitude order of the iterative error, $\|r_i^{L+1,K} - r_i^L\|$ lies between the length scale of particle diameter and an order below. Total assembly time of the particle clusters, T , was iteratively estimated by varying main two parameters, initial assembly time, T_i , and iteration number, N . Estimated assembly time, T_e , was calculated by $T_e = \sum_{i=1}^N \Delta t$ and compared with T_i . Guessing T_i and N were attempted until $t_r \stackrel{\text{def}}{=} \frac{\|T_s - T_i\|}{T_i}$ (Error between initial assembly time and estimated assembly time) becomes less than 0.01. After this condition is satisfied, T was assigned as T_i . After the creation of droplets on the surface from a printing head, it was assumed that the particles in the droplets are initially, randomly dispersed. N (number of particles in a droplet) sets of three variables in spherical coordinate systems, ρ, θ, ϕ were randomly generated and x, y, z were calculated from the sets. The iterative schemes were designed to be terminated when the average distance between particles was calculated to be less than the particle diameter. Details of the iterative solution schemes, computational algorithms, calculation of total assembly time and determination of the distribution of initial particle displacement are available in Appendix C.

5.4. Analysis on Particle Assemblies

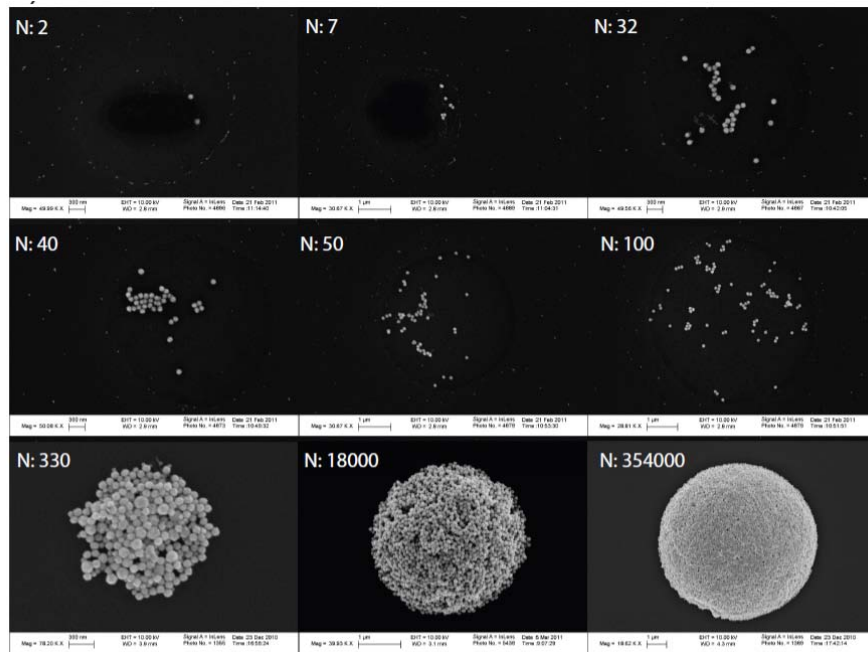


Figure 5.4 SEM views of gold nanoparticle (diameter ~ 100 nm) clusters. N corresponds to observed (or estimated) number of particles. The number of particles, N , was either counted from SEM images of assemblies, or estimated by assuming hemisphere geometries and complete packing cases where packing ratio was assumed to be 0.707.

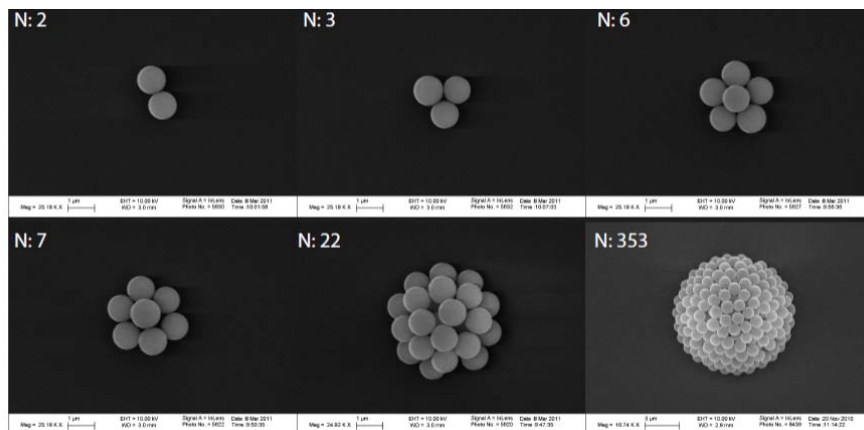


Figure 5.5 SEM views of silica microsphere (diameter ~ 1 μ m) clusters.

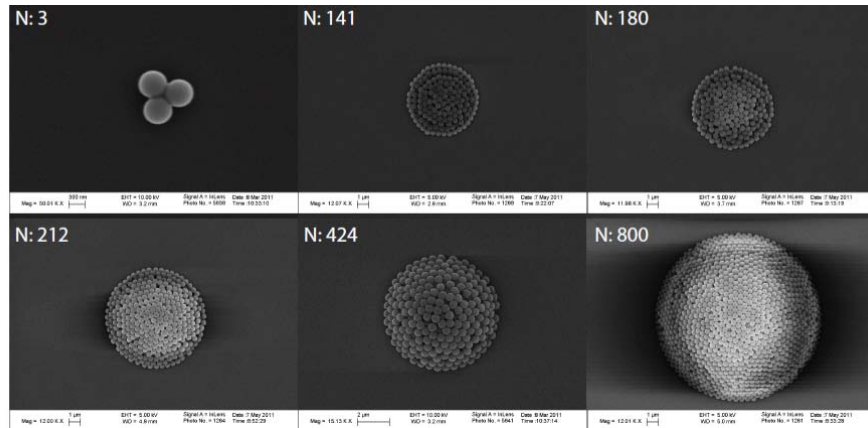


Figure 5.6 SEM views of polystyrene microsphere clusters.

As observed in Figure 5.4, 5.5 and 5.6, silica microparticles and polystyrene microparticles over whole range of number of particles were clustered and formed hemisphere-shaped particle assemblies. However, gold nanoparticles were centered completely only if the number of the particles exceeds over a certain critical value, (in Figure 5.4, $N=330$) forming hemisphere-shaped assemblies as similar to silica / polystyrene microparticle cases. Otherwise, the particles were randomly dispersed without clustering. In order to interpret the drying behaviors, a computational method was used to estimate the particle assembly time at given parameters as described in the previous section. For each material, the magnitude order of α is determined iteratively by running a few sample simulations, to find a point where estimated total assembly time is consistent with experimentally observed-evaporation time of the suspension droplets. For example, when the centering of the particles was completed prior to the evaporation of the droplets, α is determined in a way that the evaporation time of droplets resides over computed total assembly time. However, if the regime where complete centering and dispersion of the particles co-exist is found for certain material, such as Gold nanoparticles in Figure 5.4, α was determined in a way that the evaporation time of the droplets lies in the range of total assembly time for each number of particles.

Table 5.1 Summary of estimated parameters used for computations

	Time step (Δt , second)	Alpha (α)
Silica microparticle (d: 1 μ m)	10^{-3}	10^{-12}
Gold nanoparticle (d: 100 nm)	10^{-2}	10^{-16}
PS microparticle (d: 0.5 μ m)	5×10^{-4}	10^{-13}

Estimated parameters that were used for the computations are summarized in Table 5.1. Variation of α with different materials demonstrates that “Particle effects” varies significantly with different materials. By analyzing the displacement of the particles, the computed assembly time and experimentally-observed evaporation time of the suspension droplets, the particle assembly behavior during the evaporative self-assembly was successfully interpreted. The initial displacement of the particles, computed final displacement of particles and center of mass of total particle systems were calculated according to the number of particles in the systems. They are summarized in Table 5.2. As verified in Table 5.2, in silica particle cases, all particles in the given system were merged to the center of mass of the system regardless of the number of the particles. This result is good supporting evidence that the assembly of the particles is completed prior to the evaporation of the droplets. Also, this calculation is consistent with exact centering of the particle cluster with respect to initial droplet contact line as shown in Figure 5.2. It is anticipated that rapid evaporation of the suspension droplet proceeded toward center point of droplet contact-line and drives the clustered particles from the center of mass to the center of droplet contact-line. Experimental data from Figure 5.4, 5.5, 5.6 and computational data from Table 5.1, 5.2 imply that particle-particle attractive forces dominates over the evaporative force of the medium in the regimes when particle clusters are formed at the center of the printing area. If the initial particle-nucleation is driven by the meniscus effect of evaporating medium as claimed in the previous works[160, 161], the clustering and the evaporation of the liquid medium should occur simultaneously, however, the experimental and computational results strongly suggest that there exists timing-discrepancy between the completion of particle clustering and the completion of the evaporation of the droplets.

Table 5.2 Calculated initial particle displacement, final displacement and center of mass of particle systems for $N=2,3,4,5,6$. Unit: μm

Number of particles	Initial displacement			Computed final displacement			Center of mass		
2	17.87	-4.89	34.31	12.52	-3.26	54.73	12.38	-3.22	55.28
	6.89	-1.55	76.24	12.24	-3.17	55.81			
3	-32.72	-98.74	15.54	3.22	-38.95	36.99	3.31	-38.79	37.03
	11.66	-9.54	32.38	3.30	-38.64	36.92			
	30.98	-8.10	63.18	3.41	-38.79	37.20			
4	0.03	0.01	2.13	4.09	9.55	74.86	4.10	9.68	75.08
	-7.03	2.65	8.79	3.84	9.77	75.05			
	3.21	2.54	6.33	4.14	9.90	75.10			
	5.43	-1.33	12.78	4.30	9.57	75.27			
5	17.34	-4.90	28.64	-10.35	19.41	34.81	-10.71	19.53	34.80
	-2.44	-1.25	56.48	-10.76	19.37	35.13			
	1.69	0.67	13.38	-10.87	19.28	34.56			
	0.89	9.31	15.93	-10.60	19.79	34.58			
	-71.05	93.81	59.55	-10.97	19.78	34.91			
6	10.06	-54.48	77.37	4.65	-8.35	39.85	4.75	-7.93	39.72
	-0.4	-1.79	19.03	4.31	-7.87	39.64			
	59.81	-41.35	70.06	5.19	-7.94	39.79			
	11.57	-9.46	0.00	4.84	-8.1	39.32			
	-46.08	78.87	5.77	4.78	-7.50	39.59			
	-6.46	-19.35	66.11	4.72	-7.81	40.16			

In other words, only if the clustering rate of the particles and the evaporative rate of the liquid medium are different from each other, both the complete centering of the particles and the dispersed particle clustering, which were observed in Figure 5.4 can be explained. Otherwise, the particle clusters will be deposited at different locations other than the center of the droplet contact line. This observation motivates us to claim that the onset of evaporative self-assembly is mainly dominated by particle-particle interactions rather than the evaporation of liquid medium although the evaporation might continue the growth-process of the clusters by carrying the particles. The particle-interaction forces such as electrostatic-based, mass-based or surface-based forces may initiate the particle assembly and the role of fluid is limited to assist the transportation of the particle to the formed assemblies, not initiate the assembly. The term “evaporative self-

assembly” becomes self-inconsistent in taking account for micro-scopic particle-particle or particle-substrate (or any other type of solid materials beside particles) interactions in the initial stage of evaporative self-assembly. If particle-particle attractive force does not reach the evaporative force of the liquid medium, hydrodynamic effect of the evaporating medium dominates over particle effect and particles are dispersed after the completion of the evaporation as shown in gold nanoparticle case. In this case, it was approximated that the particles are carried by the fluid and apply conventional hydrodynamic models to explain the transportation of the particles. Interpretation of numerous, evaporative self-assembly-based phenomenon, such as convective assembly[48, 93-100], coffee-ring effect[49, 129-131, 151, 167-170], or rapid self-assembly on hydrophobic surfaces[55, 56, 147, 148, 153, 154, 172] can be greatly helped by using this interpretation. For instance, in coffee-ring effect, a number of previous works[49, 129-131, 134, 135, 173] have attempted to explain the particle-pinning on the substrate by applying hydrodynamic models. In those approaches, crude assumptions to validate mathematical models have resulted in incomplete description of the phenomena. However, if micro-scopic views are applied to three-phase contact-line where particles, substrate and the liquid medium co-exist, it is interpreted that the initial particle-pinning on the substrate is driven by particle-substrate and particle-particle attractive force. The particle-substrate attractive force, which is an equivalent to ψ_i^{nf} , is maximized at the edge of the droplet where the thickness of the medium is minimal. Drag-effect of the particles is minimized and only ψ_i^{nf} term drives the particle-pinning at the edge of the three-phase contact line. This interpretation is also analogous with the claim presented in Shen’s work[169] that the lower limiting size of a coffee ring is dependent on the time scale competition between the liquid evaporation and the movement of suspended particles. When the liquid evaporates much faster than the particle movement near a three-phase contact line, coffee ring cannot be formed successfully. Instead, these particles will disperse uniformly on a surface upon the completion of liquid medium-evaporation. In our experimental platform, instead of coffee-ring, high aspect ratio-particle clusters are formed if the clustering speed of the particles, driven by particle-particle interaction, outdoes the evaporative rate of the liquid. The onset of the particle- nucleation is coincided with the initial formation of high-aspect particle assembly and it is, again, argued that dominance

of “particle effect” over “hydrodynamic effect” of evaporating medium is a necessary condition to initiate the onset of evaporative self-assembly. In the same manner, the initial nucleation of the colloids in convective assembly can be interpreted without incorporating vague “solvent – evaporative term” as described in earlier works[48, 95-97]. Particle-particle interaction forces are maximized wherever the thickness of the medium is thinnest, by the decrease of drag effect from the fluid, and evaporative self-assembly of the particles is initiated from that point and propagated to the rest of the region. Also, this analysis shows that “particle effect” can provide reasonable accounts for interpreting local particle assembly behaviors shown in multi-phase flow phenomenon, which conventional hydrodynamic models were not able to do.

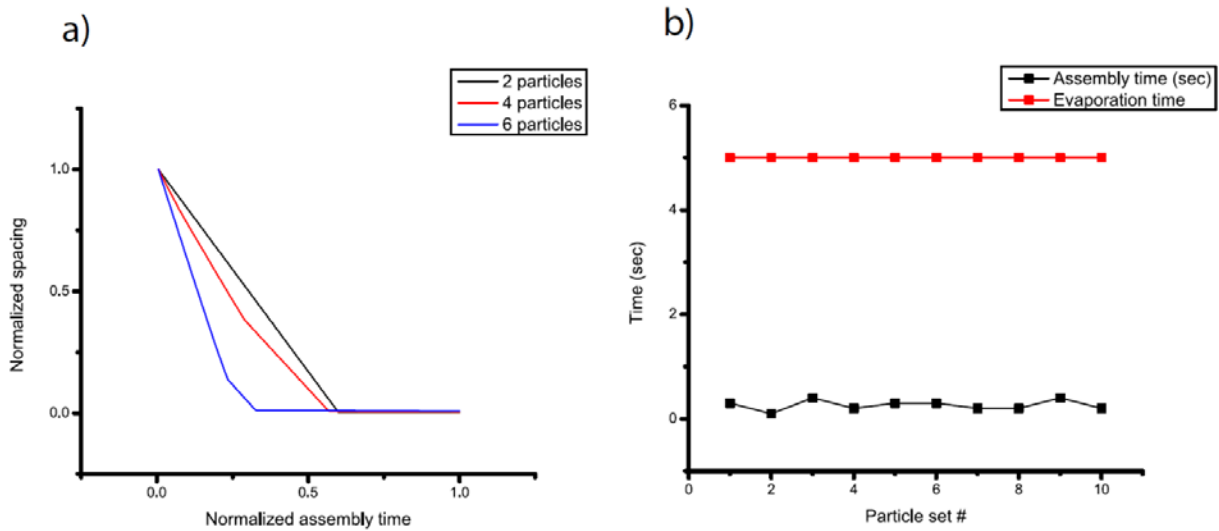


Figure 5.7 a. Normalized average inter-particle distance with respect to normalized assembly time. 2 particles, 4 particles and 6 particle-silica particle systems are used. b. Particle assembly time of 10 different sets of 2-particle systems and comparison with the evaporation time of the droplet.

Particle assembly time of 10 different sets of 2-particle system were computed and compared with the evaporation time of the droplets as shown in Figure 5.7.a. This figure demonstrates that the particle assembly takes less time than the evaporation of the droplets does for all randomly distributed initial particle displacements. The particle assembly behavior was examined by computing inter-particle spacing with respect to time, based on the computational methods as described. When two particles are clustered, the spacing decreases linearly until the

completion of the assembly. The trend of the decrease becomes steeper as the number of the particle increases because the total sum of particle interactive forces increases and the total acceleration of the system toward the center of mass also increases as well. The trend of total assembly time with the number of particles was studied in-depth as following.

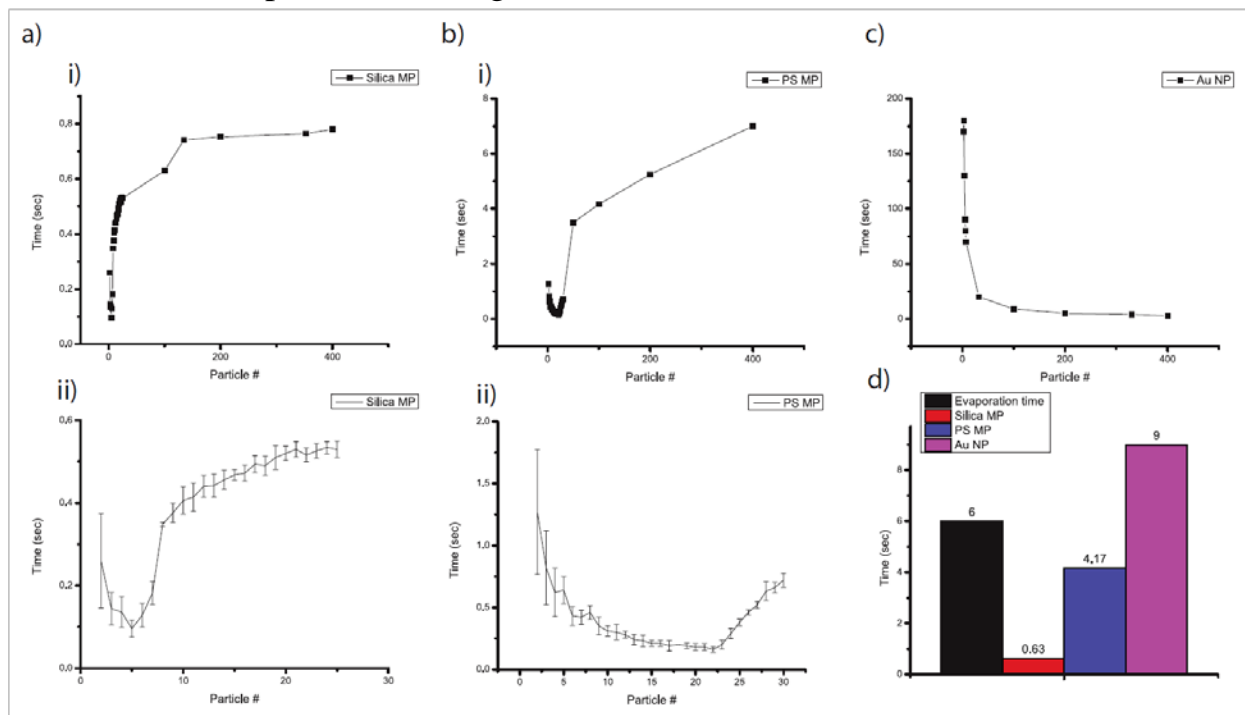


Figure 5.8 Particle assembly time with respect to the number of particles. The dot indicates actual data points that are coincided with the experimental results obtained from the printing. i) The range of particle # is from 2 to 400 ii) A zoomed part of i) graph near the turning point of the slope of (Time) / (Particle). The error bar shows the variation of assembly time by the initial random distribution of 5 different sets of 2 particle systems. a. Silica microparticles, b. Polystyrene microparticles. c. Gold nanoparticles d. Comparison of particle assembly time with evaporation time of the droplet in case the particle number is fixed to 100 for all types of particles.

As shown in Figure 5.8, trend of assembly time with the number of the particles varies with the types of the materials. The range of the number of the particles is from 2 to 400. In both Silica and Polystyrene cases, all assembly time reside within the total evaporation time of the droplet. The assembly time was decreased from the number of particles, 2 to the certain number and increases until the last number, 400. In the regime of low particle numbers, it is easily understood that the assembly time decreases as the number of the particles increases due to the

increase of total sum of particle interactive forces. Interestingly, if the number of the particles exceeds over a critical value, the assembly time increases. In order to understand this result more thoroughly, scaling analysis of the governing equation, (1), was performed by non-dimensionalization as following.

$$\left(\frac{MU^2}{L}\right) m_i^* \ddot{r}_i^* + \left(\frac{MU}{L}\right) c_i^* \dot{r}_i^* = \left(\frac{N-1}{L}\right) \sum_{j \neq i}^{N_P} (\alpha \|r_i^* - r_j^*\|^{-1}) n_{ij} \quad (5.13)$$

where * represents dimensionless parameter, M is a characteristic mass of the particle, U is a characteristic velocity of the particle, L is a characteristic length of the particle and N is the number of particles in the system. By dividing the denominator of the first term, the equation becomes

$$m_i^* \ddot{r}_i^* + \underbrace{\left(\frac{1}{U}\right) c_i^* \dot{r}_i^*}_{\text{Drag term}} = \underbrace{\left(\frac{N-1}{MU^2}\right) \sum_{j \neq i}^{N_P} (\alpha \|r_i^* - r_j^*\|^{-1}) n_{ij}}_{\text{Particle-interaction term}} \quad (5.14)$$

The acceleration of the particle is determined by the competition between drag term and particle-interaction term. Drag term scales with $\frac{1}{U}$ and the particle-interaction term scales with $\frac{(N-1)}{MU^2}$. In low particle number regime, as the particle number increases, the particle-interaction term increases and the drag term does not change significantly because the velocity does not vary drastically by adding a few more particles to the existing system. However, in high particle number regime, as the particle number increases significantly, the velocity of the particle increases by particle-interaction forces and the drag term relatively becomes more dominant than particle-interaction term. As a result, the acceleration of the particles decreases and the total particle assembly time increases. However, in case of gold nanoparticle, the high particle number regime is not found and the assembly time decreases as the particle number increases. As shown in Figure 5.6, there is a critical number of gold nanoparticles (~300) where the cluster starts being formed. The critical number of the particles is a corresponding particle number where the evaporation time of the droplet is equal to the particle assembly time. If the number is below the critical number, the particles are not clustered and randomly dispersed as shown in Figure 5.4. In other words, if the particle assembly

time at certain particle number is calculated to be longer than the evaporation time of the droplet, the clustering is not achieved and the particles will be randomly dispersed. Overall, the obtained simulation results show very good consistency with the experimental observation shown in Figure 5.3, 5.4, 5.5 and 5.6, verifying that the particle-based computational method is a proper tool to simulate particle assembly behaviors in the evaporative self-assembly.

Chapter 6. Electrical, Optical Characterization of Micro, Nanoparticle Assemblies

6.1. Introduction

In chapter 6, in order to envision practical applications of 3D patterns of crystallized micro, nanoparticle assemblies, electrical and optical characterization of 3D, crystallized particle assemblies were performed to demonstrate the feasibility of the developed systems for rapid, direct characterizations of various target species. Three types of particle assemblies; (a) Zinc oxide|(ZnO) nanoparticle assemblies, (b) Polystyrene|(PS) microparticle assemblies and (c) Gold|(Au) nanoparticle assemblies are created and characterized. 3D crystallized, ZnO nanoparticle assemblies were created via template nanoparticle assembly by thin-liquid film flow, placed between two gold|(Au) electrodes for UV light I-V characterization[176]. Various sizes of crystallized, polystyrene particle assemblies were created via printed micro, nanoparticle assembly by micro scale evaporative flow and size-tunability of the created assemblies was examined by fluorescence measurement[147]. Also, high-aspect ratio arrays of gold|(Au) nanoparticle crystallized assemblies were created via printed micro, nanoparticle assembly and size-uniformity of the created clusters was thoroughly analyzed by examining uniform, large arrays of gold nanoparticle clusters based on Surface Enhanced Raman Spectroscopy (SERS)[147]. The SERS measurements showed that size-tunable, large arrays of nanoparticle crystallized clusters were created from printed nanoparticle assembly method.

6.2. Creation of 3D ZnO Nanoparticle Assemblies on Gold Electrodes

A novel manufacturing method, “High resolution screen printing of nanoparticles enabled by in situ creation and mechanical lift-off of a polymer template”[176] was used to create 3D ZnO nanoparticle assemblies on micro-scale gold electrodes.

For the fabrication of gold electrodes, conventional micro-fabrication method was used as following: 100 nm of thermal oxide was grown on a lightly doped p-type silicon wafer and photoresist was spincoated. After photolithography, 5 nm of chrome and 25 nm of gold were deposited by thermal evaporation, followed by lift-off. Multiple electrodes of 10 μm width and 80 μm pitch with bond pads for packing were defined per each 1 cm x 1 cm die in the photo-mask. After the fabrication of gold electrodes, the wafer was diced into dies and a cellulose acetate template was patterned on the electrodes by the manufacturing method as illustrated in Figure 6.1.

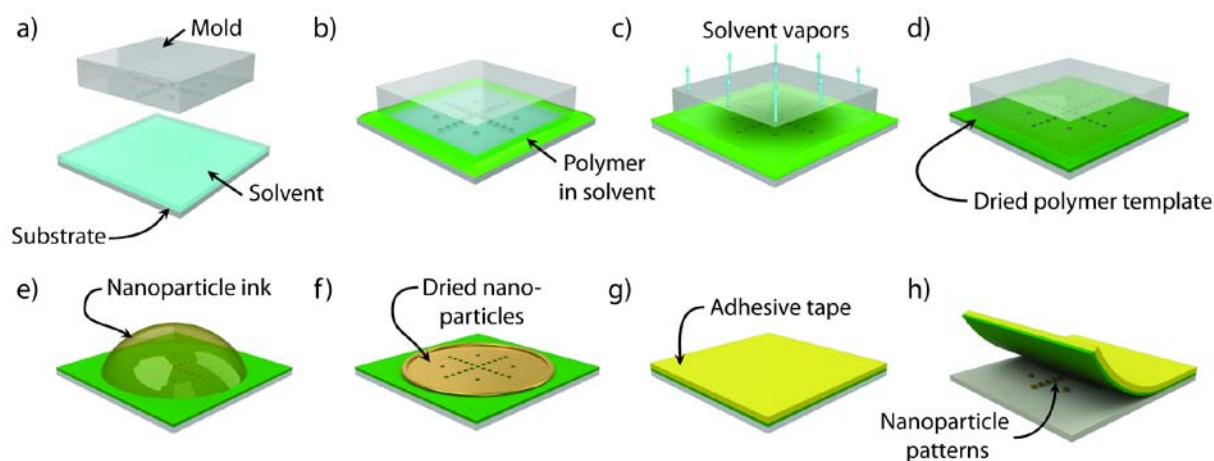


Figure 6.1 The patterning process. a) A porous polymer mold is positioned above a substrate coated with clean solvent. b) The mold is used to pattern the solvent, and polymer ink is introduced around the sides of the mold. c) The solvent evaporates and diffuses through the mold, drawing the ink inside and concentrating the polymer, until d) all of the solvent is removed and only polymer remains. e) The mold is removed and a droplet of nanoparticle ink is placed on the polymer template. f) The nanoparticle ink solvent dries, leaving a coffee-ring. g) Tape is placed over the template and coffee ring, and h) the template is pulled from the substrate, leaving only the nanoparticle patterns. Once the cellulose acetate pattern was made, the zinc oxide nanoparticles were deposited and lift-off was completed.

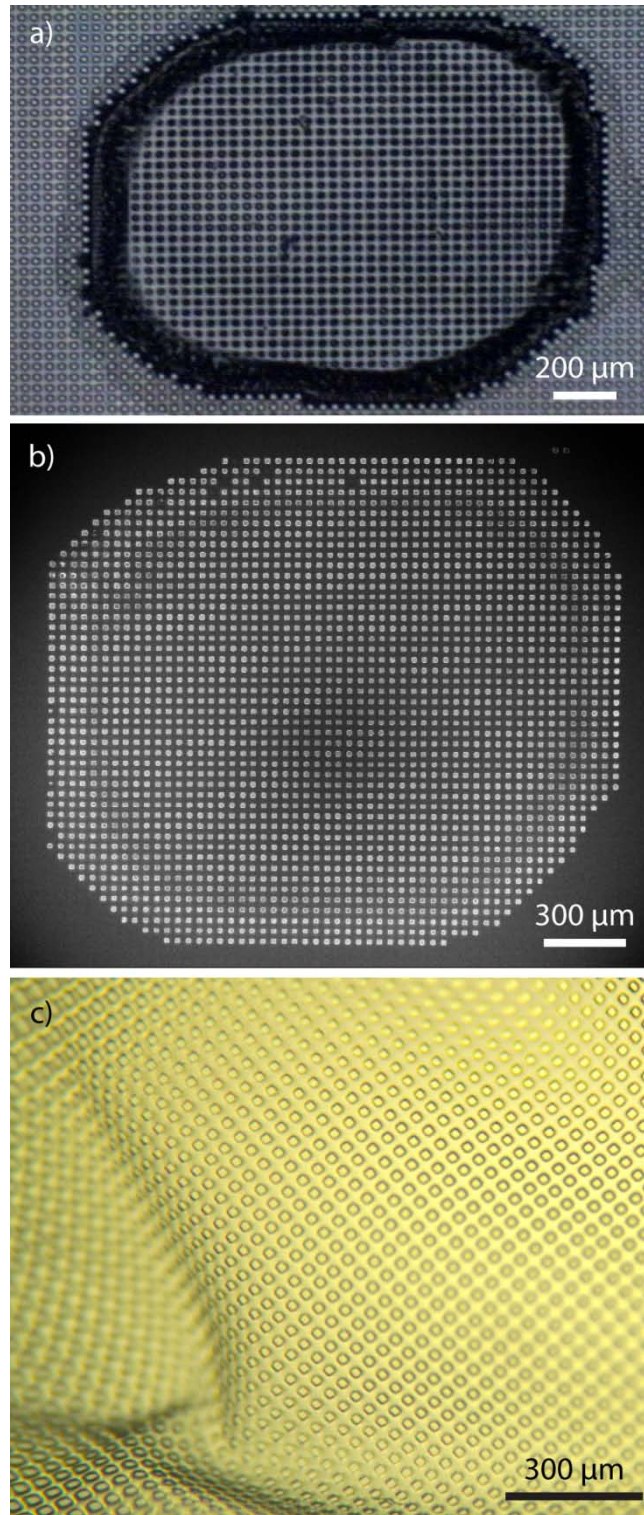


Figure 6.2 a) Optical micrograph of ZnO nanoparticles in a coffee ring on a cellulose acetate template on silicon. b) SEM micrograph of nanoparticle patterns on a silicon substrate after lift-off. c) Optical micrograph of a released cellulose acetate film.

The nanoparticle patterns on a silicon substrate are shown before and after template lift-off in Figure 6.2, along with an image of a released cellulose acetate template after non-destructive removal from the substrate with tweezers. Detailed images of the final patterning results are shown in Figure 6.3. A large, dense array of isolated squares of particles with a width of 20 μm at a 1:1, 1:2, and 1:4 spacing were formed on the substrate. Each individual square showed good, uniform packing of nanoparticles with no visible cracks or defects. The height of the patterned features were found to be quite uniform over the printed area, except for an increase in height for features near the location of the coffee ring on the template as shown in Figure 6.4. This height variation could be eliminated simply by avoiding placing features directly under the coffee ring. It is interesting to note that nanoparticles pinning the contact line at the edge of the droplet play a significant role in ensuring uniform deposition of nanoparticles inside the coffee-ring region. While nanoparticles are being deposited downward by an electrostatic attractive force induced by the hydrophilic surface charge, excessive particles are convectively transported toward the edge and form a thick coffee-ring deposit. This transport is caused by a hydrodynamic effect of an evaporating droplet and occurs only if the contact line is pinned at the edge of the droplet[49, 130]. If the volume fraction of the particles is too low, the contact line will not be pinned and particles are deposited as it recedes, causing the feature heights to vary. As shown in Figure 6.4, the thinnest features to be uniformly deposited were created using a 1 wt% nanoparticle solution, resulting in a layer with a thickness around 300 nm and with dimple structures caused by the fluid-air interface instability. In 0.25 wt% or 0.5 wt% solutions, pinning of the contact line did not occur. Solution concentrations between 0.5 wt% and 1 wt% are expected to generate incomplete coverage in deposition. Finally, the sidewalls of the patterned features do show some fracture due to shearing force caused by the mechanical lift-off, resulting in nearly 45 ° sidewalls, which are seen to be very repeatable.

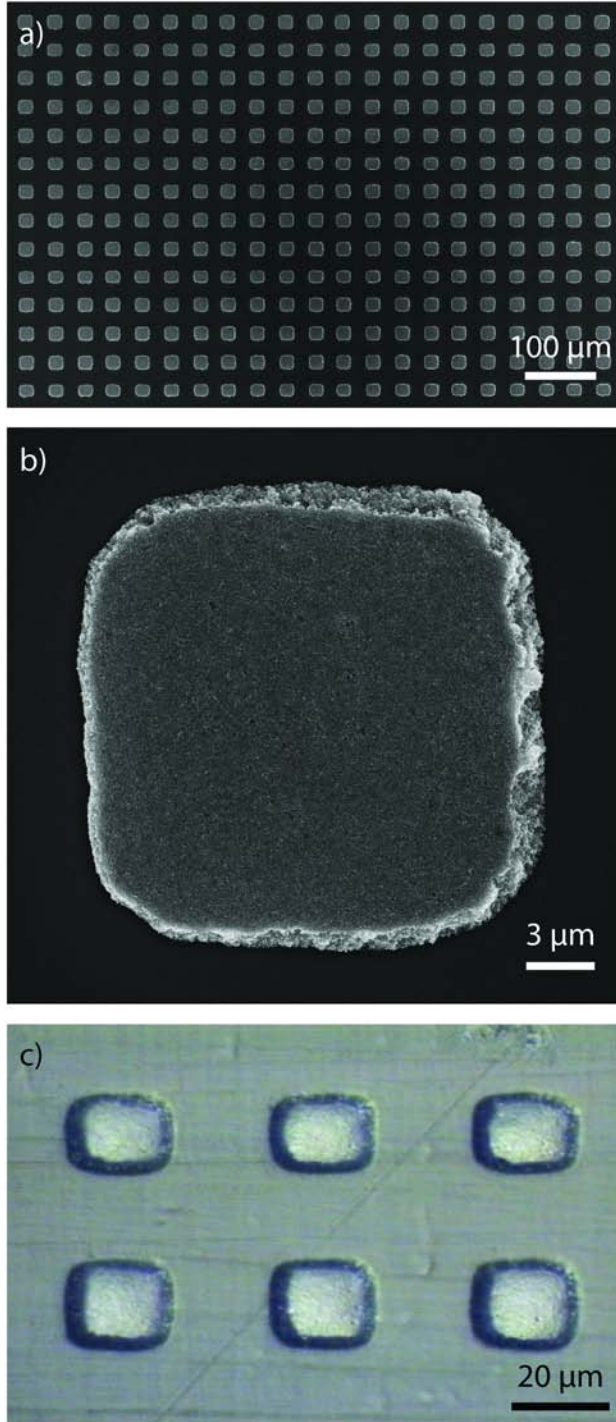


Figure 6.3 SEM micrographs of ZnO nanoparticles on a silicon substrate a) in a large array with 1:1 spacing and b) individually. c) Optical micrograph of ZnO nanoparticles on a COC substrate

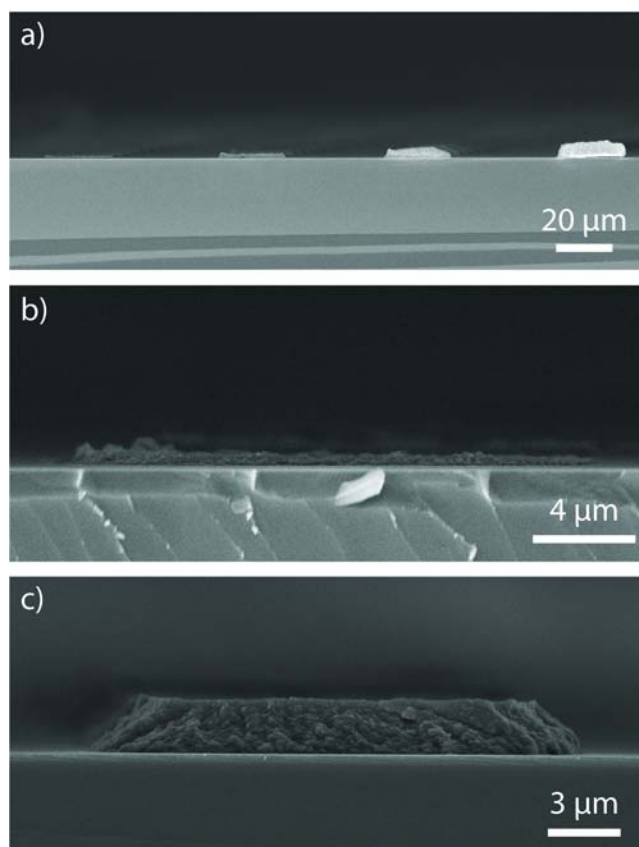


Figure 6.4 SEM micrographs of ZnO nanoparticles on a silicon substrate, showing a) the variation in height of patterned features directly under the coffee ring and b) small and c) large patterned heights in the center of the patterned area away from the coffee ring

A UV light detector was created by patterning a $400 \mu\text{m}^2$ square of zinc oxide nanoparticles between two gold electrodes on a silicon dioxide substrate. Each chip was mounted on a Leaded Chip Carrier (LDDC) by conductive carbon tape (Ted Pella Inc.) and wirebonding was performed between the electrodes of the sensor chip and the electrical pads in the LDDC. Then, the LDDC was inserted to a plastic leaded chip carrier (PLCC) package and the package mounted on an electrical breadboard for subsequent measurements.

6.3. Electrical, Optical Characterization of ZnO Nanoparticle Assemblies

The created ZnO nanoparticle assemblies were characterized using a UV lamp (UVP, UVGL-25) capable of creating UV light at 365 nm and 254 nm with an intensity of 720 and 760 $\mu\text{W}/\text{cm}^2$, respectively, at a distance of 7.6 cm from the light source. A Keithly 2400 Sourcemeter was used to supply a constant voltage and measure the current through the assembly. A constant bias of 20 V was applied to the assembly to ensure a very clear signal to noise ratio of both the short and long wavelength light so the selectivity of the assembly could be adequately characterized. The selectivity of the assembly to the two wavelengths of light was measured by affixing the light source at a distance above the sample to irradiate the sensor with an intensity of 71 mW/cm^2 . The light was repeatedly turned on and off, using both wavelengths of light, and the current through the sensor monitored.

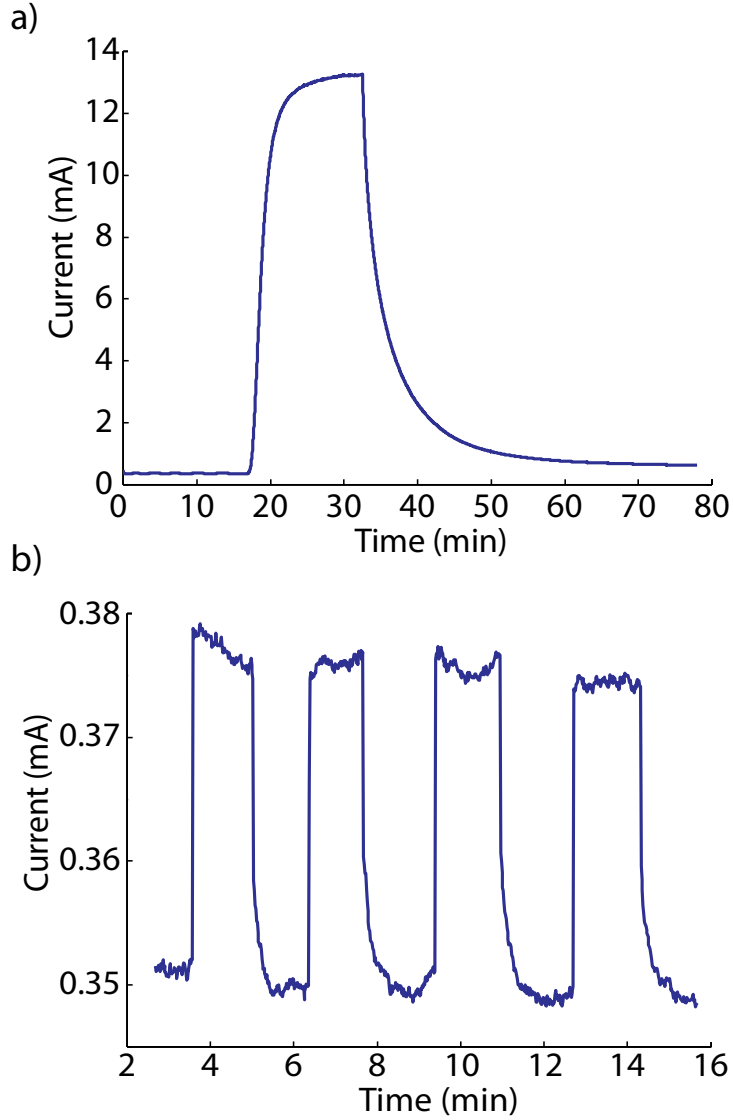


Figure 6.5 a) The current response of the sensor under a constant bias of 20 V when flashing 365 nm light (0-16 mins) and 254 nm light (after 18 mins). b) A close-up view of the 365 nm light response from part a)

The result of this test is shown in Figure 6.5. Assuming that the transient response is caused either by carrier generation and recombination events[36] or a first-order oxidation or reduction reaction[14], the rise can be modeled as an exponential given by

$$I = I_0 \left(1 + \exp \left(-\frac{t}{\tau} \right) \right) \quad (6.1)$$

and the fall by

$$I = I_0 \exp\left(-\frac{t}{\tau}\right) \quad (6.2)$$

where τ is the time constant for the rise or decay. The 365 nm light created a 25 μ A response with a rising time constant of 0.9 s and a falling time constant of 5.8 s. The 254 nm light created a 12.9 mA response with a rising time constant of 93 s and a falling time constant of 244 s. The fast and low-amplitude response to UV light at 365 nm is consistent with lowering of the energy barrier at the Schottky contact caused by promotion of electrons to interface traps by sub-bandgap energy light. Light at 254 nm caused a much slower and larger amplitude response, consistent with creation of electrons in the conduction band and holes in the valence band, reducing adsorbed oxygen on the surface of the semiconductor and lowering the depletion region at the edges of particles causing the bulk resistance of the nanoparticle network to drop.[14,16,37,38] The strength of the signal for the 254 nm wavelength light was more than 500 times greater than that of the 365 nm wavelength light at a similar intensity, showing excellent wavelength selectivity. The sensitivity to various intensities of light at 254 nm wavelength was characterized by varying the distance from the lamp to the assembly. The current through the assembly was plotted as a function of distance, and is given in Figure 6.8. The variation in the intensity of light reaching the assembly is expected to vary as the view factor from the cylindrical light source to the point sensor. Therefore, a curve was fit to the data of the sensor current to the distance of the sensor to the lamp according the equation

$$I = a_1 \left(\frac{1}{x-a_2}\right)^{a_3} \quad (6.3)$$

where I is the current, x is the distance from the light to the assembly, and the fitting parameters a_1 , a_2 and a_3 fit the sensitivity of the assembly, lensing effects from the wavelength filter in front of the lamp, and the non-linearity of the assembly, respectively.[177] Following a least-squares regression, the data and theory curves achieved a coefficient of determination of 0.9999, indicating an excellent fit. The curve fit showed that, for this assembly

$$I \propto P^{0.65} \quad (6.4)$$

where P is the light intensity at the assembly. This power-law relationship and the calculated non-linearity is consistent with similar zinc oxide UV sensors[178], and is due to the dynamics of generation, trapping, and recombination of electrons and holes in the semiconductor material[179].

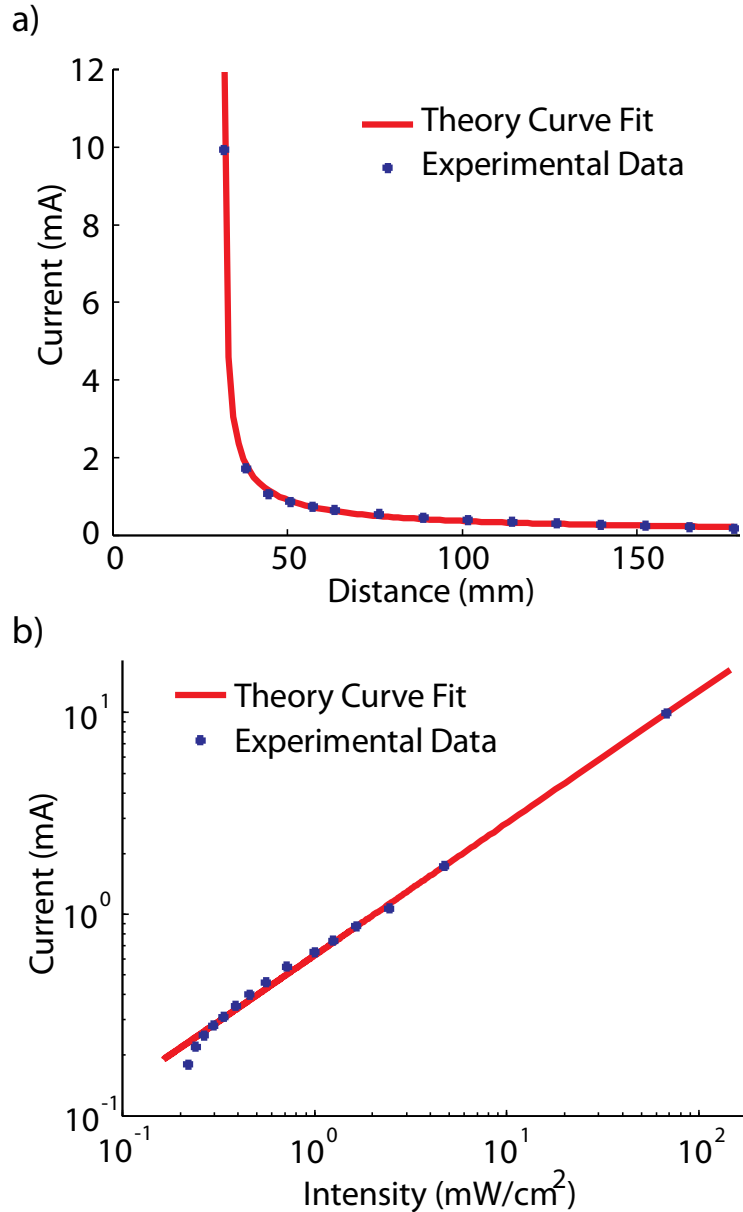


Figure 6.6 The experimental data and theory curve-fit for sensor current as a function of a) physical distance of the sensor from the light source, and b) intensity of light reaching the assembly.

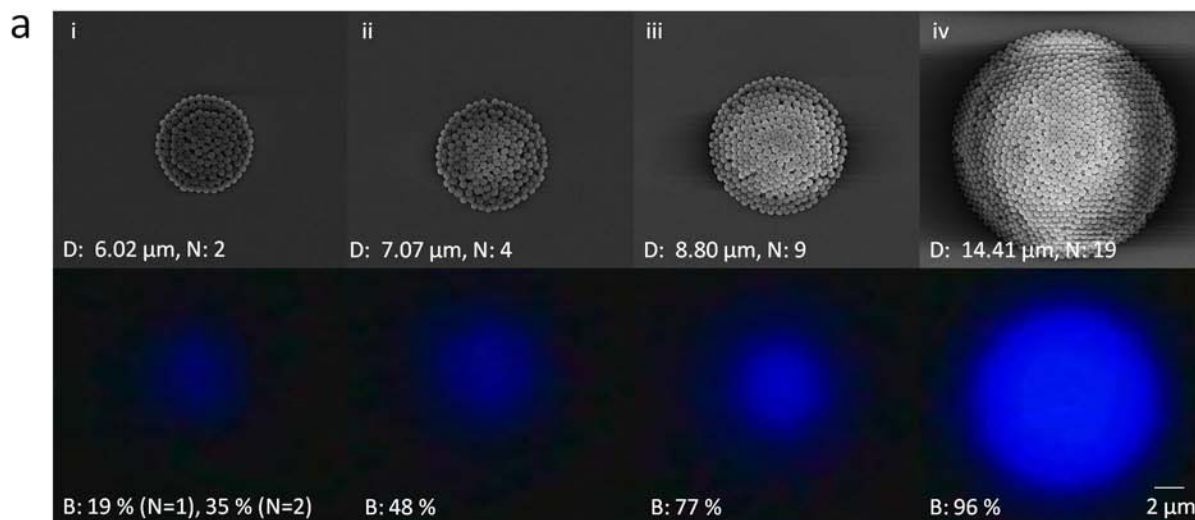
The current was also plotted as a function of incident light intensity, and is shown in Figure 6.6. The sensitivity of the assembly at any given intensity is calculated as the slope of this curve at the given location. An absolute sensitivity (defined as current per unit of incident radiation intensity) of $0.388 \text{ A cm}^2/\text{W}$ was obtained at an intensity of $71 \text{ mW}/\text{cm}^2$, a value less than other similar sensors seen

in the literature, especially considering the higher voltages used in the detection here. However, considering a relative sensitivity independent of geometry (defined as current per unit of radiation energy), a sensitivity of 9.707×10^4 A/W was obtained, a value higher substantially than similar sensors in the literature.[180] The high level of sensitivity in this assembly is believed to be due to the lack of use of any ligands, coatings, or additional solvents in the sensor fabrication. Ligands are often incorporated into UV sensors intentionally to reduce dark current and on-off ratios, but introduction of these ligands may adversely affect sensitivity[179, 181]. Other manufacturing techniques for UV sensors require use of ligands in the solution processing of the nanoparticles, which can be difficult to fully remove after patterning is complete[180]. Remaining ligands could adversely affect the sensor sensitivity, a problem which is absent in the current manufacturing method. The current assembly could therefore achieve comparable or higher absolute sensitivity by increasing the area of the exposed area while maintaining the high quality of fabricated nanoparticle films.

6.4. Study on Size-tunability of Particle Cluster Arrays by Fluorescence Microscopy

Figure 6.7 demonstrated the size-tunability of this printing technology can be used for calibration of fluorescent intensity of fluorescence dye-tagged particle assemblies with respect to concentration of the suspension. Various sizes of polystyrene particle assemblies were printed from different concentrations of polystyrene bead suspension and fluorescence measurement of each assembly was performed. Fluorescence imaging was performed using a Nikon TE 2000 inverted fluorescence microscope. A different filter cube was used for each microparticle to match the emission and excitation wavelengths. The acquired images were overlaid to obtain the final image. Obtained fluorescence images are analyzed by free software, Pixel View (Global Systems Science, Regents of the University of California). Each pixel of the image was dissected into Red, Green, Blue component color intensity (%) by this software. Blue color intensity of the innermost pixel of the images from polystyrene beads with dark blue fluorescence tags

was analyzed to perform calibration the number of polystyrene beads versus blue color intensity.



b

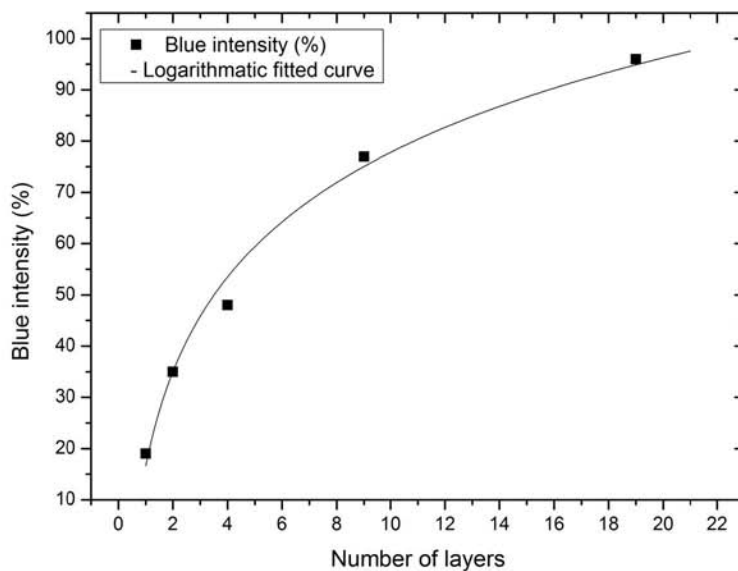


Figure 6.7 Size tunable printing of dark blue (BB, excitation wavelength: 330 nm) fluorescence dye tagged-polystyrene microspheres. a. SEM (upper), fluorescent (lower) views of the printed polystyrene microsphere assemblies. Patterns printed from (i) 0.34 wt% (ii) 0.68 wt% (iii) 1.35 wt% (iv) 2.70 wt% particle concentrations. The number of layers (N) is corresponding to the center of the patterns. For obtaining fluorescence intensity light of N=1 case, the peripheral area of the 0.34 wt% pattern was used. b. A calibration curve of blue fluorescent light versus number of layers. Logarithmic curve is obtained.

It was observed that the number of polystyrene particles was directly correlated with the intensity of the dark blue fluorescence in logarithmic scale. It is consistent with Beer-Lambert law that the amount of radiation absorbed was quantified in a log scale. This capability showed possible application of this printing technology for modulating light intensity of RGB image sensors. Also, accurate calibration of fluorescent intensity versus concentration of any type of biological particles (DNA, protein, cells) with fluorescence tag can be achieved prior to bio-assays and arbitrary fluorescence intensity can be used to quantify the concentration information of targeted species during assay.

6.5. Study on Size-uniformity of Particle Cluster Arrays by SERS Measurement

Size-uniformity of large arrays of gold nanoparticle clusters was thoroughly analyzed by Surface Enhanced Raman Spectroscopy (SERS) measurement. Usually, commercially available metallic nanoparticle suspension contains very low fractions of nanoparticles due to the presence of strong attractive inter-particle forces and high material costs. Typically, SERS measurement is performed on naturally evaporated deposits of metallic nanoparticles. Thickness variation of the deposits is randomly fluctuating because natural evaporation of a suspension droplet does not provide any means to control geometry of the deposits. Also, a large volume of suspension is required to generate thicker deposits for strong signal intensity. With the presented method, high-aspect ratio, gold nanoparticle (diameter: 100 nm) clusters of various sizes (diameter|30 μm , 10 μm , 3.7 μm , 1.75 μm) were printed from low volume suspension (0.5 ~ 1.0 μL) of low particle fraction (5×10^{-4} wt% ~ 5×10^{-2} wt%) with the method that is presented in chapter 4. The printed clusters were immersed in trans-1,2-bis(4-pyridyl)-ethylene (BPE) solution for 2 hours prior to the measurement. The SERS measurements were performed with a Raman setup built around an inverted microscope (Nikon TE2000). A 10x objective lens was used to focus the laser (785 nm, 30 mW) onto

the sample and collect the SERS signal. The collected signal is passed onto a spectrometer (Princeton Instruments, SP2300) for detection.

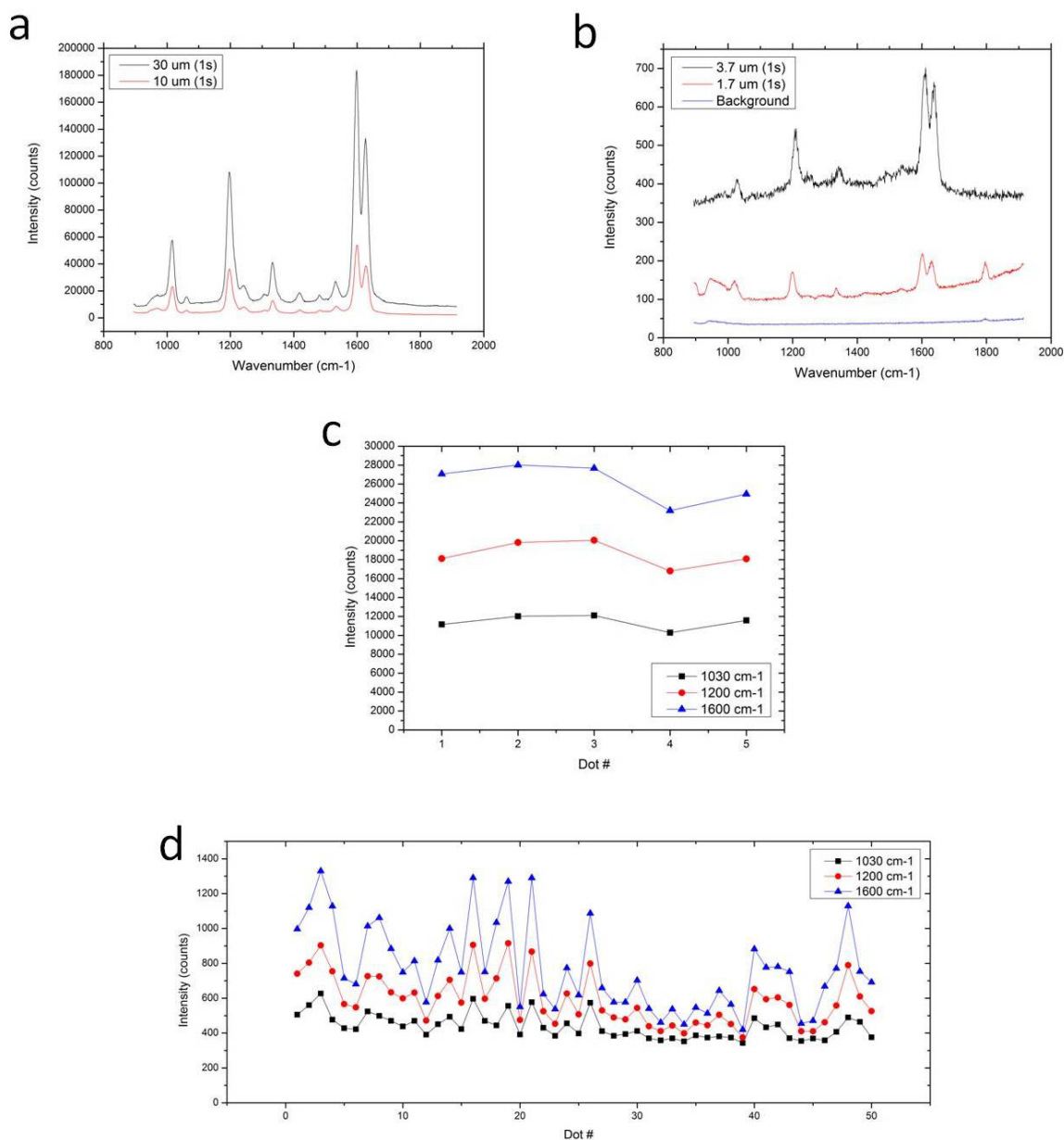


Figure 6.8 Surface Enhanced Raman Spectroscopy (SERS)-spectrum of *trans*-1,2-bis(4-pyridyl)-ethylene (BPE) molecules-absorbed on gold nanoparticle clusters. a. Spectrum from 30 μm and 10 μm diameter gold nanoparticle clusters. b. Spectrum from 3.7 μm and 1.75 μm diameter gold nanoparticle clusters and background substrate. The signal intensity drastically increases as the diameter increases. c-d. SERS signal intensity variation of the high-throughput gold nanoparticle clusters for size-uniformity characterization. c. 5 gold nanoparticle clusters (average diameter: 10 μm). d. 50 gold dots (average diameter: 3.7 μm).

As shown in Figure 6.8, strong, uniform SERS signal was obtained from gold nanoparticle clusters. In Figure 6.8.a-b, the intensity of SERS signal from the cluster was significantly modulated by the small change of cluster size. The magnitude of the order of the signal intensity changed 10^6 times as the diameter scaled up 10 times. The result implies that the intensity of SERS signal from the cluster is a good measure to identify size-uniformity of the cluster arrays. The size-uniformity of the clusters was analyzed by measuring SERS signal of the clusters as presented in Figure 6.6.c-d, The clusters of two different sizes (Diameter|10 μm , 3.7 μm) were used for the measurement. The deviation of the signal is less than 10 % from the measurement on 5 clusters of 10 μm diameter. Also, the measurement on 50 clusters of 3.7 μm diameter shows the deviation was around 10 ~ 30 %. The intensity of SERS signal is roughly proportional to the number of molecules attached to the particle surfaces and the signal is also proportional to the volume of the patterns, which means the signal scales cubically with length of the cluster. This argument leads to the estimates that variation of the cluster diameter is within 7 ~ 8 % in the array. This measurement results show good potential to apply this method to manufacture micro-scale devices in material science with low material consumption.

Table 6.1 Summary of data shown in Figure 6.8.c-d

Wave number (cm^{-1})	3.7 μm diameter patterns (50 dots)		
	Average Intensity (count)	Standard deviation	Uniformity (%)
1030	439	70.9	16.2
1200	591	145	24.6
1600	776	249	32.0
Wave number (cm^{-1})	10 μm diameter patterns (5 dots)		
	Average Intensity (count)	Standard deviation	Uniformity (%)
1030	11428	744	6.51
1200	18577	1350	7.29
1600	26180	2050	7.84

Chapter 7. Conclusion and Future Work

7.1. Conclusion

In this dissertation, three types of mechanical systems for evaporation-driven fast crystallization of 3D micro- and nano-particle assemblies were developed and studied. These mechanical systems are based upon assembly methods: constrained microparticle assembly by open-channel flow, templated micro, nanoparticle assembly by thin-liquid film flow and printed micro, nanoparticle assembly by micro scale evaporative flow. Micro- and nano-particles were chosen as modeling materials to study the crystallizing behavior of particle assemblies because its geometries are easily controllable and the size distribution of the particles is uniform, so that experimental results can be easily interpreted.

In constrained microparticle assembly by open-channel flow, the ultrafast assembly of microparticles was demonstrated by using simple photolithography and the surface-tension-induced capillary action of a microparticle dispersed suspension. High-speed assembly ($< 200 \mu\text{m/s}$) of silica and silica gel microparticles was achieved within a thin and long, open microchannel and this phenomenon was modeled and compared with experimental data. The commensurable effect of assembled particles within the channels was addressed, and self-supported particle-based patterns were fabricated by dissolving the photoresist.

In templated micro, nanoparticle assembly by thin-liquid film flow, patterning of 3D micro, nanoparticle assemblies were created by taking advantage of evaporative self-assembly and the coffee-ring effect of an evaporating droplet of a low concentration suspension. The principle of the technique was analyzed theoretically by the scaling analysis of main parameters of the process and the scaling effect, the effect of the volume, the concentration of the suspension and the effect of surface treatment on the patterning were studied. Based on this method, it was demonstrated that the patterns of 3D crystallized assemblies of various sizes of microparticles (Silica), metal oxide nanoparticles (TiO_2 , ZnO) and metallic nanoparticles (Ag) were successfully generated by low-concentrated particle suspension (1.25 wt % ~ 5 wt %) without additional sintering steps in 5 minute-

scale. It was also shown that the geometries of the patterns can be finely controlled by adjusting the parameters of the process.

In printed micro, nanoparticle assembly by micro scale evaporative flow, a fast method to create high-throughput, size-tunable micro, nanoparticle crystallized clusters was developed by applying evaporative-self assembly to picoliter scale droplets of particle suspension. Formation of the droplets from a nano-fabricated printing head was driven by gravity force and surface tension force of a contacting surface. Fast evaporation (< 10 s) of the droplets on a hydrophobic surface drove the fast, complete clustering of the particles when the particle clustering time was shorter than the evaporation time of the droplet. Based on this method, multiplex printing of various particle clusters was demonstrated with accurate positioning and alignment capability.

Particle assembly behaviors in evaporative self-assembly were studied in-depth based on experimental observation from rapid evaporative self-assembly and computational simulation to interpret the experimental results. Critical parameters for the analysis of colloidal motions in evaporative flows were identified by conventional thermo-coupled fluid mechanics and numerical values of those parameters were accurately calculated by particle-dynamic incorporated-computations to provide accounts for particle effect in evaporative self-assembly. Interpretation of experimental results was aided by numerical simulations to provide the claim that particle-particle interaction mainly drives the onset of the crystallization in evaporative self-assembly of the particles, rather than the evaporation of the liquid medium.

At last, in order to inspire various practical applications of 3D patterns of crystallized micro, nanoparticle assemblies, electrical and optical characterization of the particle assemblies were performed. Zinc oxide|(ZnO) nanoparticle assemblies, polystyrene|(PS) microparticle assemblies and gold|(Au) nanoparticle assemblies were created and characterized by UV light modulation-based I-V measurement, fluorescence measurement and SERS measurement. The characterization results promises that evaporation-driven fast crystallization of 3D micro, nanoparticle assemblies can be applied to rapid, direct characterization of various target species.

From developing new crystallizing methods for rapid crystallization of micro- and nano-particles, through understanding fundamental colloidal sciences by

experimental and computational means, this dissertation concludes with the strong thesis that evaporation-driven fast crystallization of micro-and nano-particles can be applied for rapid, direct characterization of micro, nanoparticle 3D assemblies. Based upon this thesis, several future works are proposed in the next chapter.

7.2. Future Work

It is anticipated that evaporation-driven fast crystallization of 3D micro, nanoparticle assemblies can be potentially used for various applications in micro-and nano-manufacturing, bio-chemical assays and fundamental colloidal science. The detailed proposals are following.

7.2.1. Micro-and Nano-manufacturing

Simplicity of the assembly methods based on evaporation of the liquid medium in this dissertation envisions wide applicability of those methods to various types of particles, substrates for numerous applications such as three-dimensional photonic crystals, circuitry of printed electronics on flexible substrates, conductometric, and plasmonic-based biochemical sensors. Since it offers a convenient way to control the crystallization of micro-and nano-particles with good compatibility with current IC (Integrated Circuits) processes, the methods in dissertation promises its prompt expansion and applicability to modern CMOS-based processing technologies for large-scale MEMS manufacturing. The presented technique will provide a significant means to construct key structures in Bio-MEMS (microelectromechanical systems), chromatography on the micro-scale, 3D photonics and various optical applications.

7.2.2. Bio-chemical assays

Rapid crystallization of analytes such as bacterial-cells, viruses and airborne microorganisms can be achieved by the presented technologies in this dissertation.

Also, rapid, direct measurement of analytes after “crystallization” part can also be performed by electrical and optical means as demonstrated in the dissertation. Novel filtration methods or chromatography methods can be developed by taking advantage of self-assembled microspheres in microfluidic systems for the assay of environmentally hazardous species.

7.2.3. Fundamental Colloidal Science

Good compatibility of the technologies with conventional micro-fabrication technologies can provide an accurately tunable platform to study interesting electrical, optical properties of the particle assembly with micro size apparatus on-chip. Also, real-time monitoring capability of the assembly behaviors in evaporative self-assembly, which was demonstrated in the dissertation, will suggest new revenue to study fundamental colloidal science with many different ways. Studies on particle assembly behaviors in experimental domain with controlled settings will facilitate the understanding of particle assembly behaviors in evaporative self-assembly.

Bibliography

- [1] J. Duan and J. Gregory, Coagulation by hydrolysing metal salts, *Advances in Colloid and Interface Science*, 100:475-502, 2003.
- [2] R. A. Guy, A. Kapoor, J. Holicka, D. Shepherd and P. A. Horgen, A rapid molecular-based assay for direct quantification of viable bacteria in slaughterhouses, *Journal of Food Protection*, 69:1265-1272, 2006.
- [3] A. Hashimoto, S. Kunikane and T. Hirata, Prevalence of *Cryptosporidium* oocysts and *Giardia* cysts in the drinking water supply in Japan, *Water Research*, 36:519-526, 2002.
- [4] W. A. M. Hijnen, D. A. Van Veenendaal, W. M. H. van der Speld, A. Visser, W. Hoogenboezem and D. van der Kooij, Enumeration of faecal indicator bacteria in large water volumes using on site membrane filtration to assess water treatment efficiency, *Water Research*, 34:1659-1665, 2000.
- [5] Y.-C. Hwang, O. M. Leong, W. Chen and M. V. Yates, Comparison of a reporter assay and immunomagnetic separation real-time reverse transcription-PCR for the detection of enteroviruses in seeded environmental water samples, *Applied and Environmental Microbiology*, 73:2338-2340, 2007.
- [6] S. Kamma, L. Tang, K. Leung, E. Ashton, N. Newman and M. R. Suresh, A rapid two dot filter assay for the detection of *E. coli* O157 in water samples, *Journal of Immunological Methods*, 336:159-165, 2008.
- [7] G. Ko, T. L. Cromeans and M. D. Sobsey, UV inactivation of adenovirus type 41 measured by cell culture mRNA RT-PCR, *Water Research*, 39:3643-3649, 2005.

- [8] R. MacDonald and V. S. Brechzel, Community analysis of bacterial biofilms in a simulated recirculating cooling-water system by fluorescent in situ hybridization with rRNA-targeted oligonucleotide probes, *Water Research*, 34:2439-2446, 2000.
- [9] S. Meriç, M. Guida, A. Anselmo, M. Mattei, G. Melluso and G. Pagano, Microbial and cod removal in a municipal wastewater treatment plant using coagulation flocculation process, *Journal of Environmental Science and Health – Part A Toxic/Hazardous Substances and Environmental Engineering*, 37:1483-1494, 2002.
- [10] S. J. Lee, J. S. Park, H. T. Im and H.-I. Jung, A microfluidic ATP-bioluminescence sensor for the detection of airborne microbes, *Sensors and Actuators B: Chemical*, 132:443-448, 2008.
- [11] A. J. Mach and D. Di Carlo, Continuous scalable blood filtration device using inertial microfluidics, *Biotechnology and Bioengineering*, 107:302-311, 2010.
- [12] A. R. McFarland, J. S. Haglund, M. D. King, S. Hu, M. S. Phull, B. W. Moncla and Y. Seo, Wetted Wall Cyclones for Bioaerosol Sampling, *Aerosol Science and Technology*, 44:241-252, 2006.
- [13] H. Moncada-Hernández and B. Lapizco-Encinas, Simultaneous concentration and separation of microorganisms: insulator-based dielectrophoretic approach, *Analytical and Bioanalytical Chemistry*, 396:1805-1816, 2002.
- [14] H.-S. Moon, J.-H. Lee, K. Kwon and H.-I. Jung, Review of Recent Progress in Micro-Systems for the Detection and Analysis of Airborne Microorganisms, *Analytical Letters*, 45:113-129, 2010.
- [15] H.-S. Moon, Y.-W. Nam, J. C. Park and H.-I. Jung, Dielectrophoretic Separation of Airborne Microbes and Dust Particles Using a Microfluidic Channel for Real-Time Bioaerosol Monitoring, *Environmental Science & Technology*, 43:5857-5863, 2009.

- [16] J.-S. Park and H.-I. Jung, Multiorifice Flow Fractionation: Continuous Size-Based Separation of Microspheres Using a Series of Contraction/Expansion Microchannels, *Analytical Chemistry*, 81:8280-8288, 2009.
- [17] J.-S. Park, S.-H. Song and H.-I. Jung, Continuous focusing of microparticles using inertial lift force and vorticity via multi-orifice microfluidic channels, *Lab on a Chip*, 9:2009.
- [18] H. A. Pohl *Dielectrophoresis: The behavior of neutral matter in nonuniform electric fields*, Cambridge : Cambridge University Press, 1978.
- [19] T. Rinsoz, P. Duquenne, G. Greff-Mirguet and A. Oppliger, Application of real-time PCR for total airborne bacterial assessment: Comparison with epifluorescence microscopy and culture-dependent methods, *Atmospheric Environment*, 42:6767-6774, 2008.
- [20] P. Sabounchi, A. Morales, P. Ponce, L. Lee, B. Simmons and R. Davalos, Sample concentration and impedance detection on a microfluidic polymer chip, *Biomedical Microdevices*, 10:661-670, 2008.
- [21] R. K. Saiki, S. Scharf, F. Faloona, K. B. Mullis, G. T. Horn, H. A. Erlich and N. Arnheim, Enzymatic amplification of beta-globin genomic sequences and restriction site analysis for diagnosis of sickle cell anemia, *Science*, 230:1350-1354, 1985.
- [22] M. H. Sawyer, C. J. Chamberlin, Y. N. Wu, N. Aintablian and M. R. Wallace, Detection of Varicella-Zoster Virus DNA in Air Samples from Hospital Rooms, *Journal of Infectious Diseases*, 169:91-94, 1994.
- [23] A. Sengupta, N. Brar and E. J. Davis, Bioaerosol detection and characterization by surface-enhanced Raman spectroscopy, *Journal of Colloid and Interface Science*, 309:36-43, 2007.

- [24] S. Seshadri, T. Han, V. Krumins, D. E. Fennell and G. Mainelis, Application of ATP bioluminescence method to characterize performance of bioaerosol sampling devices, *Journal of Aerosol Science*, 40:113-121, 2009.
- [25] A. E. Sherry, M. F. Patterson, D. Kilpatrick and R. H. Madden, Evaluation of the use of conductimetry for the rapid and precise measurement of *Salmonella* spp. growth rates, *Journal of Microbiological Methods*, 67:86-92, 2006.
- [26] T. S. Sim, K. Kwon, J. C. Park, J.-G. Lee and H.-I. Jung, Multistage-multiorifice flow fractionation (MS-MOFF): continuous size-based separation of microspheres using multiple series of contraction/expansion microchannels, *Lab on a Chip*, 11:2007.
- [27] L. Su, W. Jia, C. Hou and Y. Lei, Microbial biosensors: A review, *Biosensors and Bioelectronics*, 26:1788-1799, 2009.
- [28] J. Suehiro, D. Noutomi, M. Shutou and M. Hara, Selective detection of specific bacteria using dielectrophoretic impedance measurement method combined with an antigen-antibody reaction, *Journal of Electrostatics*, 58:229-246, 2003.
- [29] J. Suehiro, A. Ohtsubo, T. Hatano and M. Hara, Selective detection of bacteria by a dielectrophoretic impedance measurement method using an antibody-immobilized electrode chip, *Sensors and Actuators B: Chemical*, 119:319-326, 2006.
- [30] J. Takagi, M. Yamada, M. Yasuda and M. Seki, Continuous particle separation in a microchannel having asymmetrically arranged multiple branches, *Lab on a Chip*, 5:2005.
- [31] Z. Wu, B. Willing, J. Bjerketorp, J. K. Jansson and K. Hjort, Soft inertial microfluidics for high throughput separation of bacteria from human blood cells, *Lab on a Chip*, 9:2009.

- [32] T. Brenner, T. Glatzel, R. Zengerle and J. Ducree, Frequency-dependent transversal flow control in centrifugal microfluidics, *Lab on a Chip*, 5:2005.
- [33] H. Chen, L. Wang and P. C. H. Li, Nucleic acid microarrays created in the double-spiral format on a circular microfluidic disk, *Lab on a Chip*, 8:2008.
- [34] J. Cole and J. Hansen, Analytical ultracentrifugation as a contemporary biomolecular research tool, *Journal of Biomolecular Techniques*, 10:163-176, 1999.
- [35] D. C. Duffy, H. L. Gillis, J. Lin, N. F. Sheppard and G. J. Kellogg, Microfabricated Centrifugal Microfluidic Systems: Characterization and Multiple Enzymatic Assays, *Analytical Chemistry*, 71:4669-4678, 1999.
- [36] R. Gorkin, J. Park, J. Siegrist, M. Amasia, B. S. Lee, J.-M. Park, J. Kim, H. Kim, M. Madou and Y.-K. Cho, Centrifugal microfluidics for biomedical applications, *Lab on a Chip*, 10:2010.
- [37] S. Haeberle, T. Brenner, R. Zengerle and J. Ducree, Centrifugal extraction of plasma from whole blood on a rotating disk, *Lab on a Chip*, 6:2006.
- [38] R. G. Harrison, P. Todd, S. R. Rudge and D. P. Petrides, *Bioseparations Science and Engineering*, Oxford University Press, 2003.
- [39] N. Honda, U. Lindberg, P. Andersson, S. Hoffmann and H. Takei, Simultaneous Multiple Immunoassays in a Compact Disc-Shaped Microfluidic Device Based on Centrifugal Force, *Clinical Chemistry*, 51:1955-1961, 2005.
- [40] J. Kim, S. Hee Jang, G. Jia, J. V. Zoval, N. A. Da Silva and M. J. Madou, Cell lysis on a microfluidic CD (compact disc), *Lab on a Chip*, 4:2004.
- [41] S. Lai, S. Wang, J. Luo, L. J. Lee, S.-T. Yang and M. J. Madou, Design of a Compact Disk-like Microfluidic Platform for Enzyme-Linked Immunosorbent Assay, *Analytical Chemistry*, 76:1832-1837, 2004.

[42] B. S. Lee, J.-N. Lee, J.-M. Park, J.-G. Lee, S. Kim, Y.-K. Cho and C. Ko, A fully automated immunoassay from whole blood on a disc, *Lab on a Chip*, 9:2009.

[43] B. S. Lee, Y. U. Lee, H.-S. Kim, T.-H. Kim, J. Park, J.-G. Lee, J. Kim, H. Kim, W. G. Lee and Y.-K. Cho, Fully integrated lab-on-a-disc for simultaneous analysis of biochemistry and immunoassay from whole blood, *Lab on a Chip*, 11:2012.

[44] R. Peytavi, F. R. Raymond, D. Gagne, F. J. Picard, G. Jia, J. Zoval, M. Madou, K. Boissinot, M. Boissinot, L. Bissonnette, M. Ouellette and M. G. Bergeron, Microfluidic Device for Rapid (<15 min) Automated Microarray Hybridization, *Clinical Chemistry*, 51:1836-1844, 2005.

[45] L. G. Puckett, E. Dikici, S. Lai, M. Madou, L. G. Bachas and S. Daunert, Investigation into the Applicability of the Centrifugal Microfluidics Platform for the Development of Protein-Ligand Binding Assays Incorporating Enhanced Green Fluorescent Protein as a Fluorescent Reporter, *Analytical Chemistry*, 76:7263-7268, 2004.

[46] J. Siegrist, R. Gorkin, M. Bastien, G. Stewart, R. Peytavi, H. Kido, M. Bergeron and M. Madou, Validation of a centrifugal microfluidic sample lysis and homogenization platform for nucleic acid extraction with clinical samples, *Lab on a Chip*, 10:2010.

[47] J. Steigert, M. Grumann, T. Brenner, L. Riegger, J. Harter, R. Zengerle and J. Ducree, Fully integrated whole blood testing by real-time absorption measurement on a centrifugal platform, *Lab on a Chip*, 6:2006.

[48] S. Choi, I. Park, Z. Hao, H.-y. N. Holman, A. P. Pisano and T. I. Zohdi, Ultrafast Self-Assembly of Microscale Particles by Open-Channel Flow, *Langmuir*, 26:4661-4667, 2010.

[49] S. Choi, S. Stassi, A. P. Pisano and T. I. Zohdi, Coffee-Ring Effect-Based Three Dimensional Patterning of Micro/Nanoparticle Assembly with a Single Droplet, *Langmuir*, 26:11690-11698, 2010.

- [50] A. Jamshidi, S. L. Neale, K. Yu, P. J. Pauzauskie, P. J. Schuck, J. K. Valley, H.-Y. Hsu, A. T. Ohta and M. C. Wu, NanoPen: Dynamic, Low-Power, and Light-Actuated Patterning of Nanoparticles, *Nano Letters*, 9:2921-2925, 2009.
- [51] A. Kamyshny, M. Ben-Moshe, S. Aviezer and S. Magdassi, Ink-Jet Printing of Metallic Nanoparticles and Microemulsions, *Macromolecular Rapid Communications*, 26:281-288, 2005.
- [52] H.-Y. Ko, J. Park, H. Shin and J. Moon, Rapid Self-Assembly of Monodisperse Colloidal Spheres in an Ink-Jet Printed Droplet, *Chemistry of Materials*, 16:4212-4215, 2004.
- [53] T. Kraus, L. Malaquin, H. Schmid, W. Riess, N. D. Spencer and H. Wolf, Nanoparticle printing with single-particle resolution, *Nat Nano*, 2:570-576, 2007.
- [54] T. Leichle, M. Lishchynska, F. Mathieu, J. B. Pourciel, D. Saya and L. Nicu, A Microcantilever-Based Picoliter Droplet Dispenser With Integrated Force Sensors and Electroassisted Deposition Means, *Microelectromechanical Systems, Journal of*, 17:1239-1253, 2008.
- [55] Y. Masuda, T. Itoh and K. Koumoto, Self-Assembly and Micropatterning of Spherical-Particle Assemblies, *Advanced Materials*, 17:841-845, 2005.
- [56] J. Park, J. Moon, H. Shin, D. Wang and M. Park, Direct-write fabrication of colloidal photonic crystal microarrays by ink-jet printing, *Journal of Colloid and Interface Science*, 298:713-719, 2006.
- [57] J.-U. Park, M. Hardy, S. J. Kang, K. Barton, K. Adair, D. k. Mukhopadhyay, C. Y. Lee, M. S. Strano, A. G. Alleyne, J. G. Georgiadis, P. M. Ferreira and J. A. Rogers, High-resolution electrohydrodynamic jet printing, *Nat Mater*, 6:782-789, 2007.
- [58] R. D. Piner, J. Zhu, F. Xu, S. Hong and C. A. Mirkin, "Dip-Pen" Nanolithography, *Science*, 283:661-663, 1999.

- [59] A. Valsesia, T. Leichlé, L.-M. Lacroix, L. Nicu, F. Bretagnol, P. Colpo, F. Rossi and C. Bergaud, Deposition of Nanobead Hexagonal Crystals Using Silicon Microcantilevers, *Small*, 2:1444-1447, 2006.
- [60] Y. Yin, Y. Lu, B. Gates and Y. Xia, Template-Assisted Self-Assembly: A Practical Route to Complex Aggregates of Monodispersed Colloids with Well-Defined Sizes, Shapes, and Structures, *Journal of the American Chemical Society*, 123:8718-8729, 2001.
- [61] A.-P. Hynninen, J. H. J. Thijssen, E. C. M. Vermolen, M. Dijkstra and A. van Blaaderen, Self-assembly route for photonic crystals with a bandgap in the visible region, *Nat Mater*, 6:202-205, 2007.
- [62] J. D. Joannopoulos, P. R. Villeneuve and S. Fan, Photonic crystals: putting a new twist on light, *Nature*, 386:143-149, 1997.
- [63] D. J. Norris, Photonic Crystals: A view of the future, *Nat Mater*, 6:177-178, 2007.
- [64] B. Y. Ahn, E. B. Duoss, M. J. Motala, X. Guo, S.-I. Park, Y. Xiong, J. Yoon, R. G. Nuzzo, J. A. Rogers and J. A. Lewis, Omnidirectional Printing of Flexible, Stretchable, and Spanning Silver Microelectrodes, *Science*, 323:1590-1593, 2009.
- [65] A. L. Briseno, S. C. B. Mannsfeld, M. M. Ling, S. Liu, R. J. Tseng, C. Reese, M. E. Roberts, Y. Yang, F. Wudl and Z. Bao, Patterning organic single-crystal transistor arrays, *Nature*, 444:913-917, 2006.
- [66] W. L. Barnes, A. Dereux and T. W. Ebbesen, Surface plasmon subwavelength optics, *Nature*, 424:824-830, 2003.
- [67] S. Lal, S. Link and N. J. Halas, Nano-optics from sensing to waveguiding, *Nat Photon*, 1:641-648, 2007.

- [68] S. A. Berkowitz and J. S. Philo, Monitoring the homogeneity of adenovirus preparations (a gene therapy delivery system) using analytical ultracentrifugation, *Analytical Biochemistry*, 362:16-37, 2007.
- [69] W. Cao and B. Demeler, Modeling Analytical Ultracentrifugation Experiments with an Adaptive Space-Time Finite Element Solution for Multicomponent Reacting Systems, *Biophysical Journal*, 95:54-65, 2008.
- [70] G. J. Howlett, A. P. Minton and G. Rivas, Analytical ultracentrifugation for the study of protein association and assembly, *Current Opinion in Chemical Biology*, 10:430-436, 2006.
- [71] J. V. Zoval and M. J. Madou, Centrifuge-based fluidic platforms, *Proceedings of the IEEE*, 92:140-153, 2004.
- [72] J. D. Fair and C. M. Kormos, Flash column chromatograms estimated from thin-layer chromatography data, *Journal of Chromatography A*, 1211:49-54, 2008.
- [73] C. G. Horvath, B. A. Preiss and S. R. Lipsky, Fast liquid chromatography. Investigation of operating parameters and the separation of nucleotides on pellicular ion exchangers, *Analytical Chemistry*, 39:1422-1428, 1967.
- [74] S. Lindsay and D. Kealey, *High performance liquid chromatography*, 1987.
- [75] Y. Xiang, Y. Liu and M. L. Lee, Ultrahigh pressure liquid chromatography using elevated temperature, *Journal of Chromatography A*, 1104:198-202, 2006.
- [76] M. Eisenstein, Adventures in the matrix, *Nat Meth*, 3:410-410, 2006.
- [77] D. T. Gjerde and J. S. Fritz, *Ion chromatography*, Wiley-VCH, 2000.
- [78] P. Jackson and P. R. Haddad, *Ion chromatography: principles and applications.*, Elsevier, 1990.

- [79] G. H. Lathe and C. R. J. Ruthven, The separation of substances and estimation of their relative molecular sizes by the use of columns of starch in water, *Biochemical Journal*, 62:665-674, 1956.
- [80] J. Porath and P. E. R. Flodin, Gel Filtration: A Method for Desalting and Group Separation, *Nature*, 183:1657-1659, 1959.
- [81] H. Small, *Ion chromatography*, Plenum Press., 1989.
- [82] A. Striegel, W. W. Yau, J. J. Kirkland and D. D. Bly *Modern Size-Exclusion Liquid Chromatography: Practice of Gel Permeation and Gel Filtration Chromatography, 2nd Edition*, WILEY-VCH, 2009.
- [83] T. Sun, R. R. Chance, W. W. Graessley and D. J. Lohse, A Study of the Separation Principle in Size Exclusion Chromatography, *Macromolecules*, 37:4304-4312, 2004.
- [84] Y. Wang, I. Teraoka, F. Y. Hansen, G. n. H. Peters and O. Hassager, A Theoretical Study of the Separation Principle in Size Exclusion Chromatography, *Macromolecules*, 43:1651-1659, 2010.
- [85] T. Weiss and J. Weiss, *Handbook of Ion Chromatography*, Wiley-VCH, 2005.
- [86] A. S. Dukhin and P. J. Goetz, *Ultrasound for characterizing colloids*, Elsevier, 2002.
- [87] A. H. Gordon, *Electrophoresis of proteins in polyacrylamide and starch gels*, North-Holland Pub. Co., 1975.
- [88] R. J. Hunter, *Foundations of Colloid Science*, Oxford University Press, 2001.
- [89] J. J. Lyklema, *Fundamentals of Interface and Colloid Science*, Elsevier, 1995.

- [90] W. B. Russel, D. A. Saville and W. R. Schowalter, *Colloidal Dispersions*, Cambridge University Press, 1989.
- [91] H. Schagger, Tricine-SDS-PAGE, *Nat. Protocols*, 1:16-22, 2006.
- [92] M. Bier, *Electrophoresis: theory, methods, and applications*, Academic Press, 1967.
- [93] P. Born, S. Blum, A. Munoz and T. Kraus, Role of the Meniscus Shape in Large-Area Convective Particle Assembly, *Langmuir*, 27:8621-8633, 2011.
- [94] N.-G. Cha, Y. Echevoyen, T.-H. Kim, J.-G. Park and A. A. Busnaina, Convective Assembly and Dry Transfer of Nanoparticles Using Hydrophobic/Hydrophilic Monolayer Templates, *Langmuir*, 25:11375-11382, 2009.
- [95] N. Denkov, O. Velev, P. Kralchevski, I. Ivanov, H. Yoshimura and K. Nagayama, Mechanism of formation of two-dimensional crystals from latex particles on substrates, *Langmuir*, 8:3183-3190, 1992.
- [96] N. D. Denkov, O. D. Velev, P. A. Kralchevsky, I. B. Ivanov, H. Yoshimura and K. Nagayama, Two-dimensional crystallization, *Nature*, 361:26-26, 1993.
- [97] A. S. Dimitrov and K. Nagayama, Continuous Convective Assembling of Fine Particles into Two-Dimensional Arrays on Solid Surfaces, *Langmuir*, 12:1303-1311, 1996.
- [98] E. Kim, Y. Xia and G. M. Whitesides, Two- and three-dimensional crystallization of polymeric microspheres by micromolding in capillaries, *Advanced Materials*, 8:245-247, 1996.
- [99] Y. Mino, S. Watanabe and M. T. Miyahara, Fabrication of Colloidal Grid Network by Two-Step Convective Self-Assembly, *Langmuir*, 27:5290-5295, 2011.

[100] E. C. H. Ng, K. M. Chin and C. C. Wong, Controlling Inplane Orientation of a Monolayer Colloidal Crystal by Meniscus Pinning, *Langmuir*, 27:2244-2249, 2011.

[101] NASA Earth Observatory, Salt Ponds in South San Francisco Bay 2002.

[102] G. Khoschror, F. Fruehwirth and S. Zelzer, Isocratic High-Performance Liquid Chromatographic Method with Ultraviolet Detection for Simultaneous Determination of Levels of Voriconazole and Itraconazole and Its Hydroxy Metabolite in Human Serum, *Antimicrobial Agents and Chemotherapy*, 49:3569-3571, 2005.

[103] A. E. Herr, D. J. Throckmorton, A. A. Davenport and A. K. Singh, On-Chip Native Gel Electrophoresis-Based Immunoassays for Tetanus Antibody and Toxin, *Analytical Chemistry*, 77:585-590, 2004.

[104] B. A. Grzybowski, A. Winkleman, J. A. Wiles, Y. Brumer and G. M. Whitesides, Electrostatic self-assembly of macroscopic crystals using contact electrification, *Nat Mater*, 2:241-245, 2003.

[105] P. V. Braun and P. Wiltzius, Microporous materials: Electrochemically grown photonic crystals, *Nature*, 402:603-604, 1999.

[106] A. Walcarius, E. Sibottier, M. Etienne and J. Ghanbaja, Electrochemically assisted self-assembly of mesoporous silica thin films, *Nat Mater*, 6:602-608, 2007.

[107] C. D. Dushkin, H. Yoshimura and K. Nagayama, Nucleation and growth of two-dimensional colloidal crystals, *Chemical Physics Letters*, 204:455-460, 1993.

[108] M. Fialkowski, A. Bitner and B. A. Grzybowski, Self-assembly of polymeric microspheres of complex internal structures, *Nat Mater*, 4:93-97, 2005.

[109] S. E. Chung, W. Park, S. Shin, S. A. Lee and S. Kwon, Guided and fluidic self-assembly of microstructures using railed microfluidic channels, *Nat Mater*, 7:581-587, 2008.

- [110] N. Bowden, A. Terfort, J. Carbeck and G. M. Whitesides, Self-Assembly of Mesoscale Objects into Ordered Two-Dimensional Arrays, *Science*, 276:233-235, 1997.
- [111] R. K. Golding, P. C. Lewis, E. Kumacheva, M. Allard and E. H. Sargent, In Situ Study of Colloid Crystallization in Constrained Geometry, *Langmuir*, 20:1414-1419, 2003.
- [112] G. Su, Q. Guo and R. E. Palmer, Colloidal Lines and Strings, *Langmuir*, 19:9669-9671, 2003.
- [113] M. Yamaki, J. Higo and K. Nagayama, Size-Dependent Separation of Colloidal Particles In Two-Dimensional Convective Self-Assembly, *Langmuir*, 11:2975-2978, 1995.
- [114] W. Ryu, Z. Huang, J. Sun Park, J. Moseley, A. R. Grossman, R. J. Fasching and F. B. Prinz, Open micro-fluidic system for atomic force microscopy-guided in situ electrochemical probing of a single cell, *Lab on a Chip*, 8:1460-1467, 2008.
- [115] S. K. Sainis, J. W. Merrill and E. R. Dufresne, Electrostatic Interactions of Colloidal Particles at Vanishing Ionic Strength, *Langmuir*, 24:13334-13337, 2008.
- [116] K. Aoki, D. Guimard, M. Nishioka, M. Nomura, S. Iwamoto and Y. Arakawa, Coupling of quantum-dot light emission with a three-dimensional photonic-crystal nanocavity, *Nat Photon*, 2:688-692, 2008.
- [117] D. Graham-Rowe, From dots to devices, *Nat Photon*, 3:307-309, 2009.
- [118] S. Noda and M. Fujita, Light-emitting diodes: Photonic crystal efficiency boost, *Nat Photon*, 3:129-130, 2009.
- [119] F. Fan and K. J. Stebe, Assembly of Colloidal Particles by Evaporation on Surfaces with Patterned Hydrophobicity, *Langmuir*, 20:3062-3067, 2004.

[120] M. H. Lu and Y. Zhang, Microbead Patterning on Porous Films with Ordered Arrays of Pores, *Advanced Materials*, 18:3094-3098, 2006.

[121] D. Qin, Y. Xia, B. Xu, H. Yang, C. Zhu and G. M. Whitesides, Fabrication of Ordered Two-Dimensional Arrays of Micro- and Nanoparticles Using Patterned Self-Assembled Monolayers as Templates, *Advanced Materials*, 11:1433-1437, 1999.

[122] I. Park, S. H. Ko, H. Pan, C. P. Grigoropoulos, A. P. Pisano, J. M. J. Fréchet, E. S. Lee and J. H. Jeong, Nanoscale Patterning and Electronics on Flexible Substrate by Direct Nanoimprinting of Metallic Nanoparticles, *Advanced Materials*, 20:489-496, 2008.

[123] H. Miguez, S. M. Yang and G. A. Ozin, Colloidal photonic crystal microchannel array with periodically modulated thickness, *Applied Physics Letters*, 81:2493-2495, 2002.

[124] H. Miguez, S. M. Yang and G. A. Ozin, Optical Properties of Colloidal Photonic Crystals Confined in Rectangular Microchannels, *Langmuir*, 19:3479-3485, 2003.

[125] E. Rabani, D. R. Reichman, P. L. Geissler and L. E. Brus, Drying-mediated self-assembly of nanoparticles, *Nature*, 426:271-274, 2003.

[126] X. Xiong, P. Makaram, A. Busnaina, K. Bakhtari, S. Somu, N. McGruer and J. Park, Large scale directed assembly of nanoparticles using nanotrench templates, *Applied Physics Letters*, 89:193108-193103, 2006.

[127] S. M. Yang, H. Míguez and G. A. Ozin, Opal Circuits of Light—Planarized Microphotonic Crystal Chips, *Advanced Functional Materials*, 12:425-431, 2002.

[128] E. Adachi, A. S. Dimitrov and K. Nagayama, Stripe Patterns Formed on a Glass Surface during Droplet Evaporation, *Langmuir*, 11:1057-1060, 1995.

- [129] R. D. Deegan, Pattern formation in drying drops, *Physical Review E*, 61:475, 2000.
- [130] R. D. Deegan, O. Bakajin, T. F. Dupont, G. Huber, S. R. Nagel and T. A. Witten, Capillary flow as the cause of ring stains from dried liquid drops, *Nature*, 389:827-829, 1997.
- [131] B. J. Fischer, Particle Convection in an Evaporating Colloidal Droplet, *Langmuir*, 18:60-67, 2001.
- [132] H. Fudouzi and Y. Xia, Colloidal Crystals with Tunable Colors and Their Use as Photonic Papers, *Langmuir*, 19:9653-9660, 2003.
- [133] B. T. Holland, C. F. Blanford, T. Do and A. Stein, Synthesis of Highly Ordered, Three-Dimensional, Macroporous Structures of Amorphous or Crystalline Inorganic Oxides, Phosphates, and Hybrid Composites, *Chemistry of Materials*, 11:795-805, 1999.
- [134] H. Hu and R. G. Larson, Analysis of the Microfluid Flow in an Evaporating Sessile Droplet, *Langmuir*, 21:3963-3971, 2005.
- [135] H. Hu and R. G. Larson, Marangoni Effect Reverses Coffee-Ring Depositions, *The Journal of Physical Chemistry B*, 110:7090-7094, 2006.
- [136] D. M. Kuncicky, B. G. Prevo and O. D. Velev, Controlled assembly of SERS substrates templated by colloidal crystal films, *Journal of Materials Chemistry*, 16:1207-1211, 2006.
- [137] S. I. Matsushita, Y. Yagi, T. Miwa, D. A. Tryk, T. Koda and A. Fujishima, Light Propagation in Composite Two-Dimensional Arrays of Polystyrene Spherical Particles, *Langmuir*, 16:636-642, 1999.
- [138] M. Miyaki, K. Fujimoto and H. Kawaguchi, Cell response to micropatterned surfaces produced with polymeric microspheres, *Colloids and Surfaces A: Physicochemical and Engineering Aspects*, 153:603-608, 1999.

- [139] B. G. Prevo, E. W. Hon and O. D. Velev, Assembly and characterization of colloid-based antireflective coatings on multicrystalline silicon solar cells, *Journal of Materials Chemistry*, 17:791-799, 2007.
- [140] L. W. Schwartz and D. E. Weidner, Modeling of coating flows on curved surfaces, *Journal of Engineering Mathematics*, 29:91-103-103, 1995.
- [141] O. D. Velev, P. M. Tessier, A. M. Lenhoff and E. W. Kaler, Materials: A class of porous metallic nanostructures, *Nature*, 401:548-548, 1999.
- [142] D. Wakuda, M. Hatamura and K. Suganuma, Novel method for room temperature sintering of Ag nanoparticle paste in air, *Chemical Physics Letters*, 441:305-308, 2007.
- [143] Y. Yin, Y. Lu, B. Gates and Y. Xia, Template-Assisted Self-Assembly: A Practical Route to Complex Aggregates of Monodispersed Colloids with Well-Defined Sizes, Shapes, and Structures, *Journal of the American Chemical Society*, 123:8718-8729, 2001.
- [144] H. Sirringhaus, T. Kawase, R. H. Friend, T. Shimoda, M. Inbasekaran, W. Wu and E. P. Woo, High-Resolution Inkjet Printing of All-Polymer Transistor Circuits, *Science*, 290:2123-2126, 2000.
- [145] B. Derby, Inkjet Printing of Functional and Structural Materials: Fluid Property Requirements, Feature Stability, and Resolution, *Annual Review of Materials Research*, 40:395-414,
- [146] J. Stringer and B. Derby, Limits to feature size and resolution in ink jet printing, *Journal of the European Ceramic Society*, 29:913-918, 2009.
- [147] S. Choi, A. Jamshidi, T. J. Seok, M. C. Wu, T. I. Zohdi and A. P. Pisano, Fast, High-Throughput Creation of Size-Tunable Micro/Nanoparticle Clusters via Evaporative Self-Assembly in Picoliter-Scale Droplets of Particle Suspension, *Langmuir*, 28:3102-3111, 2012.

[148] R. Mukhopadhyay, O. Al-Hanbali, S. Pillai, A. G. Hemmersam, R. L. Meyer, A. C. Hunter, K. J. Rutt, F. Besenbacher, S. M. Moghimi and P. Kingshott, Ordering of Binary Polymeric Nanoparticles on Hydrophobic Surfaces Assembled from Low Volume Fraction Dispersions, *Journal of the American Chemical Society*, 129:13390-13391, 2007.

[149] V. Kitaev and G. A. Ozin, Self-Assembled Surface Patterns of Binary Colloidal Crystals, *Advanced Materials*, 15:75-78, 2003.

[150] H. Bodiguel, F. d. r. Doumenc and B. a. Guerrier, Stick-Slip Patterning at Low Capillary Numbers for an Evaporating Colloidal Suspension, *Langmuir*, 26:10758-10763, 2010.

[151] K. Uno, K. Hayashi, T. Hayashi, K. Ito and H. Kitano, Particle adsorption in evaporating droplets of polymer latex dispersions on hydrophilic and hydrophobic surfaces, *Colloid & Polymer Science*, 276:810-815, 1998.

[152] O. A. Soboleva and B. D. Summ, The Kinetics of Dewetting of Hydrophobic Surfaces during the Evaporation of Surfactant Solution Drops, *Colloid Journal*, 65:89-93, 2003.

[153] J. Xu, J. Xia and Z. Lin, Evaporation-Induced Self-Assembly of Nanoparticles from a Sphere-on-Flat Geometry, *Angewandte Chemie International Edition*, 46:1860-1863, 2007.

[154] W. Han, M. Byun and Z. Lin, Assembling and positioning latex nanoparticles via controlled evaporative self-assembly, *Journal of Materials Chemistry*, 21:16968-16972, 2011.

[155] N. J. Suematsu, Y. Ogawa, Y. Yamamoto and T. Yamaguchi, Dewetting self-assembly of nanoparticles into hexagonal array of nanorings, *Journal of Colloid and Interface Science*, 310:648-652, 2007.

[156] S. Andrew, Dewetting-mediated pattern formation in nanoparticle assemblies, *Journal of Physics: Condensed Matter*, 23:083001,

- [157] C. P. Martin, M. O. Blunt, E. Pauliac-Vaujour, A. Stannard, P. Moriarty, I. Vancea and U. Thiele, Controlling Pattern Formation in Nanoparticle Assemblies via Directed Solvent Dewetting, *Physical Review Letters*, 99:116103, 2007.
- [158] G. McHale, S. Aqil, N. J. Shirtcliffe, M. I. Newton and H. Y. Erbil, Analysis of Droplet Evaporation on a Superhydrophobic Surface, *Langmuir*, 21:11053-11060, 2005.
- [159] J. Arcamone, E. Dujardin, G. Rius, F. Perez-Murano and T. Ondarcuhu, Evaporation of Femtoliter Sessile Droplets Monitored with Nanomechanical Mass Sensors, *The Journal of Physical Chemistry B*, 111:13020-13027, 2007.
- [160] P. A. Kralchevsky and N. D. Denkov, Capillary forces and structuring in layers of colloid particles, *Current Opinion in Colloid & Interface Science*, 6:383-401, 2001.
- [161] P. A. Kralchevsky and K. Nagayama, Capillary interactions between particles bound to interfaces, liquid films and biomembranes, *Advances in Colloid and Interface Science*, 85:145-192, 2000.
- [162] T. Zohdi, On the Dynamics of Charged Electromagnetic Particulate Jets, *Archives of Computational Methods in Engineering*, 17:109-135, 2010.
- [163] A. Donev, S. Torquato and F. H. Stillinger, Neighbor list collision-driven molecular dynamics simulation for nonspherical hard particles. I. Algorithmic details, *Journal of Computational Physics*, 202:737-764, 2005.
- [164] J. Duran, *Sands, powders and grains. An introduction to the physics of Granular Matter.*, Springer Verlag., 1997.
- [165] T. a. S. Poschel, T, *Computational granular dynamics*, Springer Verlag., 2004.
- [166] T. I. Zohdi, *Dynamics of charged particulate systems. Modeling, theory and computation.* Springer-Verlag, in press.

- [167] V. N. Truskett and K. J. Stebe, Influence of Surfactants on an Evaporating Drop: Fluorescence Images and Particle Deposition Patterns, *Langmuir*, 19:8271-8279, 2003.
- [168] H. B. Eral, D. M. Augustine, M. H. G. Duits and F. Mugele, Suppressing the coffee stain effect: how to control colloidal self-assembly in evaporating drops using electrowetting, *Soft Matter*, 7:2011.
- [169] X. Shen, C.-M. Ho and T.-S. Wong, Minimal Size of Coffee Ring Structure, *The Journal of Physical Chemistry B*, 114:5269-5274, 2010.
- [170] B. M. Weon and J. H. Je, Capillary force repels coffee-ring effect, *Physical Review E*, 82:015305, 2010.
- [171] Y. Cai and B.-m. Zhang Newby, Marangoni Flow-Induced Self-Assembly of Hexagonal and Stripelike Nanoparticle Patterns, *Journal of the American Chemical Society*, 130:6076-6077, 2008.
- [172] J. Xu, J. Xia, S. W. Hong, Z. Lin, F. Qiu and Y. Yang, Self-Assembly of Gradient Concentric Rings via Solvent Evaporation from a Capillary Bridge, *Physical Review Letters*, 96:066104, 2006.
- [173] R. Bhardwaj, X. Fang, P. Somasundaran and D. Attinger, Self-Assembly of Colloidal Particles from Evaporating Droplets: Role of DLVO Interactions and Proposition of a Phase Diagram, *Langmuir*, 26:7833-7842, 2010.
- [174] G. Yosef and E. Rabani, Self-Assembly of Nanoparticles into Rings: A Lattice-Gas Model, *The Journal of Physical Chemistry B*, 110:20965-20972, 2006.
- [175] O. Kletenik-Edelman, E. Ploshnik, A. Salant, R. Shenhar, U. Banin and E. Rabani, Drying-Mediated Hierarchical Self-Assembly of Nanoparticles: A Dynamical Coarse-Grained Approach, *The Journal of Physical Chemistry C*, 112:4498-4506, 2008.

[176] M. T. Demko, S. Choi, T. I. Zohdi and A. P. Pisano, High resolution patterning of nanoparticles by evaporative self-assembly enabled by in situ creation and mechanical lift-off of a polymer template, *Applied Physics Letters*, 99:253102-253103, 2011.

[177] F. P. Incropera and D. P. Dewitt, *Introduction to Heat Transfer, Third Edition*, Wiley, 1996.

[178] H. Kind, H. Yan, B. Messer, M. Law and P. Yang, Nanowire Ultraviolet Photodetectors and Optical Switches, *Advanced Materials*, 14:158-160, 2002.

[179] Q. Liqiao, C. Shing and S. Sawyer, Metal-Semiconductor-Metal Ultraviolet Photodetectors Based on Zinc-Oxide Colloidal Nanoparticles, *Electron Device Letters, IEEE*, 32:51-53, 2011.

[180] Y. Jin, J. Wang, B. Sun, J. C. Blakesley and N. C. Greenham, Solution-Processed Ultraviolet Photodetectors Based on Colloidal ZnO Nanoparticles, *Nano Letters*, 8:1649-1653, 2008.

[181] Q. Liqiao, C. Shing and S. Sawyer, Low-Pass and Bandpass Alternative Ultraviolet Photoconductor Based on Zinc Oxide Nanoparticles on Intrinsic Gallium Nitride-Based Substrate, *Photonics Technology Letters, IEEE*, 23:414-416, 2010.

[182] R. Roscoe, The viscosity of suspensions of rigid spheres, *British Journal of Applied Physics*, 3:267, 1952.

Appendix A. Supporting Information for Chapter 3

A.1. Relationship between Volume of Suspension and Nature of Particle Deposition

As shown in Figure A.1, the particles on the resist and the ones inside the trenches were clearly separated, which enabled an effective lift-off in all concentrations. As the concentration increased, the trenches were packed more completely. In the lower concentrations, the ring structures were formed.

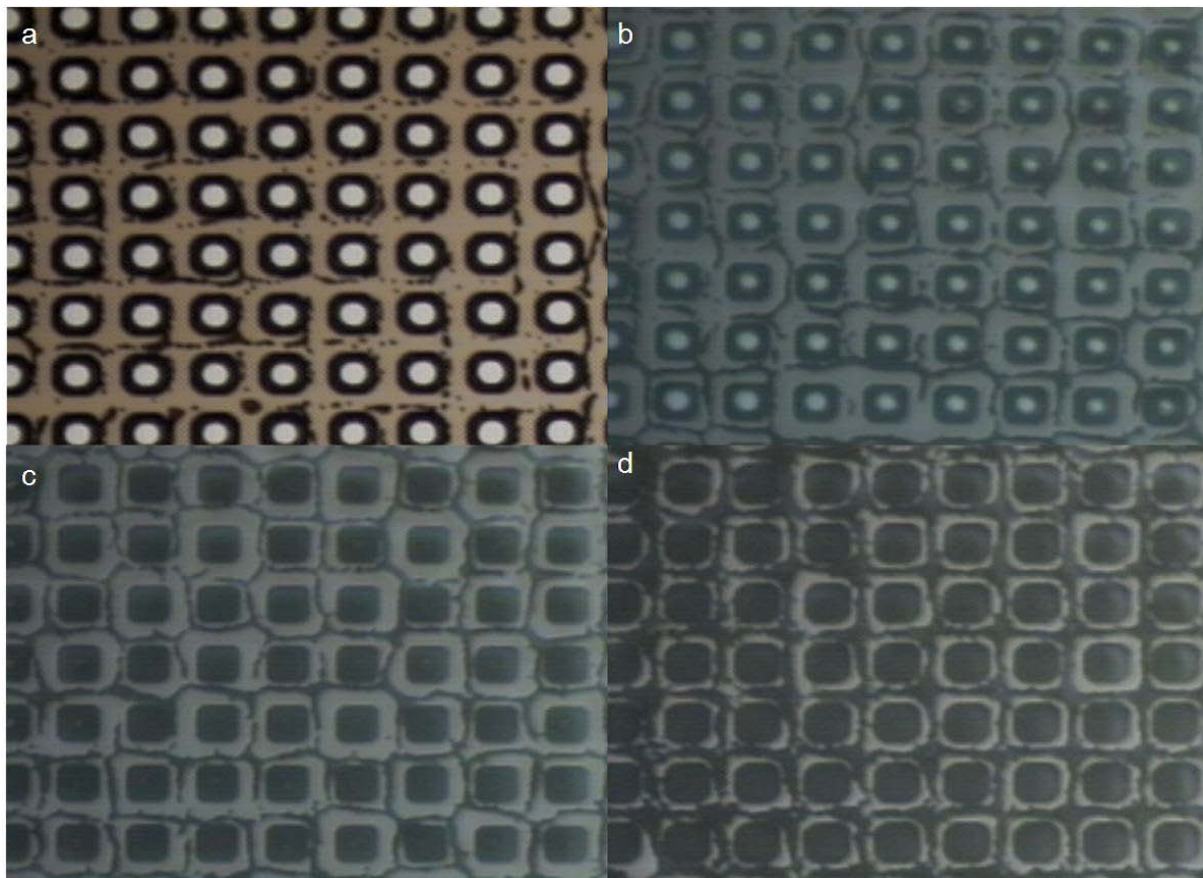


Figure A.1 The nature of particle deposition with respect to different concentrations of the suspension. a-d, (a) 0.3125 wt % (b) 0.625 wt % (c) 1.25 wt %

A.2. Images of 3 μm Silica Microspheres-based Structures after Lift-off

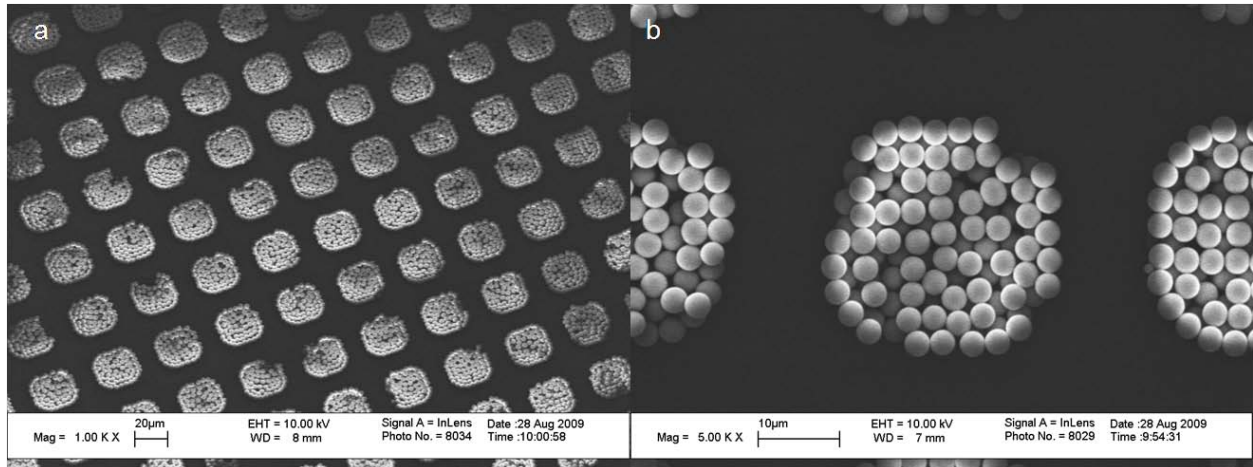


Figure A.2 The images of 3 μm silica microspheres based structures (a) Overall view (b) Close view

A.3. Calculation of Scaling Analysis

The spherical shell model was assumed to calculate the height of droplet at given contact angle. The diameter of the droplet and the contact angle of droplet were measured by the optical microscope.

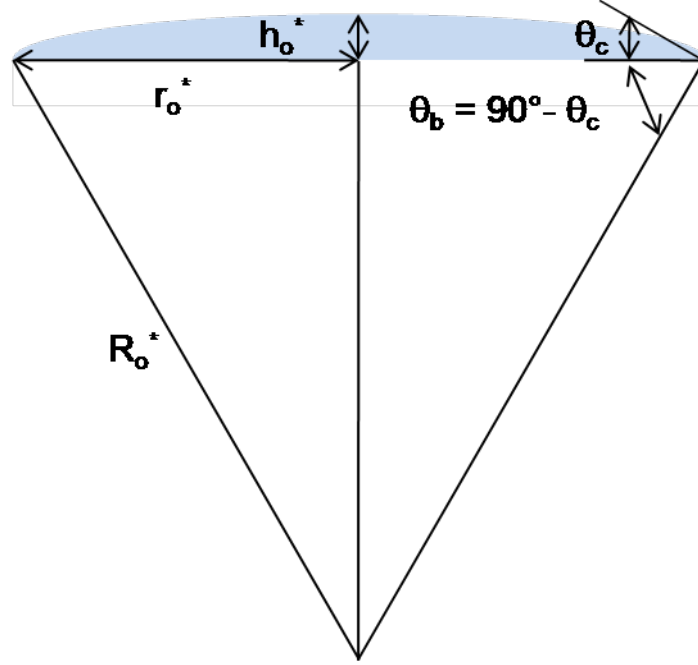


Figure A.3 The notations for the parameters of the droplet

The radius of the spherical shell, R_o^* is calculated as $\sqrt{\frac{r_o^*}{1 - \sin^2 \theta_b}}$, thus, the height of the spherical shell, h_o^* is $R_o^* - \sqrt{R_o^{*2} - r_o^{*2}}$. The parameters of the process, the width of the pattern w^* , the height of the pattern h_o^* and the contact angle θ_c are $20 \mu\text{m}$, $10 \mu\text{m}$ and 10° respectively and are inputted to the calculation. The parameters such as the density of the suspension, ρ^* , the viscosity of the suspension, μ^* are the functions of the fraction of solutes in the suspension and this fraction increases with time as the evaporation of the medium proceeds. In this analysis, it was estimated the range of the viscosity of the suspension based on Roscoe's model[182], $\eta_r = (1 - 1.35 c)^{-2.5}$, where η_r is the dimensionless form of relative viscosity to bulk viscosity and c is the weight fraction of the solutes in the suspension. The density of the suspension was simply computed by multiplying the density of silica particles, the medium to the fractions of each of them and combining those two multiplied values. The density of the water is 1000 kg m^{-3} , the density of the particle (silica in this case) is 2200 kg m^{-3} and the viscosity of the suspension with no solute is $1.002 \times 10^{-3} \text{ kg s}^{-1} \text{ m}^{-1}$. The scale of the global pressure, P_l^* is $\frac{p_c^*}{Ca}$ and the scale of the local pressure is the larger one of either $\frac{\sigma^*}{R^*}$

or $\sigma^* h_0^*$. The scale of the local pressure, $P_2^* (= \frac{\sigma^*}{R^*})$ chosen to be $\frac{\sigma^*}{R^*}$ since $\frac{1}{R^*} > h_0^*$. Therefore, $\frac{P_2^*}{P_1^*} \approx \frac{r_0^{*2}}{w^* h_0^*} \cong 1.14 \times 10^3 \gg 1$. The global time t_1^* can be scaled as the larger one of either $Ca t_c^*$ or $\frac{t_c^*}{E}$ and the scale of local time t_2^* can be scaled as the larger one of either T^* or $\frac{T^*}{M}$. The scale of the global time t_1^* was chosen to be $\frac{t_c^*}{E}$ because $Ca < \frac{1}{E}$ and the scale of the local time t_2^* was chosen to be T^* because $1 > \frac{1}{M}$. Therefore, $\frac{t_2^*}{t_1^*} \approx \frac{3k^* \Delta T^* u_c^* w^{*4}}{\sigma h_0^{*4} L^*} = \frac{3k^* \Delta T^* w^{*4}}{\sigma h_0^{*5} L^*} \left(\frac{\mu^*}{\rho^*} \right) = 0.00308 \left(\frac{\mu^*}{\rho^*} \right)$. While $\frac{P_2^*}{P_1^*}$ has no dependence of the concentration of the solutes, $\frac{t_2^*}{t_1^*}$ was dependent on the concentration due to $\frac{\mu^*}{\rho^*}$ term. $\frac{\mu^*}{\rho^*}$ can be expressed as $\frac{\mu_0^* (1-1.35c)^{-2.5}}{\rho_{\text{water}}(1-c) + \rho_{\text{silica}}c}$ from equations above and the range of $\frac{\mu^*}{\rho^*}$ as $1.002 \times 10^{-6} \leq \frac{\mu^*}{\rho^*} \leq 0.115$ when $0 \leq c \leq 0.740$ (close packing condition), thus, $3.08 \times 10^{-9} \leq \frac{t_2^*}{t_1^*} \leq 3.54 \times 10^{-4} \ll 1$. Therefore, $\frac{P_2^*}{P_1^*} \gg 1$ and $\frac{t_2^*}{t_1^*} \ll 1$. Also, the time scale of diffusion, $t_3 \approx \frac{x^2}{D}$, can be computed by inputting the height of the trench, $10 \mu\text{m}$ and diffusion coefficient of titanium nanoparticle (size $\sim 50 \text{ nm}$) which is an order of $10^{-11} \text{ m}^2/\text{s}$. Then, $\frac{t_2^*}{t_3^*} \approx 10^{-10} \ll 1$.

A.4. Calculations of Packing Volume Ratio

SEM images of the particle packed, trenches were taken in every experiment conducted for obtaining Figure 3.7. The trench patterns used for the experiment were SU-8-based photopatterned substrate with an additional hardbake process. In the analysis of images, the number of particles was counted if every particle was revealed in the image. If the particles inside the trenches were not completely visualized by images, then, hexagonal closed-packing was assumed and the packing volume was estimated based on geometrical models. The maximum number of particles for packing was calculated based on the maximum packing

density, 0.740 which can be achieved in ideal hexagonal closed-packing or face centered-packing cases. Since the number of the samples used for sampling is not sufficient, the error bar was not included in the Figure 3.7.

A.5. Correlation between Evaporation Time and (Length-scale)²

In chapter 3, it was claimed that the evaporation time of the droplet is proportional to (Length-scale)². The experiments of drying droplets of four different length-scales were performed in order to verify the correlation. Evaporative rate per unit area was assumed to be proportional to $\frac{1}{h_o^*}$ according to the assumption in the literature³⁴. Then, overall evaporative rate of the droplet is proportional to $\frac{\pi r_o^{*2}}{h_o^*}$. Therefore, it was roughly assumed that the evaporation time is proportional to V^* (the volume of the suspension) / $(\frac{\pi r_o^{*2}}{h_o^*})$ and its length-scale is L^{*2} . It was also observed that the measured evaporation time correlated with L^{*2} well as shown in Figure A.4.

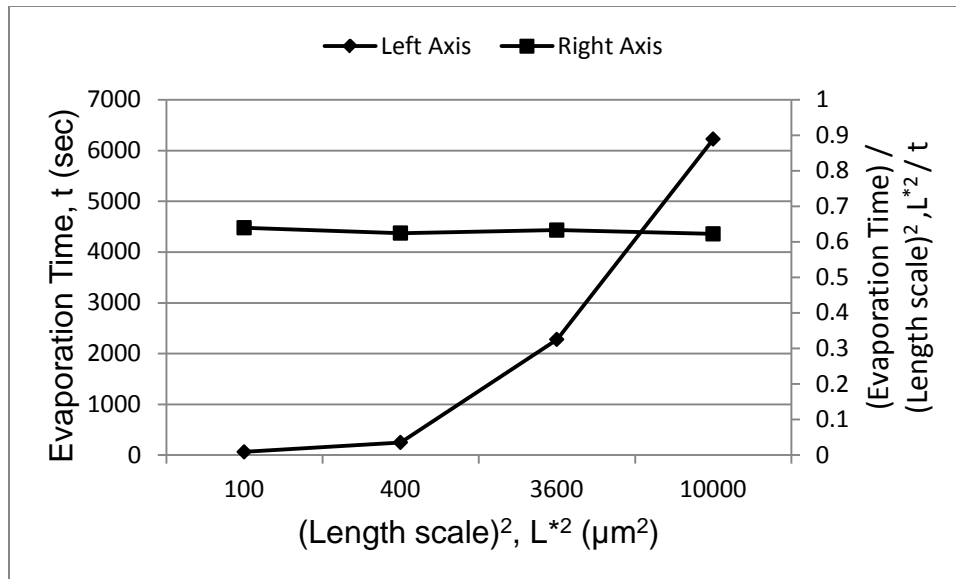


Figure A.4. The graph for the trend of evaporation time with respect to the length scale of the experiment

Appendix B. Supporting Information for Chapter 4

B.1. Calculations for Scaling Analysis

Weber number, $We = \frac{\rho V^2 D}{\sigma} = \frac{\text{(Inertia effect)}}{\text{(Surface tension force)}}$ where ρ is a density of the solvent, V is a characteristic velocity of the fluid inside the pore, D is a diameter of the pore and σ is a surface tension of the solvent was calculated by defining characteristic velocity of the fluid inside the pore. Uni-directional flow of a closed channel with circular cross section was assumed in the micro-pore and Navier-stokes equations with no-slip boundary conditions were applied to estimate characteristic velocity, $V = \frac{\rho g D^2}{16\mu}$ where ρ is a density of a solvent, g is a gravity acceleration, D is a width of the global droplet and μ is a viscosity of the solvent. Assuming low volume fractions of particles does not affect global properties of the solvent, the properties of water at room temperature were used for calculation. $\rho = 997 \text{ kg / m}^3$, $\mu = 1.002 \times 10^{-3}$. $g = 9.8 \text{ m/s}^2$, $D = 20 \text{ }\mu\text{m}$, $200 \text{ }\mu\text{m}$ were used to estimate capillary number. For calculation of Bond number, $Bo = \frac{\rho g L^2}{\sigma}$ where σ

is a surface tension of the solvent and L is a characteristic length of a global droplet, the surface tension of water at room temperature was used and a characteristic length of a global droplet was set to the height of the droplet in the reservoir of the printing head. $\sigma = 7.2 \times 10^{-3}$, $L = 2 \text{ mm}$ for before flattening meniscus of the suspension, $200 \text{ }\mu\text{m}$ for after flattening of the suspension. Also, the characteristic pressure loss across the membrane, P_{loss} is equivalent to $\left(\frac{1}{2} \rho V^2\right) f \left(\frac{2\pi D \Delta L}{\pi D^2}\right)$ where f is a friction factor of the membrane and ΔL is a thickness of the membrane. For $10 \text{ }\mu\text{m}$ thickness, P_{loss} was calculated to be on the order of 10^{-1} Pa while it is 10^{-3} Pa for 100 nm thickness membrane.

B.2. Calculations of Enhancement Factor in SERS Measurement

Enhancement factor of SERS signal from the sample was defined to be $(I_{\text{SERS}} / N_{\text{SERS}}) / (I_{\text{NEAT}} / N_{\text{NEAT}})$ where I_{SERS} is the intensity of SERS signal from the sample at 1 second laser exposure (unit: counts / sec.), N_{SERS} is the number of detection target molecules attached to gold nanoparticles in the sample, I_{NEAT} is the intensity of SERS signal from the base line sample at 1 second laser exposure (unit: counts / sec.) and N_{NEAT} is the number of detection target molecules attached to gold nanoparticles in the base line sample. As a reference, I_{NEAT} signal was measured from baseline sample. 55 mM trans-1,2-bis(4-pyridyl)-ethylene (BPE) solution in ethanol was contained in a microchannel (height: 100 μm) and N_{NEAT} was calculated to be (the detection volume) \times (molar concentration) \times (Avogadro's number). I_{SERS} was measured from samples and N_{SERS} was calculated to be $\frac{4\pi r^2}{\sigma} \times n$ where r is radius of an individual nanoparticle, σ is surface density of the number of molecules and n is the number of the particles in a single pattern. In this measurement, trans-1,2-bis(4-pyridyl)-ethylene (BPE) molecules were used for chemical detection and its σ is 9.95×10^{13} molecules / cm^2 . The number of particles, n , was either counted from SEM images of assemblies, or estimated by assuming hemisphere geometries and complete packing cases. The calculated N_{SERS} is the upper bound value since it is based on the assumption that BPE molecules are absorbed to entire surface area of every single gold particle. Therefore, calculated enhancement factor is also a conservative estimate. The results of enhancement factor calculation are summarized in Table B.1.

Table B.1 Enhancement factor calculation

Pattern Diameter	SERS measurement data		
	Intensity (count)/ Unit area	Normalized Intensity	Enhancement Factor
Base	2.95×10^{11}	1	1
1.7 μm	5.46×10^{11}	1.85	1.36×10^6
3.7 μm	1.73×10^{12}	5.86	1.39×10^5
10 μm	1.15×10^{14}	390	4.69×10^5
30 μm	3.45×10^{14}	1170	6.84×10^4

B.3. Estimating Number of Particles, n, in 30 μm Diameter Patterns

The laser spot was circular shape with 20 μm diameter. Therefore, whole region of 1.75 μm , 3.70 μm , 10.0 μm diameter patterns were included by the laser spot and all particles of the pattern were counted as n. However, in case of the 30 μm diameter dot, the laser spot size was smaller than the pattern size. Therefore, laser was applied to only the center part of the pattern. Spherical cap geometry was assumed to define the excluded region for SERS measurement in the pattern and calculation of n is followed.

Appendix C. Supporting Information for Chapter 5

C.1. Iterative Solution Schemes

The second-order system of interest is following. The equation of motion is given by

$$m_i \ddot{r}_i + c_i \dot{r}_i = m_i \dot{v}_i + c_i v_i = m_i \dot{v}_i + c_i \dot{r}_i = \psi_i^{nf} \quad (\text{D.1})$$

From Zohdi's work[166],

$$\dot{v}_i(t + \phi\Delta t) = \frac{v_i(t+\Delta t) - v_i(t)}{\Delta t} + \hat{O}(\Delta t) \quad (\text{D.2})$$

$$\dot{r}_i(t + \phi\Delta t) = \frac{r_i(t+\Delta t) - r_i(t)}{\Delta t} + \hat{O}(\Delta t) \quad (\text{D.3})$$

$$\psi_i^{nf}(t + \phi\Delta t) = \phi\psi_i^{nf}(t + \Delta t) + (1 - \phi)\psi_i^{nf}(t) \quad (\text{D.4})$$

Neglecting reminder terms and inserting (D.2), (D.3) equations to (D.1),

$$m_i \frac{v_i(t+\Delta t) - v_i(t)}{\Delta t} + c_i \frac{r_i(t+\Delta t) - r_i(t)}{\Delta t} = \psi_i^{nf} \quad (\text{D.5})$$

After rearranging the terms, the position of i^{th} particle is expressed as

$$r_i(t + \Delta t) = r_i(t) + \frac{\Delta t}{\left(1 + \frac{\Delta t}{m_i} c_i \phi\right)} \left(v_i(t) + \frac{\phi(\Delta t)}{m_i} (\phi\psi_i^{nf}(t + \Delta t) + (1 - \phi)\psi_i^{nf}(t)) \right) \quad (\text{D.6})$$

Effective drag coefficient is defined via

$$C_D \stackrel{\text{def}}{=} \frac{\|\psi_i^{drag}\|}{\frac{1}{2}\langle \rho_f \rangle_{wi} \|\langle v_f \rangle_{wi} - v_i\|^2 A_i}, \quad (\text{D.7})$$

where $\langle (\cdot) \rangle_{wi} \stackrel{\text{def}}{=} \frac{1}{|w_i|} \int_{w_i} (\cdot) dw_i$ is the volumetric average of the argument over the domain occupied by the i^{th} particle, $\langle v_f \rangle_{wi}$ the volumetric average of the fluid velocity, v_i is the velocity of the i th (solid) particle and where A_i is the cross-sectional area of the i^{th} (solid) particle. Drag number is represented as a function of the Reynolds number:

- For $0 < Re \leq 1$, $C_D = \frac{24}{Re}$,
- For $1 < Re \leq 400$, $C_D = \frac{24}{Re^{0.646}}$,
- For $400 < Re \leq 3 \times 10^5$, $C_D = 0.5$,
- For $3 \times 10^5 < Re \leq 2 \times 10^6$, $C_D = 0.000366 Re^{0.4275}$,
- For $2 \times 10^6 < Re \leq \infty$, $C_D = 0.18$,

where the local Reynolds number for a particle is $Re \stackrel{\text{def}}{=} \frac{2b_i \langle \rho_f \rangle_{wi} \|\langle v_f \rangle_{wi} - v_i\|}{\mu}$ and where b_i is the radius of the i^{th} particle.

$$\|\psi_i^{drag}\| = \left(\frac{1}{2} \langle \rho_f \rangle_{wi} \|\langle v_f \rangle_{wi} - v_i\|^2 A_i \right) C_D \quad (\text{D.8})$$

In this work, it was assumed that $\|\psi_i^{drag}\|$ is proportional to $\|\langle v_f \rangle_{wi} - v_i\|$ instead of $\|\langle v_f \rangle_{wi} - v_i\|^2$ because stoke's law usually holds for low Reynolds number where the local Reynolds number for a particle is $Re \stackrel{\text{def}}{=} \frac{2b_i \langle \rho_f \rangle_{wi} \|\langle v_f \rangle_{wi} - v_i\|}{\mu}$ and where b_i is the radius of the i^{th} particle.

Therefore,

$$\overline{\psi_i^{drag}} = \left(\frac{1}{2} \langle \rho_f \rangle_{wi} \|\langle v_f \rangle_{wi} - v_i\| A_i \right) C_D \bar{v}_i = c_i v_i \quad (D.9)$$

If it is assumed $\langle v_f \rangle_{wi} = 0$,

$$c_i = \left(\frac{1}{2} \langle \rho_f \rangle_{wi} \|v_i\| A_i \right) C_D. \quad (D.10)$$

This drag coefficient is incorporated to (D.6). The position of i^{th} particle is implicitly expressed as

$$r_i^{L+1} = r_i^L + \frac{1}{1 + \frac{\Delta t}{m_i} \left(\frac{1}{2} \rho v_i^L C_D A \right) \phi} \left(v_i^L \Delta t + \frac{\phi (\Delta t)^2}{m_i} \left((\phi \psi_i^{nf,L+1} + (1 - \phi) \psi_i^{nf,L}) \right) \right) \quad (D.11)$$

The equation (D.11) can be solved recursively by recasting the relation as

$$r_i^{L+1,K} = G(r_i^{L+1,K-1}) + R_i \quad (D.12)$$

Where $K=1,2,3,\dots$ is the index of iteration within time step $L+1$ and R_i is a remainder term that does not depend on the solution, i.e.

$$R_i \neq R_i(r_1^{L+1}, r_2^{L+1} \dots r_N^{L+1}) \quad (D.13)$$

$$\begin{aligned} r_i^{L+1,K} = & \underbrace{r_i^L + \frac{1}{1 + \frac{\Delta t}{m_i} \left(\frac{1}{2} \rho v_i^L C_D A \right) \phi} \left(v_i^L \Delta t + \frac{\phi (\Delta t)^2}{m_i} (1 - \phi) \psi_i^{nf,L} \right)}_R \\ & + \underbrace{\frac{1}{1 + \frac{\Delta t}{m_i} \left(\frac{1}{2} \rho v_i^L C_D A \right) \phi} \left(\frac{(\phi \Delta t)^2}{m_i} \psi_i^{nf,L+1} \right)}_{G(r^{L+1,K-1})} \end{aligned} \quad (D.14)$$

where

$$\psi_i^{nf,L} \stackrel{\text{def}}{=} \psi_i^{nf,L}(r_1^L, r_2^L \dots r_N^L) \quad (D.15)$$

and

$$\psi_i^{nf,L+1,K-1} \stackrel{\text{def}}{=} \psi_i^{nf,L+1,K-1} (r_1^{L+1,K-1}, r_2^{L+1,K-1} \dots r_N^{L+1,K-1}) \quad (\text{D.16})$$

The convergence of Equation (D.16) is scaled by

$$\eta \propto \frac{(\phi \Delta t)^2}{m_i + \Delta t \left(\frac{1}{2} \rho v_i^L C_{DA} \right) \phi} \quad (\text{D.17})$$

If convergence is slow within a time step, the time step size can be reduced properly to increase the rate of convergence. However, decreasing the time step size leads to the increase of overall computing time. There exists an optimal time step size in a response to the trade-off between high convergence rate for accurate estimation of the solution and short computing time. In order to estimate the optimal time step size, an approach found in Zohdi's work[166] is followed, in which (1) one approximates

$$\eta^{L+1,K} \approx S(\Delta t)^p \quad (\text{D.18})$$

(S is a constant) and (2) one assumes that the error within an iteration to behave according to

$$(S(\Delta t)^p)^K \bar{\omega}^{L+1,0} = \bar{\omega}^{L+1,K} \quad (\text{D.19})$$

$K=1,2,\dots$, where $\omega^{L+1,0}$ is the initial norm of the iterative error and S is intrinsic to the system. In order to meet an error tolerance in an exact preset number of iterations, a tolerance, TOL , is imposed as criteria.

$$(S(\Delta t_{tol})^p)^{K_d} \bar{\omega}^{L+1,0} = TOL \quad (\text{D.20})$$

Where TOL is a tolerance and where K_d is the number of desired iterations. If the error tolerance is not met in the desired number of iterations, the contraction constant, $\eta^{L+1,K}$ is too large. Δt_{tol} can be represented as

$$\Delta t_{tol} = \Delta t \left(\frac{\left(\frac{TOL}{\bar{\omega}^{L+1,0}} \right)^{\frac{1}{pK_d}}}{\left(\frac{\bar{\omega}^{L+1,K}}{\bar{\omega}^{L+1,0}} \right)^{\frac{1}{pK}}} \right) \quad (D.21)$$

In the analysis of our systems, p was chosen to be 1~2 and K_d was chosen to be 3.

C.2. Computational Algorithms

A developed iterative solution scheme was implemented by following computational algorithms.

(1) SET INITIAL ASSEMBLY TIME (T_i) AND ITERATION NUMBER (N)

(2) FOR $i = 1 : N$

(3) GLOBAL FIXED – POINT ITERATION: (SET $i = 1$ AND $K = 0$):

(4) FOR $i = 1$ TO N_p (=NUMBER OF PARTICLES)

(a) COMPUTE NEAR-FIELD FORCE, ψ_i^{nf}

(b) COMPUTE DRAG COEFFICIENT, c_i

(c) COMPUTE POSITION: $r_i^{L+1,K}$

(5) ERROR MEASURE:

$$(a) \bar{\omega}_K \stackrel{\text{def}}{=} \frac{\sum_{i=1}^{N_p} \|r_i^{L+1,K} - r_i^{L+1,K-1}\|}{\sum_{i=1}^{N_p} \|r_i^{L+1,K} - r_i^L\|}$$

$$(b) TOL_K \stackrel{\text{def}}{=} (S(\Delta t_{tol})^p)^{K_d} \bar{\omega}^{L+1,K}$$

$$(c) Z_K \stackrel{\text{def}}{=} \frac{\bar{\omega}_K}{TOL_K}$$

$$(d) \phi_K \stackrel{\text{def}}{=} \frac{\bar{\omega}_K}{TOL_K}$$

(6) IF TOLERANCE MET ($Z_K > 1$) AND $K \geq K_d$ THEN:

(a) CONSTRUCT NEW TIME STEP : $\Delta t = \phi_K \Delta t$

(b) RESTART AT TIME = t AND GO TO (4)

(7) IF TOLERANCE MET ($Z_K \leq 1$) AND $K < K_d$ THEN:

(a) INCREMENT TIME : $t = t + \Delta t$

(b) CONSTRUCT NEW TIME STEP : $\Delta t = \phi_K \Delta t$

(c) SELECT MINIMUM : $\Delta t = \text{MIN}(\Delta t^{lim}, \Delta t)$ AND GO TO (4)

(8) COMPUTE MEASURE

(a) $d_a \stackrel{\text{def}}{=} \frac{\sum_{i=1}^{N_p-1} \|r_{i+1} - r_i\|}{\sum_{i=1}^{N_p} i}$ (Average distance of inter-particle spacings)

(b) $T_s = \sum_{i=1}^N \Delta t$ (Total estimated assembly time)

(c) $t_r \stackrel{\text{def}}{=} \frac{\|T_s - T_i\|}{T_i}$ (Error between initial assembly time and estimated assembly time)

(9) IF $d_a > d$ (*Particle diameter*) THEN:

(a) IF $T_s < T_i$ THEN: $N = N + \Delta N$, GO TO (1)

(b) IF $T_s > T_i$ THEN: $T_i = T_i + \Delta T$, GO TO (1)

(10) IF $d_a \leq d$ (*Particle diameter*) THEN:

(a) IF $t_r > 0.01$ THEN: $T = \frac{T_s + T_i}{2}$, GO TO (1)

(b) IF $t_r < 0.01$ THEN: $T = T_i$, ITERATION ENDS

C.3. Determination of Total Assembly Time

Total assembly time of the particle clusters, T , was iteratively estimated by varying main two parameters, initial assembly time, T_i , and iteration number, N . Estimated assembly time, T_e , was calculated by $T_e = \sum_{i=1}^N \Delta t$ and compared with T_i . Guessing T_i and N were attempted until $t_r \stackrel{\text{def}}{=} \frac{\|T_s - T_i\|}{T_i}$ (Error between initial assembly time and estimated assembly time) becomes less than 0.01. After this condition was satisfied, T was assigned as T_i .

C.4. Determination of Distribution of Initial Particle Displacement

After the creation of droplets on the surface from a printing head, it was assumed that the particles in the droplets are randomly dispersed. N (number of particles in a droplet) sets of three variables in spherical coordinate systems, ρ, θ, φ were randomly generated and x, y, z computed are calculated from the sets.